DECIPHERING THE MOLECULAR INTERACTIONS BETWEEN ANTIMALARIALS AND HEMATIN CRYSTAL SURFACES

by

Wenchuan Ma

A dissertation submitted to the Department of Chemical and Biomolecular Engineering
University of Houston
in partial fulfillment of the requirements for the degree of

DOCTOR OF PHOLOSOPHY

in Chemical Engineering

Co-Chair of Committee: Peter G. Vekilov

Co-Chair of Committee: Jeffrey D. Rimer

Committee Member: Ognjen Miljanic

Committee Member: Vincent Donnelly

Committee Member: Alamgir Karim

Committee Member: Jeremy Palmer

Committee Member: Viktor G. Hadjiev

University of Houston
May 2021

ACKNOWLEDGEMENTS

I express my sincerest gratitude for Dr. Peter Vekilov and Dr. Jeffrey Rimer. I am very grateful for the Katy Olafson and Mohammad S. Safari. I joined your labs to work on the hematin project under your guidance. This lightened my pathway for four years of learning; without this opportunity, I would not have become the scientist that I am today. To Peter and Jeff, you have guided me through multiple challenging projects and crafted me into an expert in the field of crystal growth and design; you have shown me how to expand my line of thinking and to continuously approach unanswered questions. Peter, I owned you a special thanks for not only for all the scientific knowledge you shared but also you brought the spirit of confidence I never had before. I love the stories you spoke, both for scientific moments in the history or small tricks in the daily life. I will continue to be an expert on the fundamentals of crystal growth, hoping to make you proud. Jeff, you showed me how to be an artist in writing; A well wrote paper can be as good as documentary but also as casual as a novel. Thank you both for giving me the opportunity to craft my own experiments, including the complexation, constituent, and adhesion force studies. I am infinitely grateful for the creative license to grow as a researcher during my time here.

Thank you to my committee members Dr. Jeremy Palmer, Dr. Ognjen Miljanic, Dr.Vincent Donnelly, Dr. Alamgir Karim and my advisors for their time, expertise, and fruitful thoughts on my projects over the years. Your encouragement and thought-provoking conversations continually expanded the breadth of experiments and trail of thoughts which led to cohesive and well-rounded storylines.

I want to thank all the lab mates for their courtesy and kindness. Work become really enjoyable when you work in a friendly environment and the shared experience from different fields expanded the view. I really appreciate all insights of proteins syntheses, purification and characterization shared from my lab mates.

I need to send special gratitude to all my friends. It was enjoyable to celebrate all the achievements with you guys. It is appeased that you guys find the next stations in the future.

I would like thank several individuals who have been extremely helpful to my projects. I want to thank Corie Peterson for offering important insights to initialize the synthesis of artemisinin adducts. I would like to send my best gratitude to Dr. David Sullivan and Victoria Balta for producing all the malaria assays and insights that bought the understanding of mechanism how antimalarial drugs against the malaria parasite to a next level.

The journey of PhD was really enjoyable thanks to all of you.

Abstract:

Crystallization is the central process of materials synthesis in biological, geological, and extraterrestrial systems. Nature achieves remarkable diversity of shapes, patterns, compositions, and functions of the arising crystalline structures by combining simple strategies to control the number of nucleated crystal and the sizes to which they grow. In recent years, organic and mixed inorganic-aqueous liquids have received greater attention as alternative solvents for preparation of crystalline materials and separation (or purification) by crystallization, in particular for high-value materials such as pharmaceuticals and fine chemicals. In contrast to crystallization from purely aqueous solvents, the level of understanding of the fundamental processes of crystal growth from such liquids is severely limited. Issues that have been addressed are solvent selection, control of nucleation and growth (including seeding), solubility, transport regimes, and effects of ongoing solute synthesis, among others. In most cases, the optimization of the growth processes is carried out by trial-and-error or by mimicking pathways developed for other compounds. The lack of insight into the relevant fundamental mechanisms has emerged as a major obstacle to a rational approach to optimization and control of crystallization in organic and mixed solvents.

Approximately 3.2 billion people are at risk of malaria. Hematin is released as a byproduct of hemoglobin catabolism during the malaria parasite lifecycle in human erythrocytes and detoxified by sequestration as innocuous hemozoin crystals. Hematin crystallization has been the most effective target for antimalarial drugs. Previous studies have found that the formation of hematin crystals follows a classical mechanism whereby

new crystal layers are nucleated on top of existing ones and spread to cover the entire face. Direct observations established two classes of quinoline inhibition mechanisms. Amodiaquine and mefloquine were found to largely only bind to kink growth sites, where molecular units add to a step. This is the least effective mechanism of heme crystal growth inhibition. In a second mechanism, known as “step-pinning,” chloroquine and quinine bind on a flat surface face, inhibited new layer growth over broad areas of the crystal surface. We employed atomic force microscopy to monitor in real time the growth of steps on the (100) surface under the influence of varied drug combinations. This molecular-level view revealed that the action of quinine and amodiaquine is additive, indicating the lack on interaction between the action of each of these two drugs. Chloroquine and mefloquine weaken each other’s action, indicting antagonism in their suppression of hematin growth. These findings may serve as a basis for a lock-and-key approach to targeted drug development that is rooted in the physical basis for hemozoin crystal growth inhibition

One of the most relevant, yet the least investigated pathological crystal is cholesterol crystal, which is a principle component of gallstones(*1-5*) and atherosclerosis (*6, 7*). Prior studies have largely focused on the effects of phospholipids and bile salts on the formation of cholesterol crystals;(*8*) however, few groups have examined the mechanism(s) of crystallization. To this end, we conducted preliminary studies revealing cholesterol crystal growth occurs by a combination of classical and nonclassical(*9*) pathways involving the addition of monomer and precursors (i.e. clusters), respectively.

Table of Contents

List of Tables

List of Figures

Chapter 1: Introduction to crystal growth

Crystallization is a natural process which occurs as materials solidify from a liquid as they participate out of a liquid or gas. Crystallization is a process directed by properties of molecules and the environment in which a crystal develops. A complex combination of factors controls the way of the formation, the rate of growth and eventually lead to a various distribution of size, morphology, surface roughness and so on. The understanding of fundamental mechanisms of crystal growth could potentially accelerate the designed crystal transformation or stopped those undesired. The functionality of additives participated in the crystallization process could guide the discovery of new pharmaceuticals drugs.

1.1 Mechanisms of crystal growth

In the process of forming a solid phase from a supersaturated solution, the timescale of the transition divided the progress into nucleation and growth. The development of microscopic techniques revealed the different pathways in which the intermedium displays distinctive habit with defined physicochemical properties. Different intermedium observed in the nucleation process lead to a proposal of nonclassical theory. The characterizations and identification of those intermedium provide key information on that external parameters. Controlling nucleation is an essential aspect to modify the crystal polymorphism, size, morphology and other characteristics. Molecules in the solution assembly into the ordered structure. The process is largely impacted by factors

like solvent, temperature pressure, concentration and so on. Understanding and controlling nucleation is important for many crystallization applications.

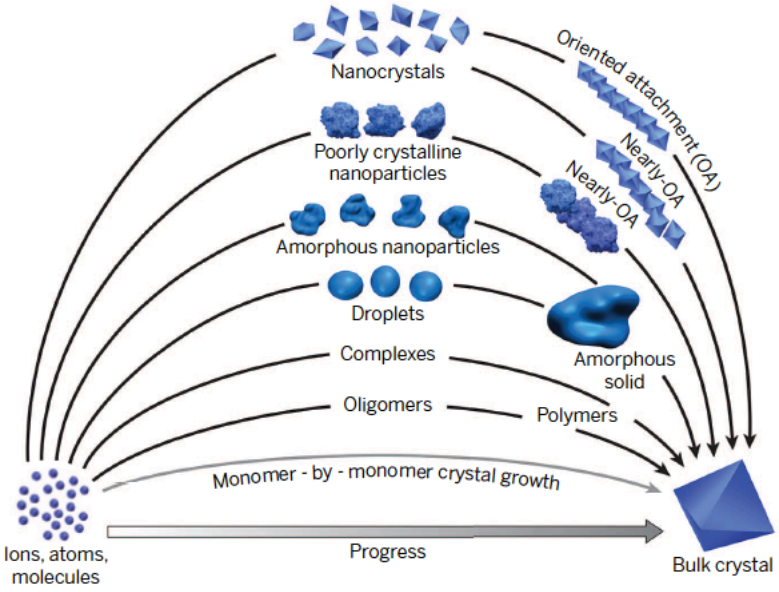

Figure 1. Various intermedium working as precursory particles for crystallization.

1.1.1 Classical Crystallization

Basic classical nucleation describes the formation of nuclei by monomer by monomer addition from the solution to the crystal surface and the formation of a bulky new face and of an interface. A Kossel crystal is a general shape of a basic cubic crystal in which particles are considered as Blocks that impact of simple shear on the crystallization and takes account only the interaction between the atoms. The energy for the system is a summation of the number of bonds and change of freedom of atoms and the crystallization is driven by the energy change when a particle gets in cooperated into the crystal structure. 6 bonds will form when a particle is structured in the bulk structure and 5 possible sites for a particle attached on the surface: (1) vacancy in a terrace/face, (2)

hole in a step, (3) kink, (4) step edge and (5) directly to terrace or face. Ideally, the change in the number of dangling bonds from attaching a molecule determines of the driving forcing. As a consequence, crystals can fix the defects point by filling the vacancy, generating a new lane by attaching to the kinks site, generating new lanes by attaching on the step edge and forming new layers by the new terrace.

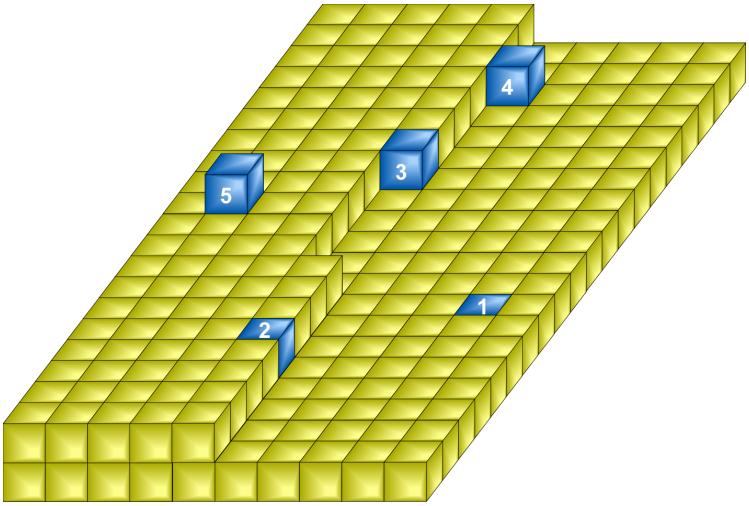

Figure 2. Possible sites for particle attachment in classical crystallization.

In the driving force. Besides, the energy difference between atoms dropped on the terrace and those stay in the kink sites lead to a shift called surface diffusion. Surface diffusion is a general process that involves the motion of adsorbed atoms on the surface of a solid material. Surface diffusion may appear a complex energy barrier as the complexity surface structure combined from both solvent and solute sides. The barriers have both enthalpic and entropic contributions raised from the remove of solvent, bond formation/disassociation and structure thrift during the movement of particles on the surface. However, those barriers are generally smaller than the energy barrier of direct

incorporation. As the growth rate is determined by the slowest process, surface diffusion plays a pivotal role in determine the growth pathway of a seed.

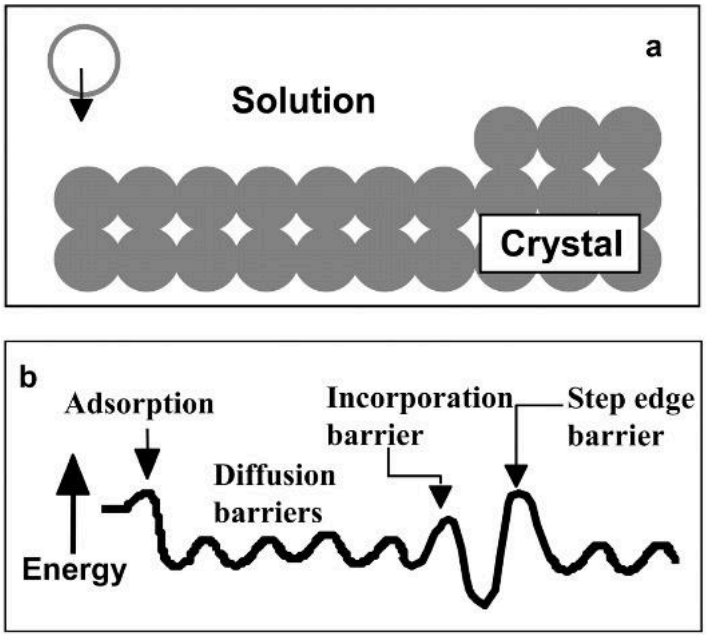

Figure 3. Energy barriers involved in the process of surface diffusion.

1.1.2 2D nucleation and critical radius

When a molecule attaches to a surface, it can either dissociate from the surface and back to the solute phase or stay as part of the bulk crystal for another molecule to attach. The growth of particles on the terrace both increase the volume and surface area. As a consequence, a new layer will be generated on the top of the terrace and this process is called 2D nucleation.

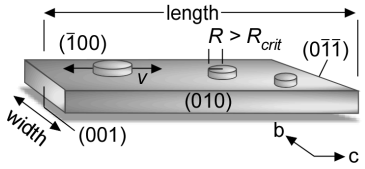

Figure 4. Diagram of two-dimensional nucleation and layer propagation on a crystal surface.

The energy of the system drops due to the increasing number of bond formation and increasing due to the raise of the line tension that describes with the Gibbs free energy,

$$\Delta \boldsymbol{G} = -\boldsymbol{\pi r^2 h \Delta g_v} + \boldsymbol{2\pi r h \gamma}, \quad (1)$$

where $\Delta \boldsymbol{g_v}$ is the Gibbs free energy per volume and $\boldsymbol{\gamma}$ is the surface tension we need to break a nucleus. The critical radius $\boldsymbol{r_c}$ is given by the maximum of the Gibbs free energy and at this point the nuclei has 50 percent chance for growth or dissolution. When the nuclei size exceeds $\boldsymbol{r_c}$, the layer will spread until it reaches the crystal edges, thus resulting in a faceted crystal.

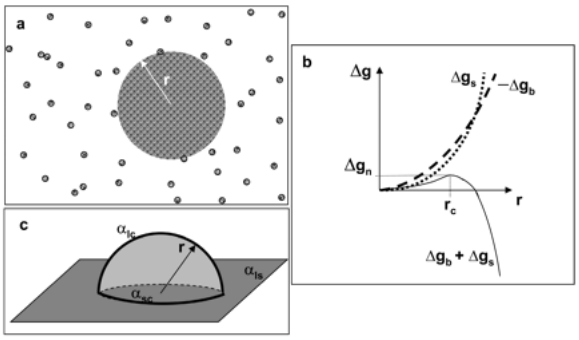

Figure 5. Energy barrier for molecule incorporation (a) 3D homogeneous nucleation, (b) The Gibbs free energy per volume and Gibbs free energy per surface area, (c) 2D nucleation on a substrate.

1.1.3 Crystal defects and dislocation

Crystal defects are imperfection in the regular arrangement of the atoms in a crystalline solid. Defects can be located at single points, along lines, or on whole surfaces in the solid. Point defects include the Frenkel type, the Schottky type, and the impurity

type. Point defects are caused by particle drift, particle removal or particle replacement. Surface defects may arise at the boundary between two grains, or small crystals, within a larger crystal leading to a mismatch across the grain boundary. Line defects are lines along whole rows of atoms in ta solid are arranged anomalously. The irregularity in spacing lead to the line of dislocation.

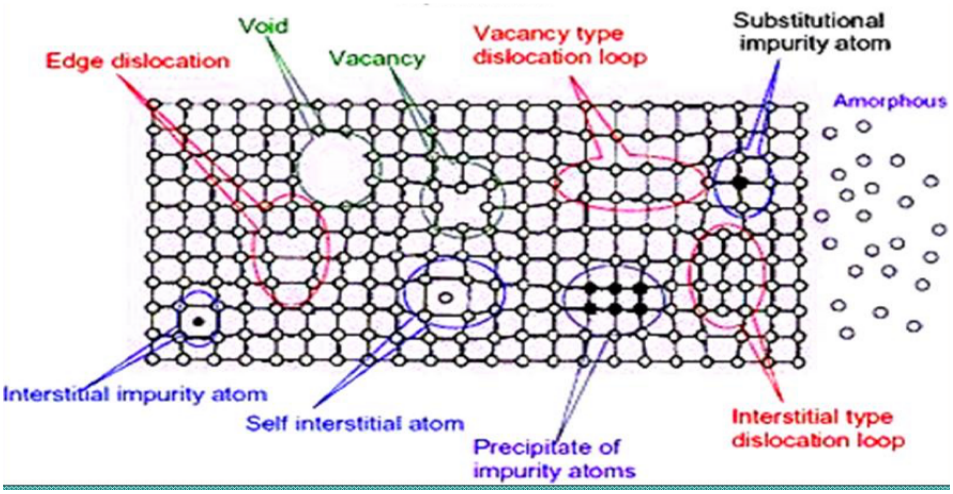

Figure 6. Illustration of various crystal defects.

Dislocation is a prominent pathway of crystallization at low supersaturation as the energy barrier is much smaller than the energy required for generation of new layers. As a linear crystallographic defect generated on the surface, the movement of dislocations allow atoms to slide over each other at low stress. The surface is continuously warped as the growth front advances, clockwise or counterclockwise. In the same time, Burgers vectors might emerge on a crystal surface. Plastic deformation is directly related to the motion of mobile dislocations. Dislocation lines cannot end within a crystal and crystals follow dislocation growth preserve sequences of layer succession in crystals. Layers

advance across the surface usually display a step height related to the size of a unit cell. The growth of a crystal followed by dislocation can be described with equation

$$\boldsymbol{R = \frac{h}{\lambda} v = \frac{h\Delta\mu v}{19\Omega\alpha}.} \quad (2)$$

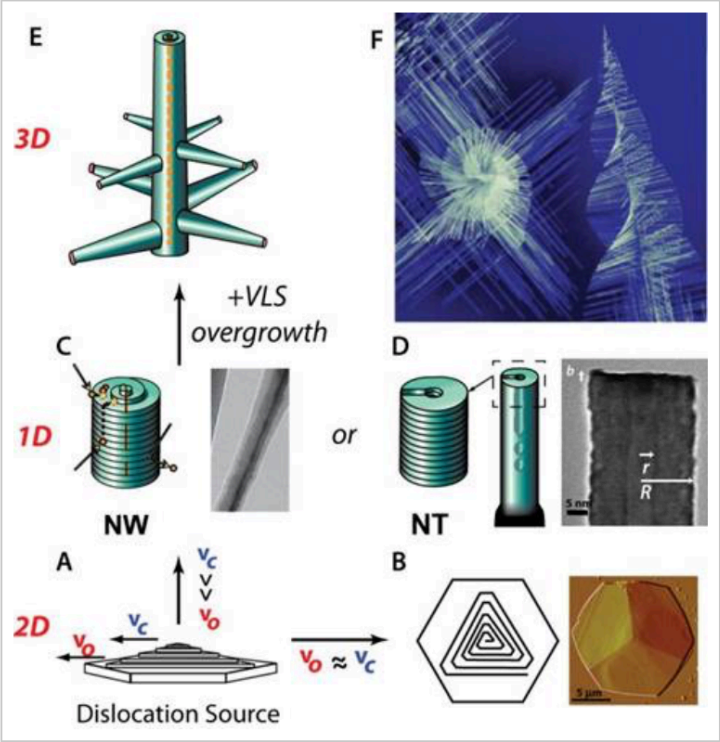

Figure 7. Formation pathways for different nanostructures driven by screw dislocations.

1.1.4 Nonclassical mechanisms of crystal growth

The idea of precursor was proposed to explain the formation of many crystallization processes in which crystals displayed physical single crystal properties though it does not follow a molecule-molecule attachment pathway. Modern experimental techniques have shown that the nucleation process can proceeds through a various pseudo equilibrium state before reaching the final thermodynamically stable phase. Crystals are not formed directly from assembling of monomer. Instead, monomer

will form precursors vary with respect to their microstructure, size and shape that largely depends on the circumstance. The existing of precursors also opens possibility for controlling the nucleation pathway.

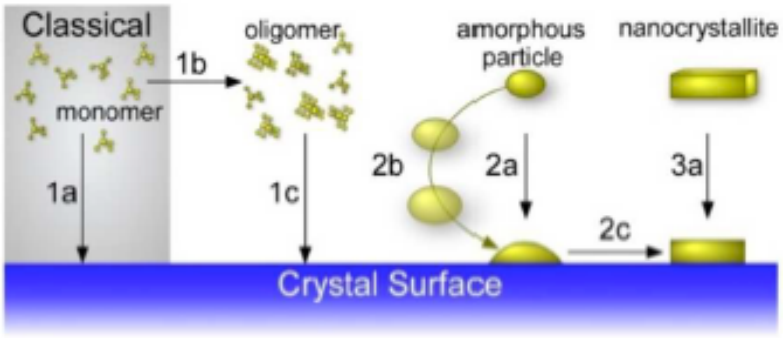

Figure 8. Pathways for monomer to transfer into crystalline and the impact on the original surface.

A recent study of olanzapine provided direct state that dimer can work as the basic element for crystallization(*10*). The work demonstrate that the symmetry elements of olanzapine crystals emerge in solute dimers in solution prior to crystallization. The crystal growth was monitored with time-resolved in-situ scanning probe microscope and the result exhibits a quadratic dependence on the solution concentration. The result suggested dimer is preferred to adsorb on the surface and then diffuse to the growth sites though the monomer is the dominate species in the solution phase.

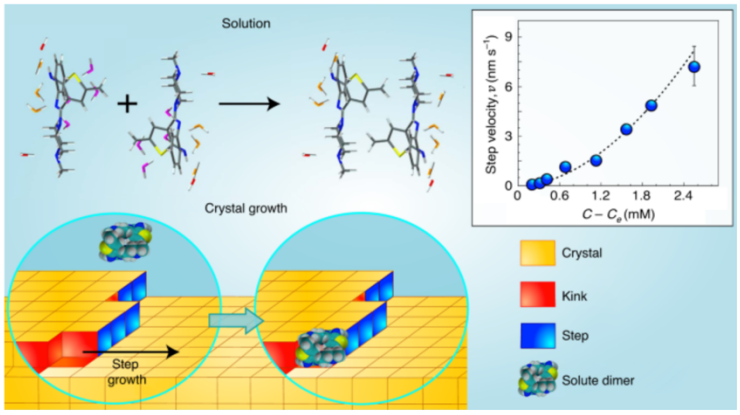

Figure 9. The transformation of olanzapine molecules and the quadratic growth rate.

The discovery of the amorphous calcium carbonate (ACC) in the crystallization pathways was recognized as a common strategy employed by many organisms to build biominerals (*11, 12*). ACC is composed of calcium carbonate that lacks long-range, periodic atomic scale order. ACC was observed as sphere particles with a radius of around 50 ~ 100 nm under the cryogenic TEM (*13*). Amorphous spheres were suspended in the supersaturated solution and transform into certain morphologies in microseconds when the supersaturation pass the limitation. The stability of ACC is largely impacted by the pH and ions in the solution. The evolution was monitored with WAXS to determine the species and time period. When the solution started from a neutral pH, the ACC transform directly to the final stage calcite. Conversely when mixing started from high pH around 15.5, vaterite formation was triggered with a much slower rate of formation(*14*). The result suggested that the structure depends on the binding strength of Ca^{2+} and CO_3^{2-} ions. The binding strength is inversely related to pH that plays a key role in controlling the stability of ACC. When other ions like mg^{2+} present in the solution, they may also participate in the process of ACC formation. XRD patterns suggested Mg can incorporated

into the crystal instead of attaching on the surface of ACC (*15*). Increasing the Mg/Ca ratio will largely increase the concentration of Mg in side ACC and delay the formation of final crystals that show a similar composition and morphology. The Roman spectrometry and simulation work predicted that the stability of ACC is controlled by the water structured around the ACC surface and the Mg has a better affinity to water and then the water can form a more affirmative structure in the presence of Mg.

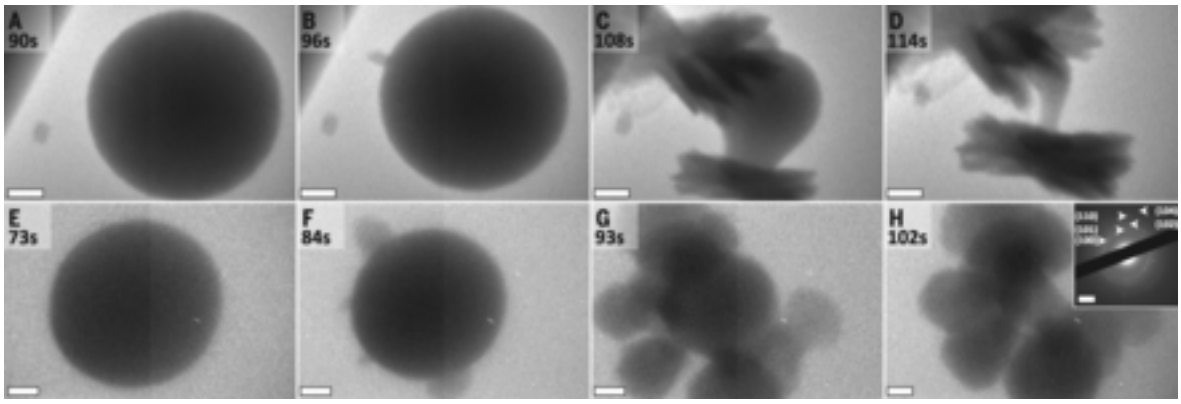

Figure 10. Frames show a previously nucleated ACC particle (*13*).

After the formation of different precursors, those intermedia can also work as growing units, transform into crystalline on the surface or provide new spots for layer generation. One of the important mechanisms of crystal growth is the oriented attachment of molecular clusters and nanoparticles in solution. In the James De Yoreo's work, they applied a high-resolution transmission electron microscopy using a fluid cell to directly observe oriented attachment of iron oxyhydroxide nanoparticles. As a cluster approaching the bulk crystal surface, particle undergo contiguous rotation and interaction to find a perfect lattice. The particle will jump to the contact point in a range of 1 nanometer, followed by lateral atom-by-atom addition (*16*). The ferrihydrite crystals grow both through monomer addition from solution and particle attachment events. The

balance between the long-range interactions. Osmotic forces may remain the stability of the nanoparticles and the Van Der Waal Force provide the attritive force as the nanoparticle begin to approach the bulk crystal.

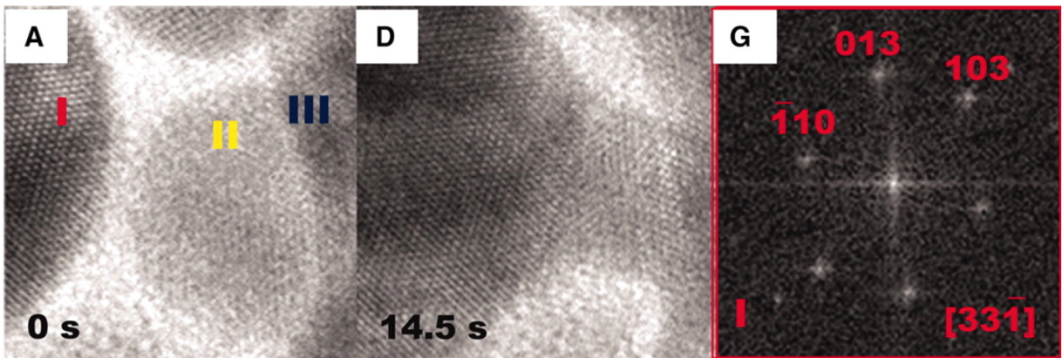

Figure 11. The atom-by-atom addition happened at the contact point.

Cluster and nanoparticles continuously form and appears coexist with crystals from early time. The deposition of nanoparticles on the crystal surface was observed in many crystal systems. The consequence introduced by nanoparticles greatly increase the complexity that underlines a growing crystal. From the atomic scope microscopy, those deposits can either inhibit or enhance the growth of the original crystal by changing the surface features. The excessive amount of small crystals deposited on the surface and embedded into the structure is commonly caused by the strain or macro steps that transformed the pathway of crystal growth to a different pattern. Moreover, cluster dropped on the surface may evolved into 3D layers as the deposit become the center of new source of hillocks. The dislocation center was introduced by a nonclassical pathway while the growth of hillocks still follow the classical theory (*17*).

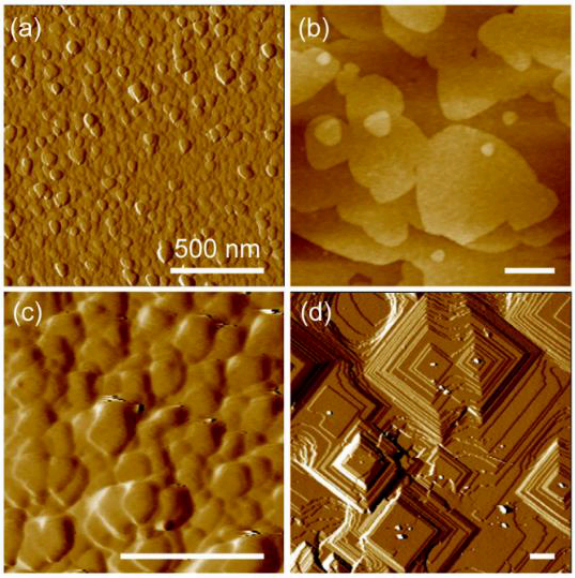

Figure 12. AFM images showing nonclassical (left column; A and C) and classical (right column; B and D) growth. (A) and (B) Silicalite-120 and (C) and (D) SSZ-13.52 Scale bars equal 500 nm.

1.2 Modifiers of crystallization

The use of growth modifiers can control growth and achieve desired physicochemical properties. Modifiers can range from ions to macromolecules, such as polymers or proteins. Modifiers mediate the accession of solute to growing crystals, often through specific binding to crystallographic faces, which inhibit solute to incorporation into active growth sites (18). Modifiers can also induce nonclassical pathways involving a vast number of growth units (19).

1.2.1 Growth modifiers varying the crystal growth

Crystallization is the central process of materials synthesis in biological, geological, and extraterrestrial systems (*20, 21*). Nature achieves remarkable diversity of shapes, patterns, compositions, and functions of the arising crystalline structures by combining simple strategies to control the number of nucleated crystals and their anisotropic rates

of growth (*22, 23*). To promote or inhibit crystallization in both natural and engineered environments, soluble foreign compounds are deployed that interact with the solute or the crystal-solution interface (*24*).

Modifiers act to inhibit crystal growth by either thermodynamic or kinetic routes. Crystal can grow through the incorporation of solute from either bulk solution or surface. Some modifiers may complex with solute in the solution and adjust the incorporating ability of solute molecules. Complexation may reduce the driving force for crystallization as it reduces the concentration of solute. On the other hand, the process may either increase or decrease the energy barrier of crystallization by changing the energy of rotation, affinity to the surface, diffusion ability and so on (*25, 26*). Part of modifiers showed interaction with kink sites and crystal surface. Modifiers bind to active sites on a crystal surface and thus reduce the density of kinks available to solute in solution. The later alters the free energy involved in the step advancement by changing the surface free energy.

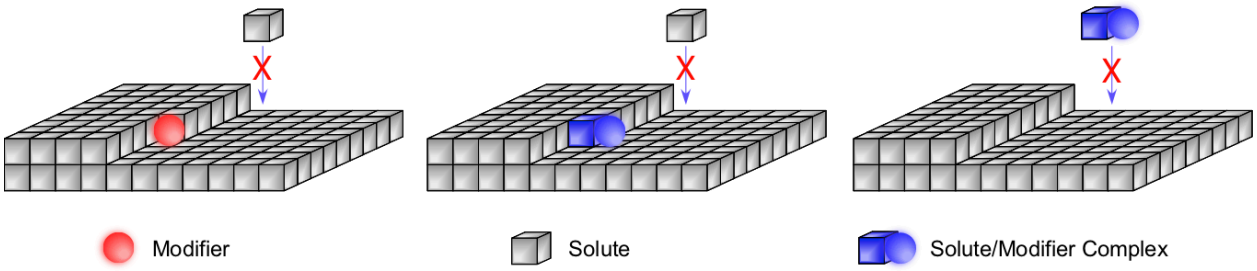

Figure 13. Mechanisms for inhibiting crystal growth.

1.2.2 Classical action modes of modifier

Crystal growth modifiers can take a variety of forms and have a wide range of effects on the kinetics of crystallization that include promotion and inhibition. Common positions of modifier inhibition attachment are kinks, steps or terraces.

In the mode of step pining, modifiers adsorb onto crystal terraces and the spacing of modifier will reduce as the concentration increase (*27*). As an advancing layer encounters the 'gate' formed by two of the adjacent modifiers, the step velocity v is reduced due to the increasing curvature of the surface layer. If two or more modifiers are spaced closed enough on the terrace, the step advancing can be fully arrested due to the fact that the energy to create surface area overwhelms the energy for to create space.

Modifiers can also bind to kink sites through a mode of cation called kink blocking. The adsorption of modifiers into kinks site will reduce the number density of kinks available to solute molecules both from solution and surface and reduce the rate of molecule attachment. The percent of layer advancement frustration is directly proportional to the percentage of occupied kink sites (*28*).

Recent studies in our group have shown that adsorbed modifiers can induce localized strain within a range of concentration that can dissolve the crystal surface (*29*). The crystal only dissolves in the certain range of modifier concentration. Below or above the concertation border, the growth can recover from the state of dissolution and begin to grow. The mechanism behind the phenomenon is still unclear.

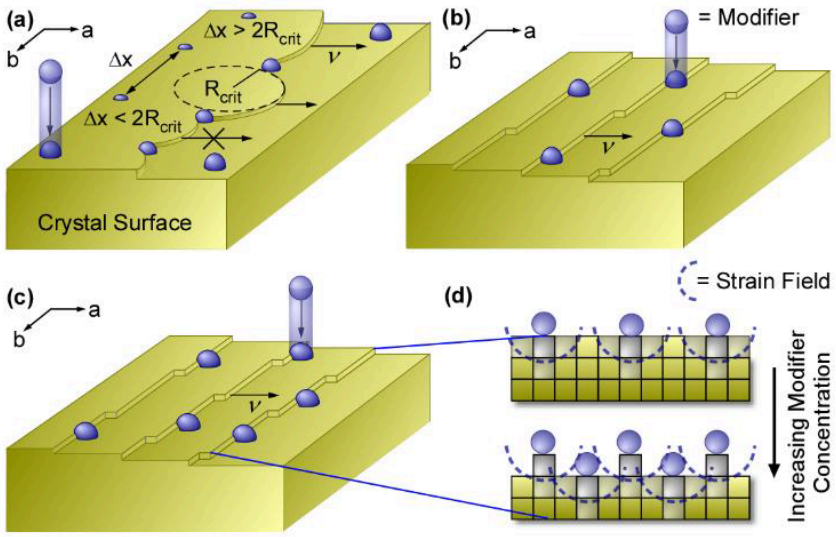

Figure 14. Illustration of types of modifiers. Modifiers absorb to (a) terraces and frustrate the step advancement, (b) kink sites and reduce the kink density, (c) and (d) surface and induce the strain under certain concentration (*24)*.

Chapter 2: Pathophysiological crystallization

Crystallization is essential for everyday operation for living beings, compared with a positive or negative consequence depends on the angle of view (*30-33*). In important class of diseases, aberrant crystallization directly or indirectly leads to several stats, although few contributions have been made to such disease from a materials science perspective. A fundamental understanding of mechanisms behind crystallization is essential for directing the pathogenesis of these diseases (*34*). A prominent example is the formation of crystalline hemozoin, a vital component of parasite physiology (*35, 36*).

2.1 Pathophysiology of malaria

Malaria is a severe disease caused by five species of parasites of the Plasmodium *(falciparum, vivax, malariae, knowlesi, and ovale)* (*37*). The *falciparum Plasmodium* strain is the most common one that leads to the significant consequences. Malaria is worldwide disease and the most people impacted by the disease in Africa and south Asia. Around 3.2 billion population is at risk of the infection and children are vulnerable group for this disease. Over recent year, there are renewed calls for elimination and eventual eradication of malaria. However, the fact the disease is carried by mosquitos limited the efficiency of stopping the transportation process. Also, the tricky system adopted by malaria parasite made the development of the vaccines a real challenge (*38*).

Malaria infection starts with a mosquito bite introducing *Plasmodium* sporozoites, which transfer to the erythrocytes, where they catabolize hemoglobin and release Fe(II) heme (*39*). The released heme rapidly oxidizes to Fe(III) hematin, which is toxic to the

parasite in its free state (*40*). The main mechanism of hematin detoxification implemented by the parasite is sequestration as inert crystalline hemozoin (*41*). Identification of hemozoin became integral to malaria diagnosis in 1880 (*42*) and its detection in the *Anopheles* stomach implicated several mosquito species as the vector (*43*). The first effective treatment for malaria, quinine extracts from the bark of the cinchona tree, was reported in 1632 (*44*). Since then, quinine, and its homologues chloroquine, mefloquine, and others, forming the quinoline class of antimalarials, have been used as both prophylactic and therapeutic drugs in nearly every type of malarial treatment (*45, 46*). It was found that quinolines bind hemozoin crystals and inhibit their growth (*47*). To date, heme sequestration has been the most successful molecular target for antimalarial drugs (*48*).

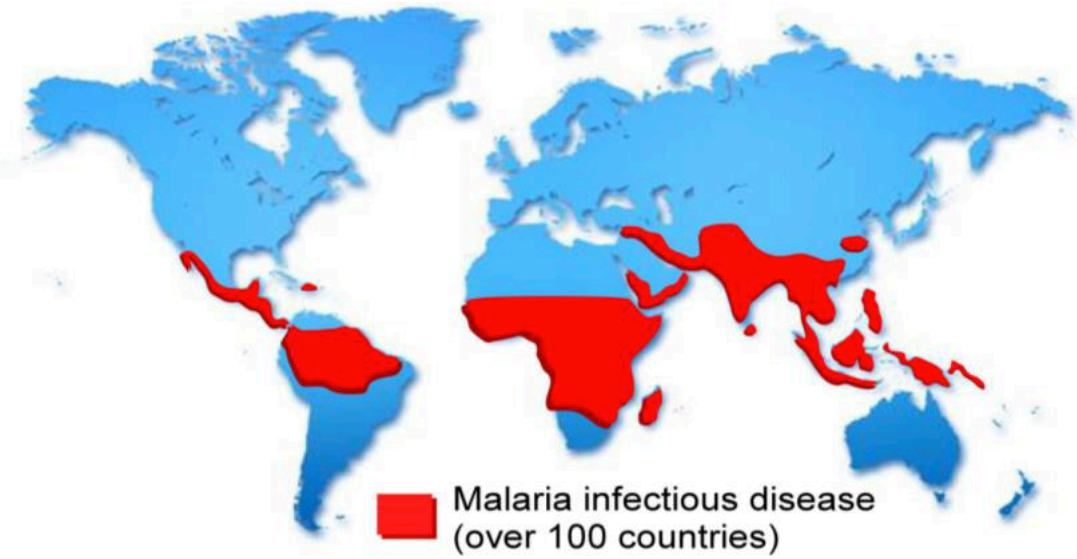

Figure 15. A world map for malaria infected area form W.H.O (*37*).

Plasmodium has a complex cycle alternating between female Anopheles mosquitoes and vertebrate hosts. The mosquitos transport malaria parasites' sporozoites and infect hosts from bits. Once sporozoites enter the host, they rely on gliding motility to reach and penetrate the wall of the blood vessel (*49*) and follow the stream of blood to host kidneys. The parasite grows mature and then begins to release merozoite back to blood stream. As merozoite beings to infect normal red blood cells, it indicts the parasite enters the blood stage in its life cycle. In the infected red blood cells, they multiply again until the cells burst for more infections. The cycle is repeated and leads to fever in the process of evasion. Meantime, some of the infected blood cells leave the cycle of asexual multiplication and those merozoites in the cells develop into sexual forms of the parasite, called gametocytes. Gametocytes will circulate in the human vessel until the patient gets bit by a mosquito. The mosquito gusts the gametocytes and later evolve into mature sex cells and begin a new round of malaria life-cycle.

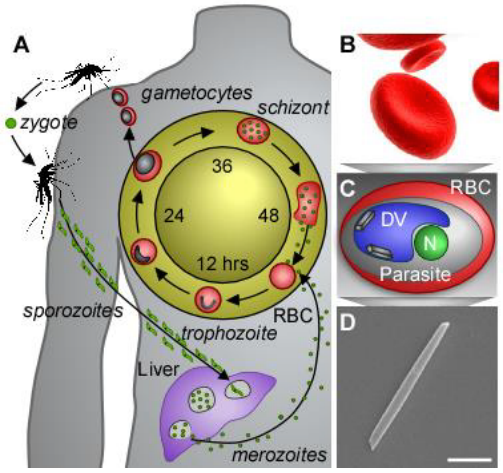

Figure 16. Schematic of the malaria Plasmodium lifecycle.

During the malaria parasite life cycle in human erythrocyte, parasites digest the protein hemoglobin, functional for transporting oxygen for human organs, to obtain the energy and source for multiplication. Heme is released during hemoglobin catabolism as byproduct that shows toxicity to parasite membrane (*50*). In the parasite digestion vacuole, heme is oxidized into hematin and parasite detoxifies by transforming hematin into crystals (*45*). The crystal formed in *vivo* called hemozoin and they commonly appear in the infected red blood cells. Hemozoin is identical to synthetic β - hematin crystals as they display the same powder X-ray pattern (*51*).

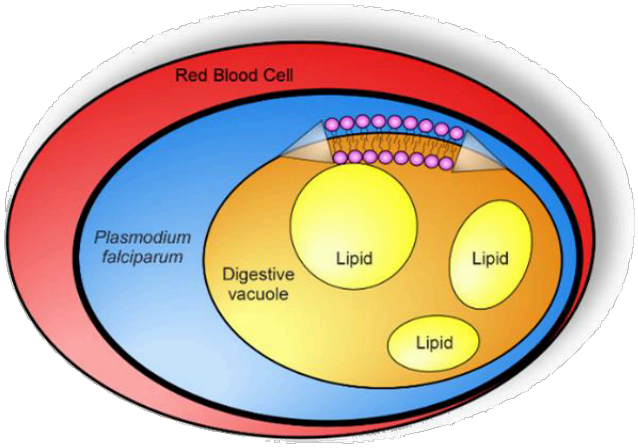

Figure 17. Schematic illustration of *Plasmodium falciparum* structure in an infected red blood cell.

The digestive vacuole is complex system with a predominantly acidic pH 4.8 – 5.5 aqueous phase (*52*). The digestive vacuole lipid membrane may promote the hematin nucleation as hemozoin crystals is observed under the electron microscopy to be enveloped in lipid bodies (*53*). Also, Pisciotta and coworkers succeeded in isolating hemozoin crystals within lipid nanospheres from parasite digestive vacuole from malaria parasites (*54*). To understand the direction of crystal growth within an aqueous or liquid

environment, projects done in our group by Katy Olafson and Megan Ketchum were aimed to answer those question by mimicking the parasite environment (*55, 56*).

X – ray diffraction (XRD) has shown that the crystals has a spacing structure of triclinic, with space group P1 (*57*). Hematin molecules are arranges as head-to-tail dimer bound by a coordination bond between oxygen atom of the central iron atom within the porphyrin ring of one hematin with a carboxylate oxygen of a second hematin (*57*). Unit parameter were solved as a = 1.2196 nm, b = 1,4684 nm and c = 0.8040 nm.

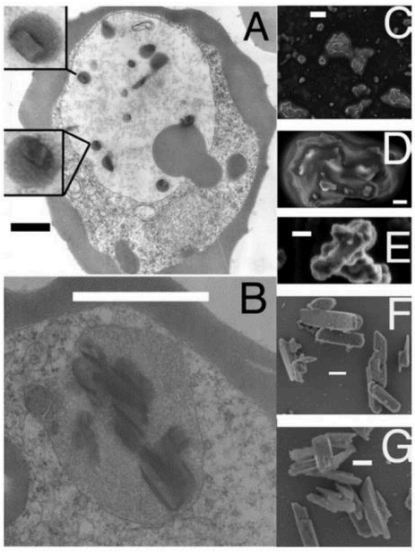

Figure 18. Scan electron microscopy images of hemozoin crystals from in the nanospheres droplets of lipid inside parasite digestive vacuole.

2.2 Antimalarials for malaria parasite

Antimalarial drugs have been widely used against malaria parasite. Many of the common antimalarial drugs are believed to suppress the parasite by inhibit hematin crystallization and hence increasing the concentration of hematin in the solution (*58*). Classical compounds include quinoline class compounds and artemisinin class was

discovered in recent years. One common method used for screening new drugs is taking assays for parasite cultures combined with various concentrations of drugs. For malaria, malaria parasites are cultured in the presence of antimalaria drugs and the efficiency is determined by concentration lead to a 50% of the parasite survival rate that is evaluated as IC_{50}. This approach requires to test a vast amount of synthesized organic compound samples restrained by the chemical and biopharmaceutical properties. As the increasing development of drug resistance for antimalarial drugs, the demand of discovering new antimalarial drugs is rising that motivates the exploration of fundamental understandings of malaria pathophysiology.

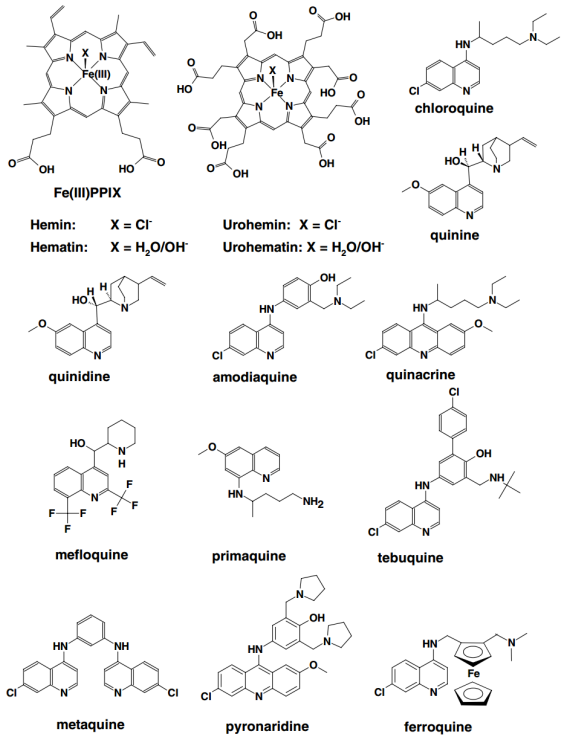

Figure 19. Structure of hematin molecule and antimalarial drugs (*59*).

2.3 Hematin crystallization from aqueous and organic solutions

To explore the mechanisms behind hematin crystallization and the interaction routes between antimalarial drugs and hematin crystal, a controllable system was development in our group (*55*) that mimics the environment in malaria parasite digestive vacuole while simplifies the lipid to an organic solvent with simpler structure. Hematin crystals were attempted to be grown larger than the physiological in order to acquire better information of crystal growth and surface development, including attempts for understanding the impact from the antimalarial drugs on crystallization.

2.3.1 Hematin growth environment.

Several key factors existed in the environment for the formation of hemozoin are the lipid membrane, pH ~ 4.8 aqueous phase and nanoparticles form in the lipid phase. In the Megan and Katy Olafson's work (*60*), critic buffer-saturated octanol was applied for simulating the lipid layer and the pH was controlled through a buffer made of a mixture of citric acid and NaOH solution. Citric buffer at pH 4.80 was prepared by dissolving 50 mM of citric acid in DI water and titrating the solution, under continuous stirring, with 0.10 M NaOH to the desired pH. The buffer pH was verified before each experiment and fresh buffers were prepared every month. We placed 5 mL of citric buffer at pH 4.80 in direct contact with n-octanol at 23°C and allowed 30 min for equilibration. The upper portion of the two-phase system was decanted and denoted as citric buffer-saturated octanol (CBSO).

2.3.2 Determine the extinction coefficient of hematin in CBSO

To understand and control the hematin crystallization in the CBSO system. The ultraviolet – visible (UV-Vis) spectrophotometry was put into use to determine the concentration of different compounds that follow the Beer – Lambert Law

$$\mathbf{A} = \boldsymbol{\varepsilon}\mathbf{b}\boldsymbol{C}, \tag{3}$$

where A is the absorbance, $\boldsymbol{\varepsilon}$ is the extinction coefficient, b is the path length of the cuvette, and C is the concentration of the solute.

Hematin powder always remains insoluble residue when hematin dissolves either in anhydrous or critic acid buffer saturated octanol. The hematin concentration in both solvents cannot be determined directly form the calculation of measured mass of dissolved material. As the accurate concentration of hematin solution is required for determination of the extinction coefficient, hematin was first dissolved in NaOH at a known concentration and then transferred to octanol phase by setting the hematin solution inContact with octanol solution for two weeks (*55*). The amount of hematin transferred into the octanol phase was determined from the difference of concentrations in NaOH before and after the inculcation.

The extinction coefficient of hematin dissolved in the 0.1 M NaOH was determined previously by measuring the absorbance spectra of the solutions with difference concentrations in the 200 – 800 nm wavelengths. The concentration of hematin in NaOH can be calculated through the mass of dilute as hematin powder can be full dissolved. The absorbance spectrum at 607 nm displayed a linear dependence between the intensity of

absorption and the concentration of hematin and the its slope yields the extinction coefficient of hematin in 0.1 M NaOH at this wavelength $\boldsymbol{\varepsilon_{hematin}}$ =3.86 ±0.06 $cm^{-1}mM^{-1}$.

Finally, the extinction coefficient of hematin in water-saturated octanol was determine through a series of incubated solutions with different concentration. The absorption band showed a local maximum at the wavelength of 594 nm. The slope of the linear correlation revealed the extinction coefficient of hematin in water-saturated octanol, $\boldsymbol{\varepsilon_{hematin}}$ =3.1 ± 0.1 $cm^{-1}mM^{-1}$.

The determination of the coefficient enables the measurement of hematin concentrations in the octanol solution that is the prerequisite for projects in which hematin crystals were generated in the CBSO system and the study of the growth of crystal under atomic force microscope.

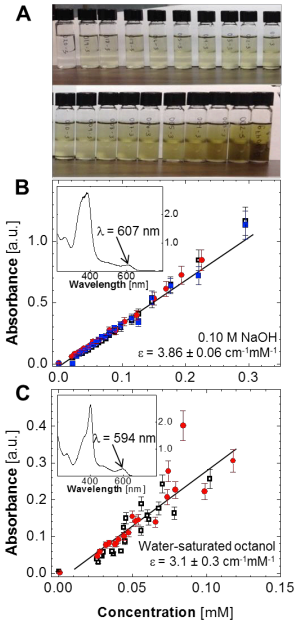

Figure 20. Determine the amount of hematin transferred to octanol phase (*55*).

2.3.3 Determine the solubility of hematin in CBSO

For crystallization to occur, the concentration of the solution must be larger than the solubility. Solubility fundamentally depends on the physical and chemical properties of the solution and solvent. Also, solubility is largely impacted by temperature, pressure and presence of other chemicals. Solubility reveals the equilibrium state between solution in the solution and crystal formed in the bulk showed below

$$\boldsymbol{hematin}\ (\boldsymbol{solution}) \rightleftharpoons \boldsymbol{hematin}\ (\boldsymbol{crystal}). \quad (4)$$

The activity of the soluble hematin was assumed to be equal to its concentration and the assumption was justified at low solubility values. Within the state, the intermolecular interactions are weak and the dominant interaction is long intermolecular separations. As a result, the equilibrium constant for crystallization is

$$\boldsymbol{K_{crystal}} = \boldsymbol{c_e^{-1}}. \quad (5)$$

To determine the solution of hematin in CBSO, hematin powder were added to CBSO stored in a sealed glass vial and stored at desired constant temperature. Aliquots of solution were removed and the concentration of solution was determined using an extinction coefficient $\boldsymbol{\varepsilon_{hematin}}$ =3.1 ±0.1 $cm^{-1}mM^{-1}$ at λ=594 nm (*61, 62*). The procedure was repeated until measured concentration reached a plateau. The value of plateaued concentration was defined as the solubility at this temperature.

Solubility is a parameter depends on the temperature described by the classical Van't Hoff equation

$$\frac{\partial ln c_e}{\partial \frac{1}{T}} = \frac{\Delta H^{\circ}_{crystal}}{R}, \quad (6)$$

where R is the universal gas constant. To determine the enthalpy of hematin crystallization, the solubility of hematin in CBSO was measured at four different temperatures: 5 ℃, 25 ℃, 37 ℃ and 45 ℃. The final solubility is determined by the mean value of several plateaued concentrations and also confirmed with AFM studies where the step advancement begin to oscillate around that concentration. The result shows that the solubility determined from bulk crystallization has similar value with the one determined from AFM study at 25 ℃. The slope of the c_e data plotted in van't Hoff coordinates ln c_e as a function of (1/T) yields $\Delta H^{\circ}_{crystal} = -37 \pm 8\ kJ\ mol^{-1}$ (*60*).

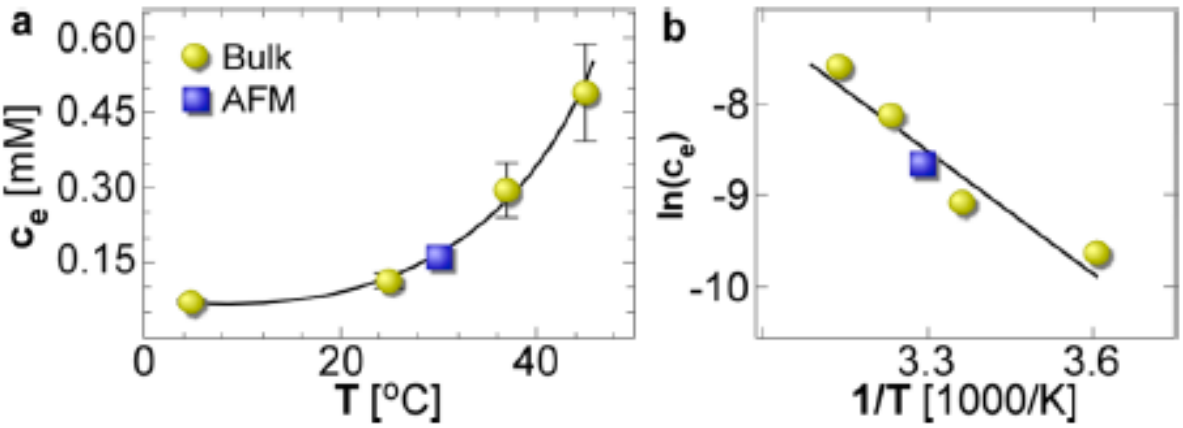

Figure 21. The solubility of hematin in CBSO determined from bulk crystallization experiments (yellow circles) and by in situ atomic force microscopy (blue squares).

The Gibbs free energy of crystallization $\Delta G^{\circ}_{crystal}$ can by determined from solubility measurement. $\Delta G^{\circ}_{crystal}$ is related to the crystallization equilibrium constant $K_{crystal}$ as

$$\Delta \boldsymbol{G}^{\circ}_{\boldsymbol{crystal}} = -\boldsymbol{RT} \ln \boldsymbol{K}_{\boldsymbol{crystal}} = \boldsymbol{RTln}\, \boldsymbol{c}_{\boldsymbol{e}}, \quad (7)$$

and the difference between $\Delta \boldsymbol{H}^{\circ}_{\boldsymbol{crystal}}$ and $\Delta \boldsymbol{G}^{\circ}_{\boldsymbol{crystal}}$ provides the entropy for crystallization $\Delta \boldsymbol{S}^{\circ}_{\boldsymbol{crystal}}$ as

$$\Delta \boldsymbol{S}^{\circ}_{\boldsymbol{crystal}} = \frac{\Delta \boldsymbol{H}^{\circ}_{\boldsymbol{crystal}} - \Delta \boldsymbol{G}^{\circ}_{\boldsymbol{crystal}}}{\boldsymbol{T}}. \quad (8)$$

The enthalpy of crystallization describes the strength of the molecule – molecule interaction. In the crystallization process, the formation of bonds will reduce the total energy of the system. The entropy of crystallization reflects loss of translational and rotational degrees of freedom when a molecule incorporates into the crystalline lattice from the solute, partially balanced by the increase from vibrational degrees of freedom. The magnitude of estimated $\Delta S^{\circ}_{crystal}$ value for hematin crystallization is about -49 J $mol^{-1}K^{-1}$ that is lower than the estimates for molecule with similar size. The discrepancy may indicate that octanol can form ordered structure at the crystal – solvent interface.

2.3.4 Hematin crystallization at the water – octanol interface

Previous study suggested hematin crystalline lattice is composed of a 'head to tail' structure that dimers bound by reciprocal COO^- - Fe (III) coordination bonds and connected through chains of -COOH-HOOC- hydrogen bonds (*57, 63*). The formation of hydrogen bonds is essential to the structure that requires the presence of water and hydrogens ions. Those features of the structure indict the initiation of hematin crystallization happens at the aqueous and organic interface. The pH of the system was

controlled by the citric acid buffet to 4.8 that controls the population distribution of deprotonated hematin molecules.

2.3.4.1 Hematin crystallization from aqueous solution

The dimensions of hematin crystals in vivo are constrained by the size of the DV and the availability of hematin produced during digestion of hemoglobin. The longest crystals extracted from the *P. falciparum* are around the size of 1 μm (*54*). We attempted to growth crystals large than extracted crystals from purely aqueous solution using citric and acetate buffers. Longer crystals were produced with the longest dimension ≤ 3 μm through the morphology is distinctly different from that of hemozoin (*55*). AFM images of crystals grown in acetate buffer were showed in Fig.22. The crystal exhibit block structure and the entire surface rough that the layer of thickness varies from 12 to 63 nm. The missing of sharp crystal edge indicts the crystal is missing crystalline structure. The height of layers is greater than the thickness of single crystal layer in the (100) plane as c = 1.22nm (*57*). Those layered structures suggest the layer was grown under high elastic stress and twinning (*64*).

In summary, hematin crystals grown from aqueous solutions from critic/acetate buffer at pH 4.8 showed incompatibility in shapes and surface features from biological hemozoin. Those discrepancies suggest that biological hemozoin crystals may not grow within a purely aqueous environment.

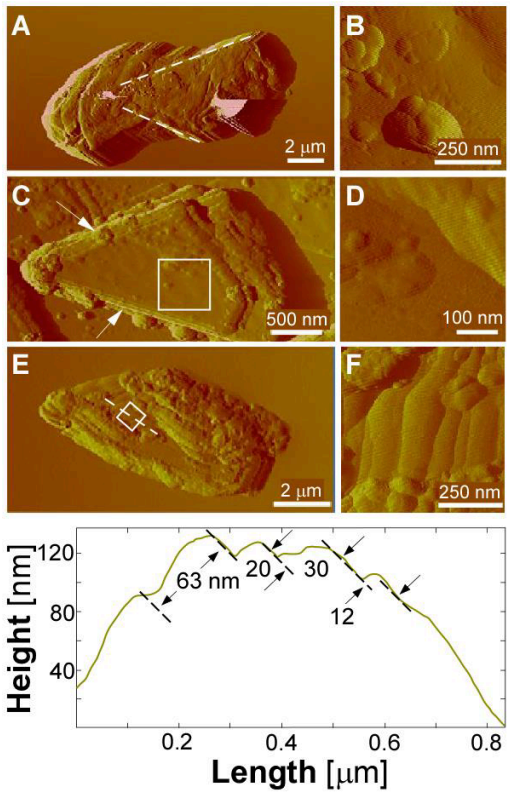

Figure 22. AFM images of features of hematin crystal grown from purely aqueous solution (*65*).

2.3.4.2 Hematin crystallization from CBSO solution

CBSO was used as a surrogate for the lipid sub-phase in the DV for hematin crystallization. Hematin solutions were prepared by dissolving hematin powder in 8 mL of freshly made CBSO and heating it up to 70℃ for 7-9 h. The solution was filtered through a 0.2 μm nylon membrane filter and the concentration was determined using an extinction coefficient $\varepsilon_{hematin}$ =3.1 ±0.1 $cm^{-1}mM^{-1}$ at λ=594 nm (*61, 62*). The filter solution was diluted with fresh CBSO to the concentration 0.20 mM with a total volume of 5 ml. Small crystals were observed on the bottom of vials after 2 ~ 3 days and continue to grow until it reaches the maximum size of 20 ~ 30 μm. The crystals were well faceted and had smooth faces with no visible gaps. According to the unit cell structure of hematin

crystalline (*57*), the crystal displayed clearly cut of (100), (010) and $(0\overline{1}1)$ face and the ratios of area of those faces are comparable to hemozoin crystals found in P. *falciparum.* The x-ray powder diffraction measurement showed similar patterns for hemozoin crystals and synthesized ones (*66*).

In the previous studies, evidence suggested that the nucleation of hematin crystal first happened at the water – organic interface. To understand the location where the first step of hematin crystallization, nucleation, occurs in the CBSO system, CBSO solution was characterized by dynamic light scattering (DLS) method and the result revealed CBSO solution is not homogenous but contains a relatively monodisperse population of scatters with size 120 nm (*67*). The correlation function amplitude disappeared when CBSO solution was diluted with pure octanol indicts that the nanoparticles are aqueous buffer droplets suspending in the octanol solvent. Those small droplets provide huge organic – aqueous interface that promotes the crystal nucleation. Hematin is enriched in the octanol phase suggest that crystals most likely form in the octanol phase and the water droplets accelerate the assembly of hematin molecules by orientating the OH head groups toward the water and then hematin nucleate on the ordered layer of aliphatic tails.

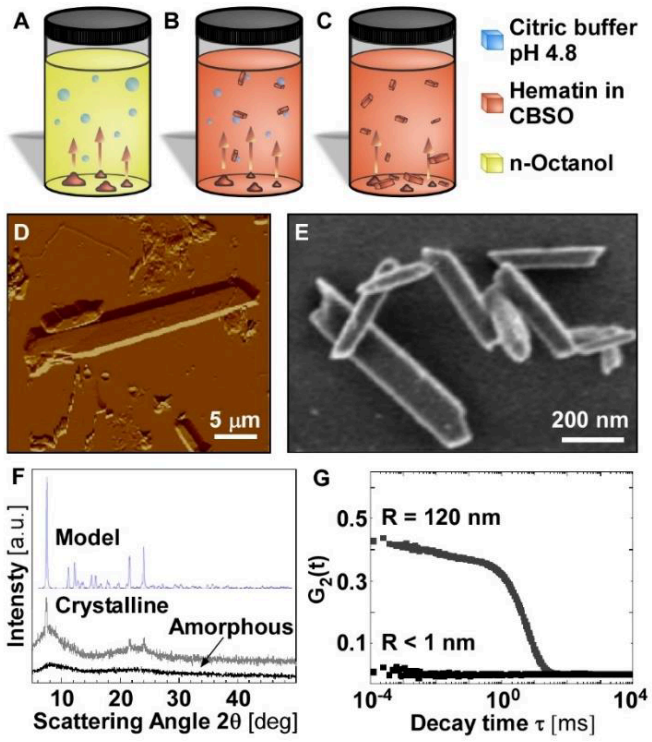

Figure 23. Large hematin crystals grown from CBSO (*55*).

2.4 Solubility of antimalarial drugs in CBSO

To evaluate the effect of concentration of antimalarial drugs on hematin crystallization, solubilities of the five different drugs, chloroquine(CQ), amodiaquine (AQ), quinine (QN), mefloquine (MQ) and pyronaridine (PY) in CBSO (Figure 24) were determined by Megan A Ketchum (*68*) to control the amount of drugs that is available to reach a target site. As artemisinin class don't adsorb visible light, the concentration of artemisinin is determined from mass balance.

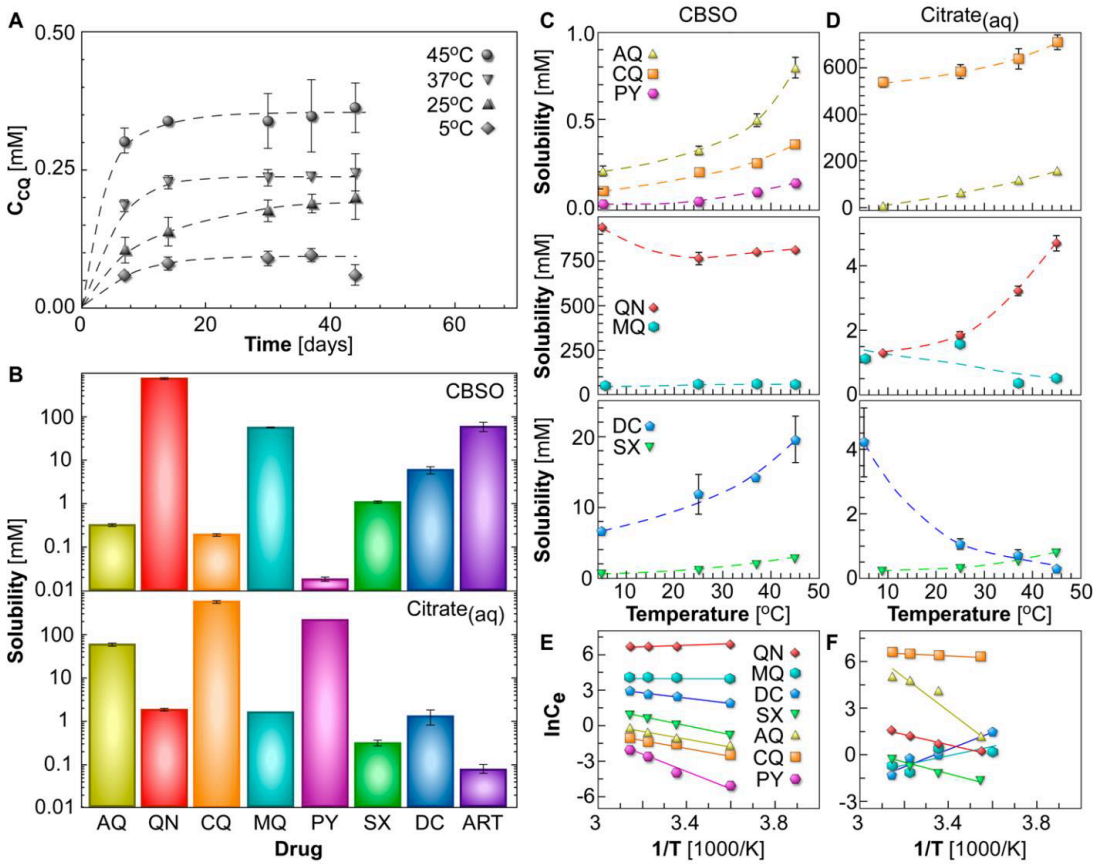

Figure 24. Solubilities of antimalaria drugs (CQ, AQ, QN, MQ, PY). Sulfadoxine (SX) and Doxycycline (DC) are antibodies used for comparison.

Chapter 3. Mechanisms of hematin crystallization

Antimalarial drugs have been used in the treatment of malaria and great progress has been made to reduce the high level of suffering caused by malaria worldwide (*69*). It was proposed that many of quinoline class antimalarial drugs target the hemozoin crystal and stop crystallization process by binding on the crystal surface. The traditional method for discovering new drugs is from screening numerous of drugs with similar structure, which is a costly and time – consuming process (*70*). Understanding the mechanism how antimalarial drugs inhibit the growth of crystal can provide insights in designing new drugs. The in-situ atomic force microscopy (AFM) was employed to monitor the hematin crystal (100) face and provides the first evidence of molecular mechanisms of hematin crystallization. AFM observations demonstrate that hematin crystallization follows classical mechanism that new crystal layers are generated by two-dimensional nucleation attachment of solute molecules.

3.1 The growth mechanism of Hematin crystallization

Does hematin crystallization follow a classical or nonclassical pathway. Is there any intermedium involved in nucleation? Are inhibiters stop the crystallization by occupying specific surface sites, reduce the hematin solution or create a new pathway for crystallization?

To answer those questions, β - hematin was synthesized from CBSO as a replacement of hemozoin crystal. Both natural and synthetic hematin crystals displayed identical habit and defined with [100] for basal faces and [001], $[0\bar{1}\bar{1}]$ for sides (*66, 71*).

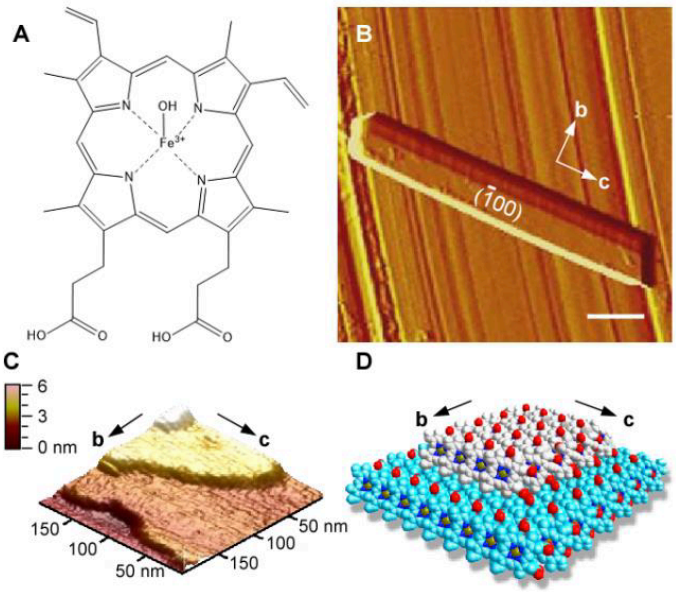

Figure 25. (a) Hematin molecules. (b) AFM image of a hematin crystal. Scale bar equals 2 μm. (c) AFM image displayed in 3D. (d) Molecular model of β - hematin.

3.2 The environment for in-situ growth

Hematin crystals were grown on glass disks as described above. The density of attached hematin crystals was monitored under an optical microscope. We ensured similar crystal density for all samples to minimize potential depletion of inhibitors due to high crystal number. The glass slides were mounted on AFM sample disks (Ted Pella Inc.) and the samples were placed on the AFM scanner. The environment of digestive vacuole was simulated by CBSO solutions that provide both liquid membrane from octanol solution and aqueous – organic interface from the citric buffer droplets. Hematin dissolved in the CBSO solution was used for the growth of unfinished layers.

The temperature of the growth solution within the AFM fluid cell during *in situ* crystal growth monitoring was measured with a copper-constantan thermocouple connected to a temperature controller (SE5010, Marlow Industries Inc.). The

thermocouple was calibrated using a crushed ice/DI water bath. The bath was allowed to equilibrate for 30 minutes after which the water freezing point was verified at several locations with an accurate (±0.1°C) mercury thermometer. The thermocouple tip was secured to the thermometer. The set point of the controller was adjusted to read 0.0 ± 0.1°C. The thermocouple was embedded in a brass disk positioned right under the AFM sample. The liquid cell was sealed with a silicon O-ring and loaded with CBSO. To replicate the experimental conditions, we continuously imaged for 3 hours a 2×2 μm^2 area at a scanning rate 2.52 s^{-1}. The temperature in the fluid cell reached a steady value of 27.8 ± 0.1°C within 15 min of imaging (*72*).

3.3 Hematin crystallization in Various solvent.

We used a multimode atomic force microscope (Nanoscope IV) from Digital Instruments (Santa Barbara, CA) for all AFM experiments. AFM mages were collected in tapping mode using Olympus TR800PSA probes (Silicon nitride, Cr/Au coated 5/30, 0.15 N/m spring constant) with a tapping frequency of 32 kHz. Image sizes ranged from 300 nm to 20 μm. Scan rates were between 1 and 2.52 s-1. Height, amplitude, and phase imaging modes were employed. The captured images contained 256 scan lines at angles depending on the orientation of the monitored crystal (*62, 73*).

Contact mode images were used in select cases to help visualize surface features; however, all in situ measurements were performed in tapping mode to minimize the possibility of disturbing solute and/or growth modifier attachment to crystal surfaces. Tapping mode images were collected at a tapping frequency of 32 kHz.

Hematin crystal growth was tested in three different condition (hematin dissolved in acetic acid buffer, pure octanol and CBSO) by Katy Olafson to exploit the necessity of aqueous – organic interface for activating the growth. For each growth solution, crystal surface was monitored with in situ AFM for 48 hours. steps of hematin crystals on (100) surface merged in the hematin solutions dissolved in acetic acid buffer, pure octanol stay stationary for a long period of time while advances in the CBSO solution.

3.3.1 Hematin crystallization in acetic acid

Hematin was dissolved in the 0.1M NaOH and titrating with acetic acid to the desired pH. Steps were first observed on the basal surface and become observed with increased time of exposure to the acetic solution. Different from the head-to-tail structure in the organic solution, hematin molecules can form several dimers and higher oligomers through the π - π interactions. Molecules are parallel to each other for maintaining the overlap of π electron density (*74*). Those species of dimers may coat the hematin crystal surface and lead to the disappearance of steps.

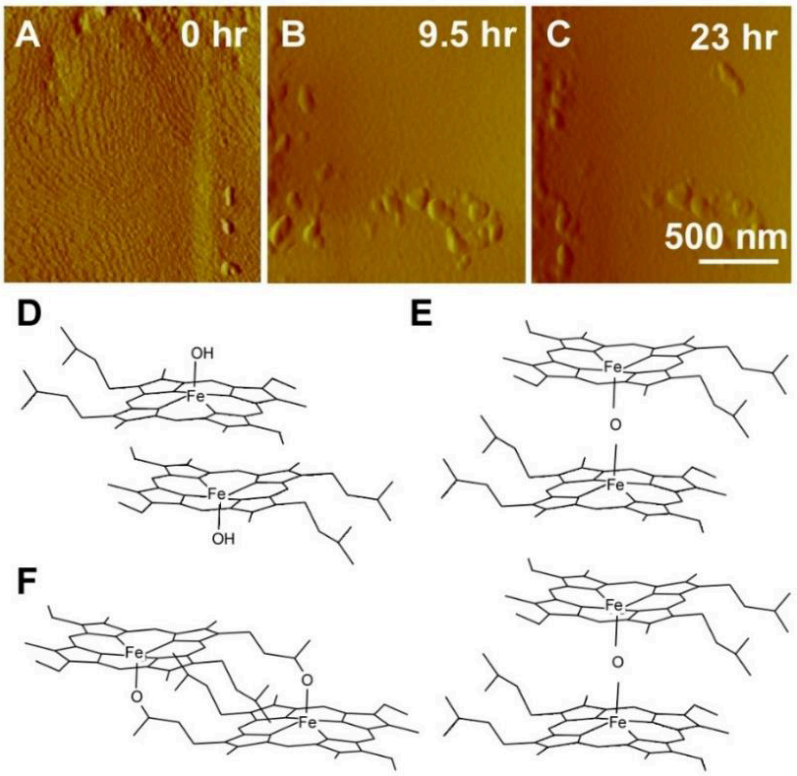

Figure 26. (a – c) AFM images of the evolution of hematin (100) surface contacted in hematin dissolved in acetic buffer. (d – e) The structure of hematin dimers.

3.3.2 Hematin crystallization in octanol solution

AFM studies observation revealed that in anhydrous n – octanol, the steps of crystal surface will retract at the solubility of hematin in CBSO that indicts the solubility is even greater in octanol. At the concentration higher than the solubility in octanol, the 48 hours continuous scanning displayed that the step almost stays stationary. The result indicts that droplets of acetic acid buffer is necessary both for hematin nucleation and growth.

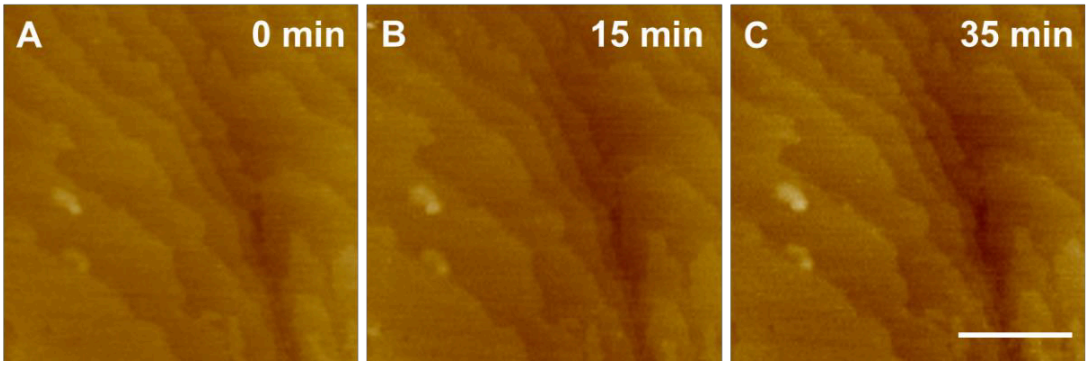

Figure 27. AFM images of (100) hematin surface in contact with hematin dissolved in octanol. Steps remain stationary for 40 mins. Scale bar is 250 nm.

3.3.3 Hematin crystallization in CBSO

Hematin solution in CBSO with concentration of 0.28 mM was prepared less than 2 h in advance. This solution was loaded into the AFM liquid cell using 1 mL disposable polypropylene syringes (Henck Sass Wolf), tolerant of organic solvents. After loading, the system was left standing for 10 – 20 mins to thermally equilibrate. The crystal edges were identified to determine the orientation and the crystallographic directions on the upward-facing (100) crystallographic surface. The crystals were kept in contact with the solution for 0.5 – 1.5 h to allow their surface features to adapt to growth conditions. We set the scan direction parallel to the [001] crystallographic direction and AFM images were collected for 3 – 5 h. The solution in the AFM fluid cell was refreshed every 30 min to maintain constant concentration.

The AFM study revealed that (100) surface of hematin crystal follows a classical layer-by-layer mechanism that 2D nucleus generated on the surface and spread by the attachment of hematin molecules. The rate of step advancement is proportional to the concentration of hematin solution and follow first order kinetic with a step kinetic

coefficient $\beta = 4.3\ \mu m\ s^{-1}$ in the fastest growth direction. CBSO can dissolve the hematin crystal and lead to the step retreatment. The rate of retreating is nearly symmetric to the rate of advancing according to the solubility.

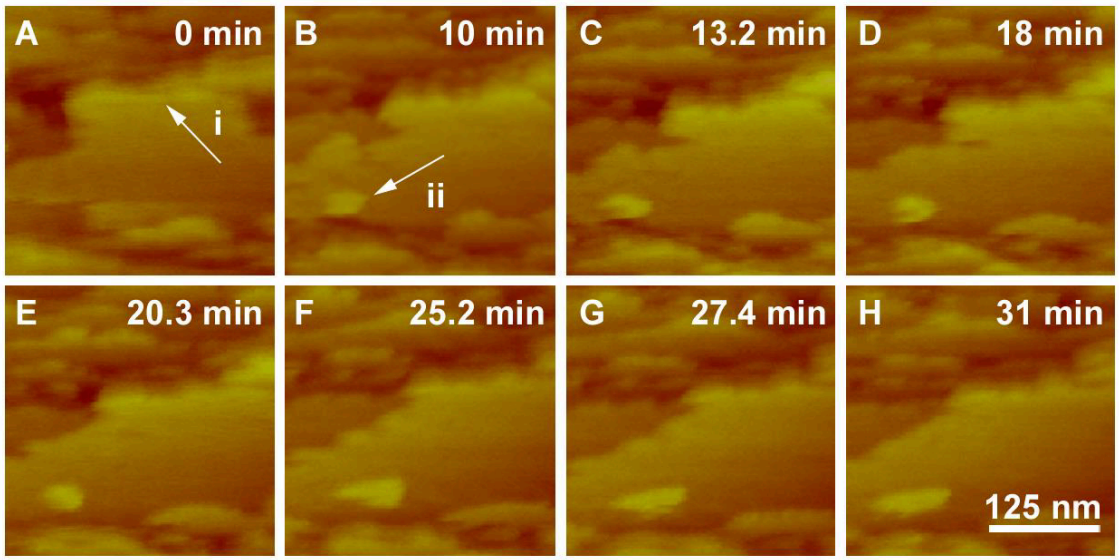

Figure 28. AFM images of the evolution of (100) surface in CBSO with hematin concertation 0.21 mM (*75*).

3.4 Characterization of hematin crystallization

The evolution of the hematin crystal surface was characterized by the velocity of growing steps ν and the rate of two-dimensional nucleation of new crystal layers J_{2D}. To determine ν, we monitored the displacements of 8 – 13 individual steps with a measured step height h = 1.17 ± 0.07 nm. Between 25 and 35 measurements were taken for each individual step and the average growth rates were reported. To determine J_{2D}, the appearance of new islands on the surface between successive images was monitored and the number of islands that grew was counted. This number was scaled with the imaged

area and the time interval between images to yield J_{2D}. From 15 to 25 measurements were averaged for each $\boldsymbol{J_{2D}}$ determination.

3.4.1 2D nucleation on hematin surface

According to classical nucleation theory, the rate of 2D nucleation is determined by the free energy

$$\boldsymbol{J_{2D}} \propto \mathbf{exp}\left(-\frac{\boldsymbol{\Delta G^*_{2D}}}{\boldsymbol{k_B T}}\right), \tag{9}$$

with the free energy barrier for layer nucleation

$$\boldsymbol{\Delta G^*_{2D} = \pi \gamma R_{crit} h.} \tag{10}$$

The critical size of a 2D nuclei is defined as the radius that lead to the maximum of free energy. At the critical point, the 2D nuclei stands 50% percent chance to grow or dissolve. The critical radius R_{crit} for layer nucleation is defined as the threshold size above which an island has a higher probability to grow. Islands of size $R < R_{crit}$ are more likely to dissolve. We monitored the size evolution of all newly generated islands employing time-resolved sequences of *in situ* AFM images and classified the islands as growing or dissolving. The largest sizes reached by dissolving islands and the threshold, above which all islands grew, were averaged to yield R_c. We determined from 25 to 30 independent $\boldsymbol{R_c}$s.

The dependence R_{crit} is governed by the Gibbs – Thomson relation that expressed with the equation

$$\boldsymbol{R_{crit} = \Omega \gamma / k_B T ln\left(\frac{C_H}{C_e}\right)}, \tag{11}$$

where $\boldsymbol{\Omega}$ is the volume of a molecule equals to 0.708 nm^3; $\boldsymbol{\gamma}$ is the surface free energy of the layer edge; $\boldsymbol{k_B}$ is the Boltzmann constant; T is the temperature; C_H is the hematin concentration; and c_e is hematin solubility in CBSO. Katy Olafson determined the critical radius of 2D nucleus related to different hematin concentrations and compared with the prediction from CNT (*58*).

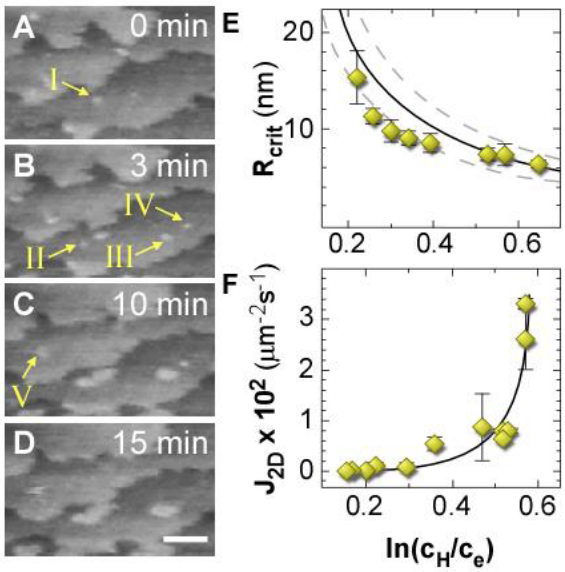

Figure 29. 2D nucleus generated on the (100) hematin surface. The critical size reduces and the rate of nucleation increases exponentially with boasting concentration.

3.4.2 Determination of step velocity

The spread of 2D nucleus lead to the formation of new layers. Layers merge with adjacent layers and eventually cover the entire face. The step velocity v was determined from displacements of individual steps measured from successive AFM images. The growth along the $\overline{\boldsymbol{c}}$ showed a faster step velocity that is consistent with the bulk crystal habit. The step velocity along $\overline{\boldsymbol{c}}$ direction was reported in Katy Olafson's work (*62*).

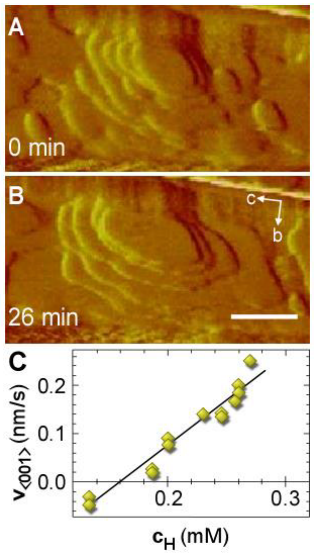

Figure 30. The evolution of 2D nucleus generated on the (100) surface.

The step velocity v shows a linear dependence on hematin concentration. The cross-section between the line and the x axis indicts the solubility of hematin in CBSO, which is consistent with the result from bulk experiment. According to the CNT, step velocity can be expressed as

$$\boldsymbol{v = akΩ(c_H - c_e),} \tag{12}$$

where a is the molecule size and k is the effective first-order rate constant.

3.5 Pathways of incorporation

Molecules can propagate via both direction incorporation from bulk solution and molecules adopted on the terrace and then diffuse into kink sites. For directly incorporation, the solvent structure on the surface and kink sites and the water molecules around solute in the solution make great contribution to the kinetic barrier as the solvent in the kinks have to get replaced by the solute molecule for crystal step advancement (*76,*

77). For surface diffusion, the energy barrier is comprised of several different stages. As solute first adsorb on the terrace and then diffuse to kink sites, the first kinetic energy barrier is determined by the bond strength between surface and solute and interaction between solvent molecules and solute. When molecule is travelling along the surface with a three-dimension network of solvent structure, the molecule passes a bunch of small energy barriers. After the solute molecule reached the kink sites, it removes the solvent molecule and attach to a growth site (*78, 79*).

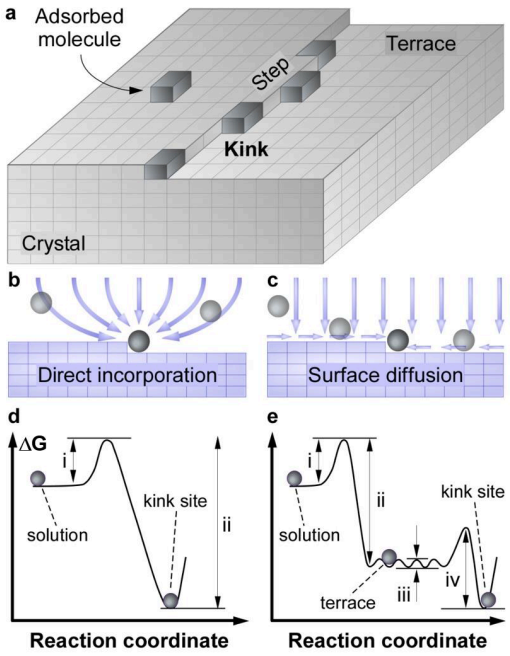

Figure 31. Schematic of direct incorporation and surface diffusion.

3.6 Surface diffusion for hematin crystallization

To understand the pathway of molecule incorporation for hematin crystal, the dependence of step velocity on interstep distance was measured. Observations revealed that closely spaced steps move significantly slower than separated steps. The dependence

of step velocity on the interstep distance was expressed with equation studied in Cabrera and coworkers' work (*80*)

$$\boldsymbol{v} = \frac{\boldsymbol{\lambda}}{\boldsymbol{h}}\frac{\boldsymbol{\Omega D}}{\boldsymbol{\Lambda}}(\boldsymbol{c_H} - \boldsymbol{c_e})[\frac{\boldsymbol{\Lambda s}}{\boldsymbol{\lambda}} + \frac{\mathbf{1}}{\mathbf{2}}\mathbf{coth}\frac{\boldsymbol{l}}{\mathbf{2}\boldsymbol{\lambda}}]^{\mathbf{-1}}, \quad (13)$$

$\boldsymbol{\lambda}$ is the characteristic length of surface diffusion and D is the diffusivity of the hematin molecules in the solution. $\boldsymbol{\Lambda}$ describes the resistance for molecule to adsorb form bulk solution to the crystal surface. $\boldsymbol{\Lambda_s}$ is the resistance for molecule to incorporate into kinks from the surface. D is the surface diffusivity.

The advancement of layers with different interstep distance was monitored with in-situ AFM. The disabled y axis scan was utilized to monitor the evolution of a line on the step with the step height around 1.2nm. Figure 32c displayed the separation of two layers where the edge i is well separated from the surface below and step ii is closed packed with edge i from the beginning (*75*). The growth rate for step i and step ii were recorded. The result shows that the growth rate of step i is comparable to the growth rate measured in the previous experiment while the step ii is only fluctuated. The result indicated that the surface diffusion plays an important role in hematin crystallization and the supplies reach kinks only from the lower terrace. The step velocity reaches a plateau as the amount of solute adsorbed on the surface reached the limitation of molecules transferred from surface diffusion.

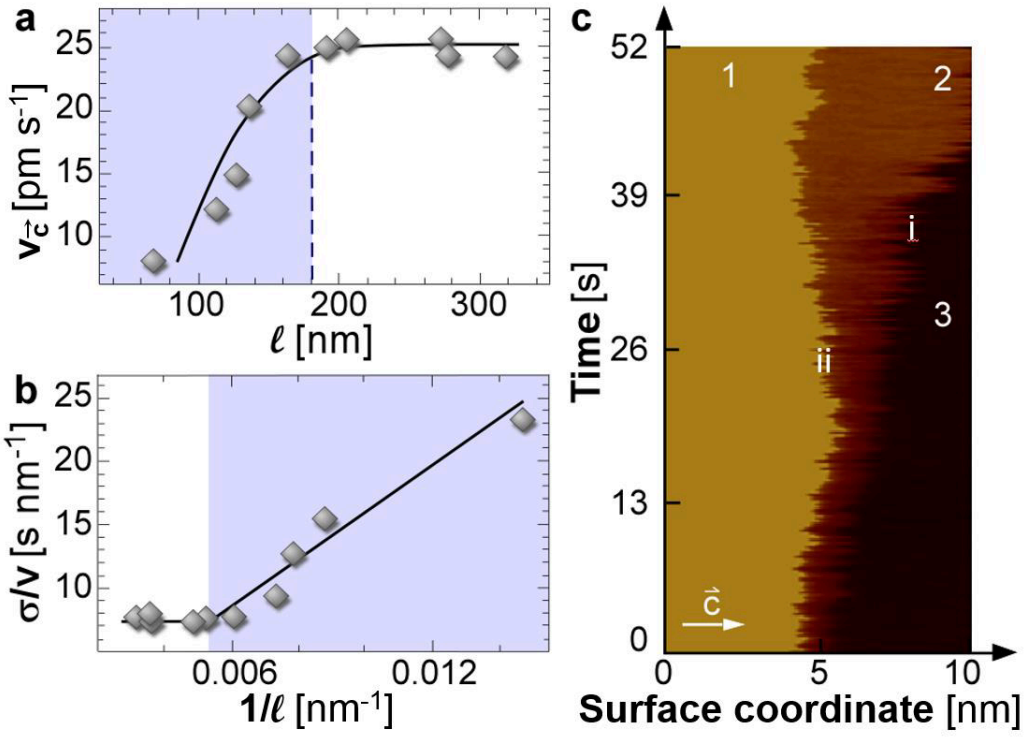

Figure 32. The evolution of step edge monitored with disabled y axis scan.

Chapter 4. Mechanism of antimalarials on hematin crystallization

The pathology pathways of malaria, gout, kidney stones, and other aggregation diseases incorporate crystallization and its inhibition is the target of drugs that are often combined for increased efficacy (*24, 29, 81-83*). Hematin is a toxic byproduct of hemoglobin digestion in malaria parasites and suppression of its sequestration into inert hemozoin crystals is a favored approach to parasite elimination (*84, 85*). Two or more hematin crystallization blockers have been combined in state-of-the-art antimalarial regimens and extensive efforts have failed to deliver molecular-level understanding of the synergy or antagonism between the partner drugs (*86, 87*). Here we demonstrate that drug pairs, whose constituents employ distinct mechanisms of hematin crystallization inhibition, kink blocking and a step pinning (*62, 88*), exhibit both synergistic and antagonistic cooperativity depending on the drug combination and applied concentrations. Whereas synergism between two crystal growth modifiers is expected, the antagonistic cooperativity defies current crystal growth models. We demonstrate that the kink blockers reduce the line tension of the step edge, which facilitates both the nucleation of new crystal layers and the propagation of the steps through the gates created by step-pinners. The molecular viewpoint on synergistic and antagonist cooperativity between crystallization modifiers provides guidance on the pairing of drugs in malaria combination therapies and the understanding and control of physiological and pathological crystallization.

4.1 Step pinging and kink blocking antimalarial drugs

For solution grown crystals, two classes of inhibition of step propagation are discussed. In the first mechanism, known as step-pinning, inhibitors bind to flat terraces and arrest step growth over broad areas of the crystal surface. Alternatively, inhibitors may associate and block kinks, the sites where solute molecules incorporate into steps. We examine the growth of beta-hematin crystals, a component of the physiology of malaria parasites, in the presence of artemisinin and quinoline derivatives, drugs that represent the current front line of antimalarial defense.

For studies of modifiers, growth solutions were replaced with ones containing a selected antimalarial inhibitor(s). With each modifier concentration, AFM images were collected for two to four hours, during which the solution was replenished several times. Solution with no modifier was pumped into the AFM cell and the observed crystal was allowed to grow uninhibited for about 30 min before another modifier concentration was introduced.

We used four antimalarial drugs: quinine (QN), chloroquine (CQ), amodiaquine (AQ), and mefloquine (MQ). Solid QN and MQ were added to CBSO and the solutions reached the desired concentration after 2 - 4 days. AQ and CQ were added in excess to CBSO and stored in the dark for 30 - 45 days, allowing the concentrations to approach the respective solubilities (*68*). All drug solutions were filtered through 0.2 μm nylon membrane filters and the concentrations were determined by UV–vis spectrometry using

a Beckman DU 800 spectrophotometer and extinction coefficients and wavelengths listed in from Ketchum, *et al.* (*68*).

From AFM measurements, all four drugs lead to slower step growth, fewer 2D nuclei, and more rugged step edges. On the contrary, CQ and QN, follow the step pinning mechanism, can fully cease both the step advancement and nucleation at high drug concentration while MQ and AQ, follow the kink blocking mechanism, can partially reduce the growth and nucleation rate (*75*).

4.1.1 step pinning antimalarials

The mechanisms of antimalarial drugs to stop hematin crystallization was proposed by Sullivan for quinoline drugs (*89*). In previous studies (*62*), Katy Olafson monitored the evolution of hematin (100) surface in the presence of different concentration of various antimalarial drugs and characterized with rate of step growth and nucleation, shown in Figure 33.

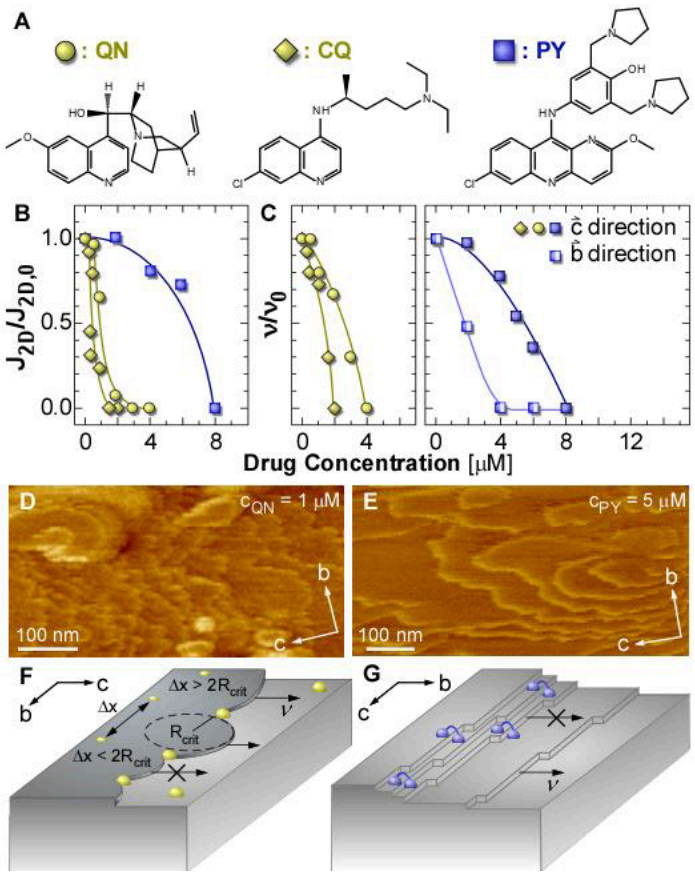

Figure 33. The rate of step velocity and nucleation in the presence of CQ, QN and PY.

At intermediate inhibitor concentrations, QN and CQ lead to an exponential decay in J_{2D} and v with increasing drug concentration, accompanied with corrugated steps and closely packed intersteps. Steps are fully ceased at high concretions of antimalarial drugs, which is around 2 μM for CQ and 4 μM for QN. Observations indicated that CQ and QN stop crystallization by step pinning mechanism in which modifiers adsorbs on the terrace and form gates. The distance of these gate is determined by the spacing of modifiers on the structure. If the separation distance is smaller than $2R_{crit,}$ the step will be curved as the step is trying to pass a gate that raising the surface tension for creating more surface

areas. The phenomena creates a under saturation for the advancing steps and growth is arrested (*90*).

4.1.2 Kink blocking antimalarials

AFM measurements of AQ and MQ on v and J_{2D} revealed that modifiers can alter crystal growth with a different mechanism. Both AQ and MQ showed a weaker impact on inhibiting crystallization a border concentration that leads to a minimum of rate of growth and nucleation. Beyond the boarder, future increase concentration of drugs does little impact on changing the inhabitation effectiveness. The mechanism in which modifier can adsorb into a kink and reduce the number density of kink sites refers to kink blocking. No observed change in the step velocity or nucleation when artemisinin class drugs were applied though they work as the frontline against malaria. ART is believed to attain inactivity before the reduction of the endoperoxide bridge by fe(II) heme (*35, 40*).

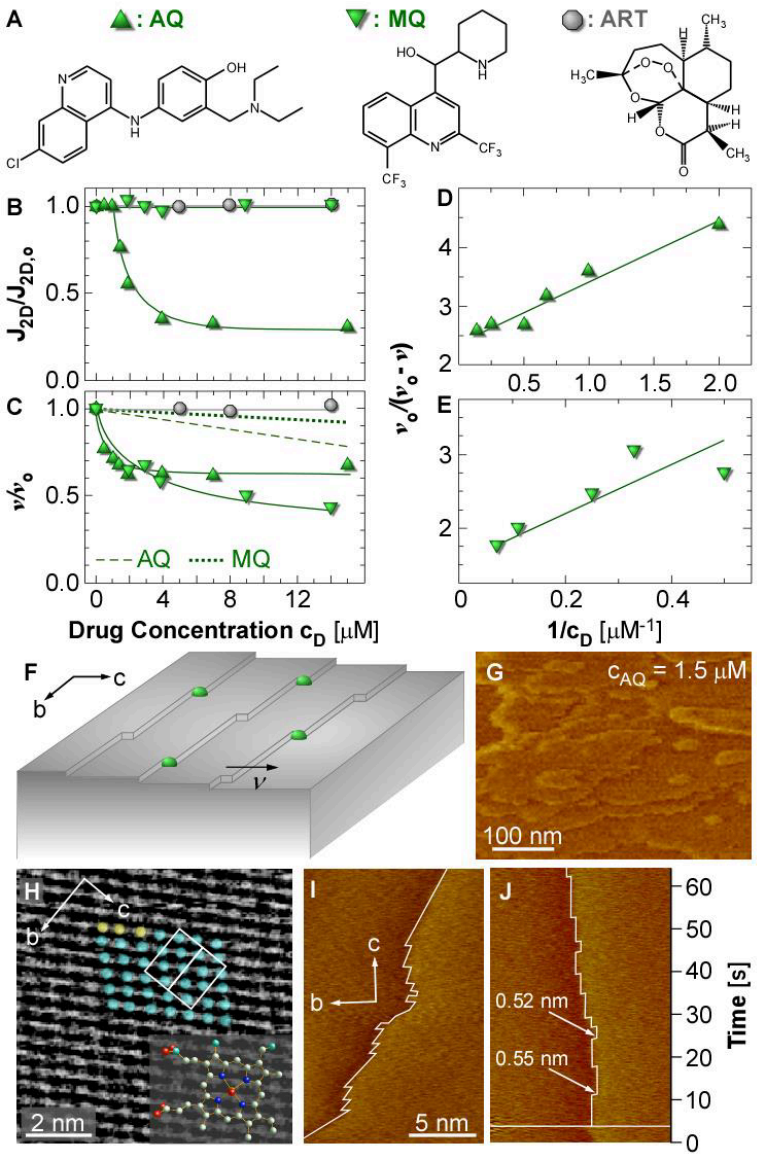

Figure 34. MQ and AQ inhibit the hematin crystallization by the mechanism of kink blocking.

4.2 antimalarial drugs effects hematin bulk crystallization.

To have a general understanding how drugs effect the crystal growth in all directions, bulk assays of hematin crystallization were performed with varying concentrations of six drugs: CQ, QN, AQ, NQ PY and ART.

The length and width of crystals grown for 16 days were measured by Katy Olafson (*75*). Generally, in the presence of CQ, QN, PY and AQ, crystal appears a shorter average crystal length, indicating that (001) and $(0\bar{1}\bar{1})$ are potentially preferred surfaces to bind. Additionally, CQ can suppress growth of the axial faces, where QN, PY and AQ have identical effects on the lateral and axial faces. ART does inhibit the growth that is consistent with AFM data.

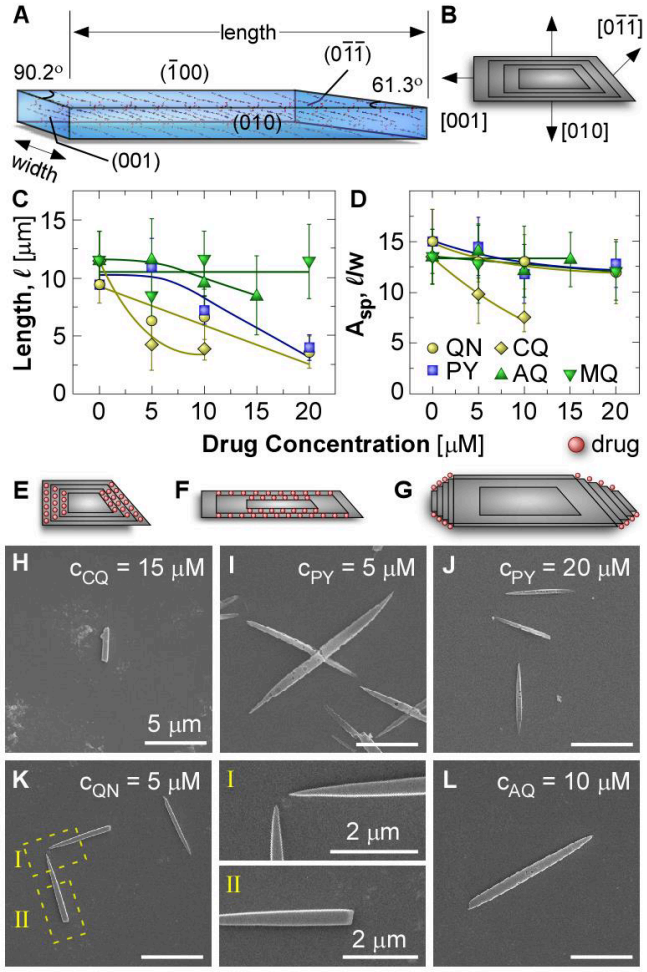

Figure 35. The measured lengths and widths for hematin bulk assays.

4.3 Identifying the active species responsible for inhibition

Previous studies indict that antimalarial drugs can inhibit the growth of hematin solution by binding to selectively sites. While the UV-vis tests indicated that complexation between antimalarials drugs and hematin formed in the solution, questions still remain that what are the effectiveness species participating into sites or antimalarial drugs simply stop the crystallization by reducing the concentration of hematin. To answer those questions, hematin solution was titrated with various of antimalarial drugs and the adsorption was monitored with UV-Vis (*75*). The spectra data showed that hematin can form complexes with QN, CQ, AQ and MQ while no complexes for PY and ART.

The concentrations required to cease hematin crystallizations are 0.09 mM and 0.07 mM for QN and CQ which are 20-fold higher than the concentrations concluded from AFM studies. Those Considerations suggest that the interactions between antimalarials and hematin surface play a more important role in inhibiting hematin crystallization.

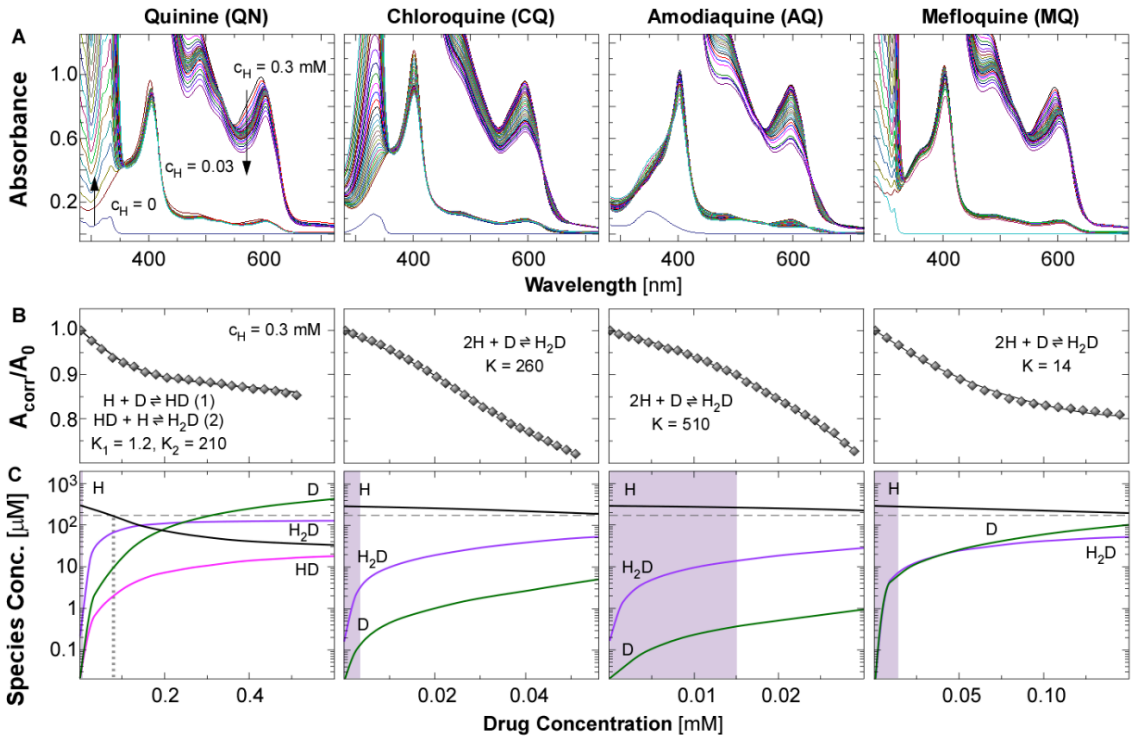

Figure 36. Spectra of drug – hematin complexes determined form UV-Vis.

Chapter 5. Combination Therapy and cooperativities between antimalarial drugs.

Recent work established that that β-hematin crystals, a synthetic analogue to hemozoin, follow classical growth mechanisms, whereby new layers nucleate on the crystal surfaces and advance by incorporation of solute molecules at the layer edges, the steps (*62*). These studies uncovered two unique classes of quinoline inhibition of step propagation (*88*). In a first mechanism, known as "step-pinning," the drugs chloroquine and quinine bind to flat terraces and arrest crystal formation over broad areas of the crystal surface (*91*). Second, the drugs amodiaquine and mefloquine were found to largely only bind and block the kinks, the sites where hematin molecules add to steps (*62*).

Combinations of two or more drugs constitute the main line of current antimalarial defense (*92*). The studies of the joint action of pairs of drugs have been confined to parasite responses (*83, 86, 87*) and a crucial gap of understanding of the interactions between pairs of drugs on hemozoin inhibition has been identified (*87*). To address the molecular mechanism of action of pairs of drugs on hematin detoxification we combine a step pinner, chloroquine (CQ) or quinine (QN), with a kink blocker, mefloquine (MQ) or amodiaquine (AQ). We classify the cooperativity between paired drugs as synergistic, additive, or antagonistic according to whether the response to a combination of two drugs is, respectively, stronger, equal, or weaker than the sum of the responses to individual doses (*93*).

We propose an alternative classification of cooperativity, based on the derivatives of the step velocity with respect to the two inhibitor concentrations. The criterion that

we propose states that if the signs of both derivatives are negative, the cooperativity is synergistic; antagonistic cooperativity ensues if these derivatives are of opposite signs. A numerical evaluation of the two derivatives suggests a kinetic state diagram, in which the space of the concentrations of two inhibitors is divided into two fields: a field of synergy at low concentrations of either inhibitor, and a field of antagonism, where the concentrations are high. Again, the complex nonlinearity of the derived relations hampers straightforward predictions on the consequences of stronger adsorption of any of the inhibitors on the cooperativity. These relations, however, can be evaluated numerically to address this and other question related to the inhibition of step velocity.

5.1 Combination therapy

The usage of combined antimalarial drugs predominantly reduced the risk of malaria (94). Combination therapy achieved great successes in reducing the side effects of antimalarial drugs and reduced the rate of development of drug resistance. Some studies have examined the efficacy of drug combinations with two traditional drugs (95). Newer fixed combination drugs, some using an artemisinin component, are being developed or marketed (96).

Even though combinations of two or more crystal growth inhibitors are common in many drug formulations (92), a crucial gap in the understanding of interactions between inhibitor pairs that regulate hematin crystallization has been identified (83, 87). To address the molecular mechanism of action of binary inhibitor combinations on β-hematin crystal growth we pair a step pinner, chloroquine (CQ) or quinine (QN), with a kink blocker, mefloquine (MQ) or amodiaquine (AQ). We classify the cooperativity

between paired inhibitors as synergistic, additive, or antagonistic according to whether the response to a combination of two inhibitors is, respectively, stronger, equal, or weaker than the sum of the responses to individual doses (93).

5.2 Complexations in the two-drug system

The aim of these tests was to find out whether binary complexes between paired inhibitors form and reduce the inhibitor concentrations. Spectroscopic characterization of solutions of the tested inhibitors reveals that the sum of the UV-vis absorbances of individual inhibitors is approximately identical to the absorbance of their combination. Moreover, no shift in absorbance peaks was observed after mixing. These results suggest that it is unlikely that complexes between two inhibitors form.

Complexes formed between hematin and antimalarial inhibitors were discussed by Egan and coworkers *(97, 98)* and the complexation constants between hematin and antimalarial inhibitors in CBSO were reported by Olafson *et al.* (*88*). Using established protocols, we tested for the complexation between hematin and four inhibitor pairs: QN/AQ, QN/MQ, CQ/AQ, and CQ/MQ. The two tested inhibitors were dissolved at equal concentrations in CBSO and 2 mL of this stock were mixed to a final concentration determined by the lower inhibitor solubility. Fresh hematin stock was diluted with CBSO to a concentration of 0.38 mM and then titrated with a solution of the inhibitor pair. At each titration step, the solution was gently stirred 8 – 10 min to complete complexation and a 350 mL aliquot was drawn for UV-vis spectrometry. The UV-vis adsorptions at 594 nm were measured for 40 titration steps and rescaled to account for the dilution. The

absorbance A_i was compared with a theoretical curve calculated from the complexation constants of the two tested inhibitors.

The absorbance at around 594 nm displayed a clear shift to higher wavelengths after the addition of the inhibitor mixture, which indicates the formation of complexes. We calculated the theoretical A_{corr}/A_0 values for four different models for each combination and chose the best fit from the minimal mean squared deviation between experimental and theoretical A_{corr}/A_0 values. Nonzero deviations suggest the formation of complexes. The UV-Vis spectra of solutions containing two inhibitors and hematin indicate that in all four combinations, even if new complexes exist, their concentration would be limited to a level that does not appreciably attenuate the concentration of antimalarial inhibitors in solution. Therefore, the sequestration of inhibitors due to the formation of ternary inhibitor-hematin-inhibitor complexes is unlikely to be significant.

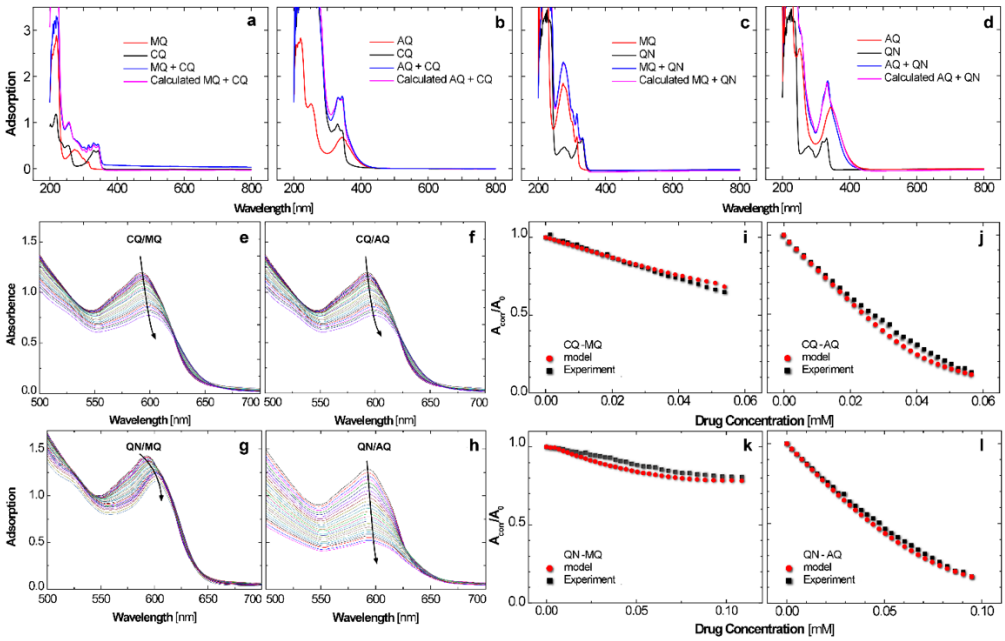

Figure 37. Lack of complexation between kink blockers and step pinners in the solution.

5.3 Hematin bulk crystallization in the presence of combined drugs

The binary drug combinations impose dramatic changes in the shapes and dimensions of β-hematin crystals (Fig. 1d). The crystal length along the *c* crystallographic axis reports the sum growth in $[001]$ and $[0\overline{1}\overline{1}]$ directions (Fig. 1 e and f). The shorter average length enforced by both MQ and CQ than by of CQ alone indicates strong synergy of the activity of these two drugs (Fig. 1g). Since the crystal length is insensitive to the presence of MQ alone (*88*), additive cooperativity of CQ and MQ would engender crystal lengths similar to those constrained by CQ only. By contrast, the crystal lengths affected by the AQ and CQ pair are significantly longer than those commanded by CQ, implying antagonistic cooperativity between AQ and CQ. The addition of either MQ or AQ to CQ-containing solutions enforces length/width crystal aspect ratios A_{sp} that are lower than those with solitary CQ (Fig. 1h). The crystal width increases owing to growth in the $\langle 010 \rangle$ directions (Fig. 1e) and the lower A_{sp} indicates that the MQ/CQ and AQ/CQ pairs impede growth in the Error! Bookmark not defined. faces less than CQ on its own. Since both MQ and AQ weakly affect A_{sp} (*88*), the aspect ratio responses to these two drug combination present additional two examples of antagonistic cooperativity. In contrast to CQ, combining QN with MQ and AQ elicits synergistic response of the crystal length along the *c* axis (Fig. 1i). The A_{sp}s are similar to those driven by QN for the lower MQ and AQ concentrations (Fig. 1j), indicating that the MQ/QN and AQ/QN pairs cooperate synergistically in inhibiting growth along the *c* axis. Higher MQ and AQ concentrations introduce significant decline in A_{sp} relative to that dictated by solitary QN, implying a cooperativity shift toward antagonistic.

The synergistic and antagonistic cooperativities of the four tested drug combinations, exposed by the length and aspect ratio responses of β-hematin crystals, are relatively weak. Moreover, in select drug concentration ranges (e.g., C_{CQ} < 1 μM and C_{MQ} < 4 μM) synergism in suppressing growth along the *c* direction accompanies antagonistic cooperativity towards growth in the *b* direction (Fig. 1g and h); the opposing responses are likely defined by the selective binding of the drugs to the individual crystal faces dictated by their distinct structures (*24, 100*). Importantly, they further weaken the synergy of the CQ and MQ in inhibiting hematin sequestration into crystals. The weak synergy is consistent with the results on the interaction between CQ/MQ and CQ/AQ drug pairs in suppressing several strains of *P. falciparum* (*83, 87*).

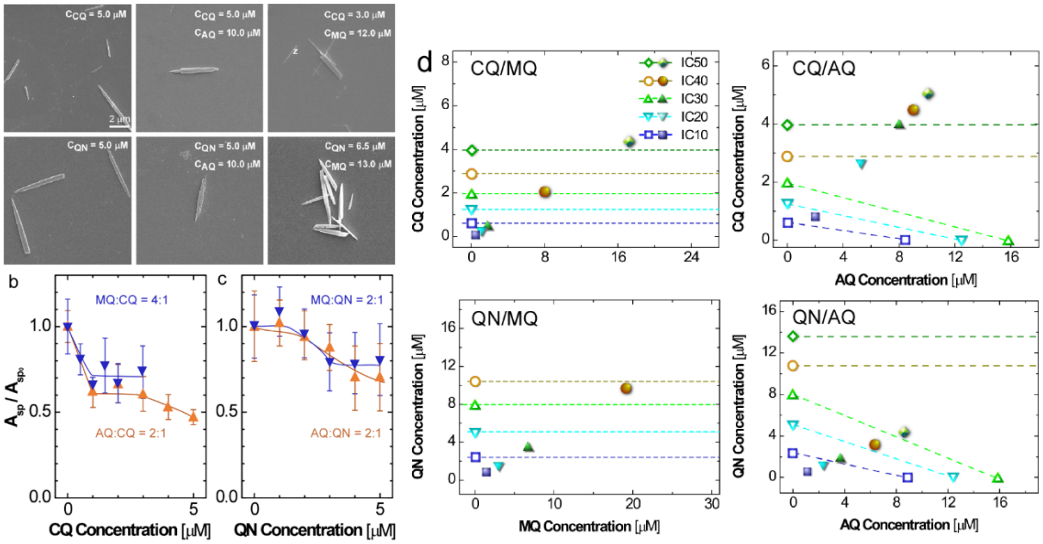

Figure 38. Effects of step pinners and kink blockers on bulk hematin crystallization.

Antagonistic cooperativity between crystallization inhibitors appears counterintuitive. For a facile explanation, we examine whether the constituents of a drug pair form solution complexes that do not inhibit crystallization. Such complexation would

lower the concentration of the active drug forms and constrain their potency. We tested the formation of CQ/MQ, CQ/AQ, QN/MQ, and QN/AQ binary composites. Considering that the tested drugs form complexes with hematin (*88, 98*), we also explored whether these four drug combinations assemble into ternary compounds that include hematin. Results presented in the previous data demonstrate that no complexes involving both drugs exist in the solution and imply that complexation between the applied drugs is not the reason for the observed antagonistic cooperativity.

5.4 Step evolution of (100) surface in the presence of combined drugs

To gain molecular-level insight into the mechanisms of cooperativity between crystallization modifiers, we examine the growth of β-hematin crystals, which form in malaria parasites as a part of their heme-detoxification mechanism (*41*), in the presence of quinoline compounds that represent a major class of the currently employed antimalarials (*47, 48*). Recent work established that β-hematin crystal growth follows classical mechanisms whereby new layers nucleate on the crystal surfaces and advance by incorporation of solute molecules at the steps (*62*). These studies uncovered two distinct classes of quinoline inhibition of step propagation (*88*). In the first mechanism, known as "step-pinning," chloroquine and quinine (Fig. 1a) bind to flat terraces and arrest crystal formation over broad areas of the crystal surface (Fig. 1b) (*91*). Alternatively, amodiaquine and mefloquine were found to block kinks, the sites where hematin molecules incorporate into steps (*62*).

For this study, we used four antimalarial drugs: quinine (QN), chloroquine (CQ), amodiaquine (AQ), and mefloquine (MQ). Solid QN and MQ were added to CBSO and the

solutions reached the desired concentration after 2 - 4 days. AQ and CQ were added in excess to CBSO and stored in the dark for 30 - 45 days, allowing the concentrations to approach the respective solubilities (68). All drug solutions were filtered through 0.2 μm nylon membrane filters and the concentrations were determined by UV–vis spectrometry using a Beckman DU 800 spectrophotometer and extinction coefficients and wavelengths listed in from Ketchum, et al. (68). The evolution of the hematin crystal surface was characterized by the velocity of growing steps ν and the rate of two-dimensional nucleation of new crystal layers J_{2D}. To determine ν, we monitored the displacements of 8 – 13 individual steps with a measured step height h = 1.17 ± 0.07 nm. Between 25 and 35 measurements were taken for each individual step and the average growth rates were reported. To determine J_{2D}, the appearance of new islands on the surface between successive images was monitored and the number of islands that grew was counted. This number was scaled with the imaged area and the time interval between images to yield J_{2D}. From 15 to 25 measurements were averaged for each J_{2D} determination.

The goal of the AFM investigations is to establish the molecular mechanisms of synergy or antagonism between step pinners and kink blockers in inhibiting the growth of hematin crystals. Using AFM imaging at mesoscopic scale, we demonstrate that step pinners and kink blockers cooperate in suppressing both the nucleation of new layers and the propagation of steps on hematin crystal surfaces. The nucleation of new layers at random locations on the crystal surface requires observations at the mesoscopic length scale, within the range of capabilities of standard AFM techniques. Molecular resolution images of growing steps would have provided additional insights. As shown in our

previous work on hematin crystallization, imaging with resolution comparable to the size of the hematin molecule, ca. 1 nm, is possible during in situ AFM monitoring of flat crystal planes (88). The presence of steps, however, disrupts the contact between the scanning tip and the crystal surface and lowers the image resolution. Strict numerical correspondence between discrete molecular-level events and the mesoscopic and macroscopic variables that characterize crystal growth and inhibition has been established in out earlier work (*101-104*) and has never been questioned in crystal growth research. This correspondence supports the molecular mechanisms based on observations at mesoscopic length scales.

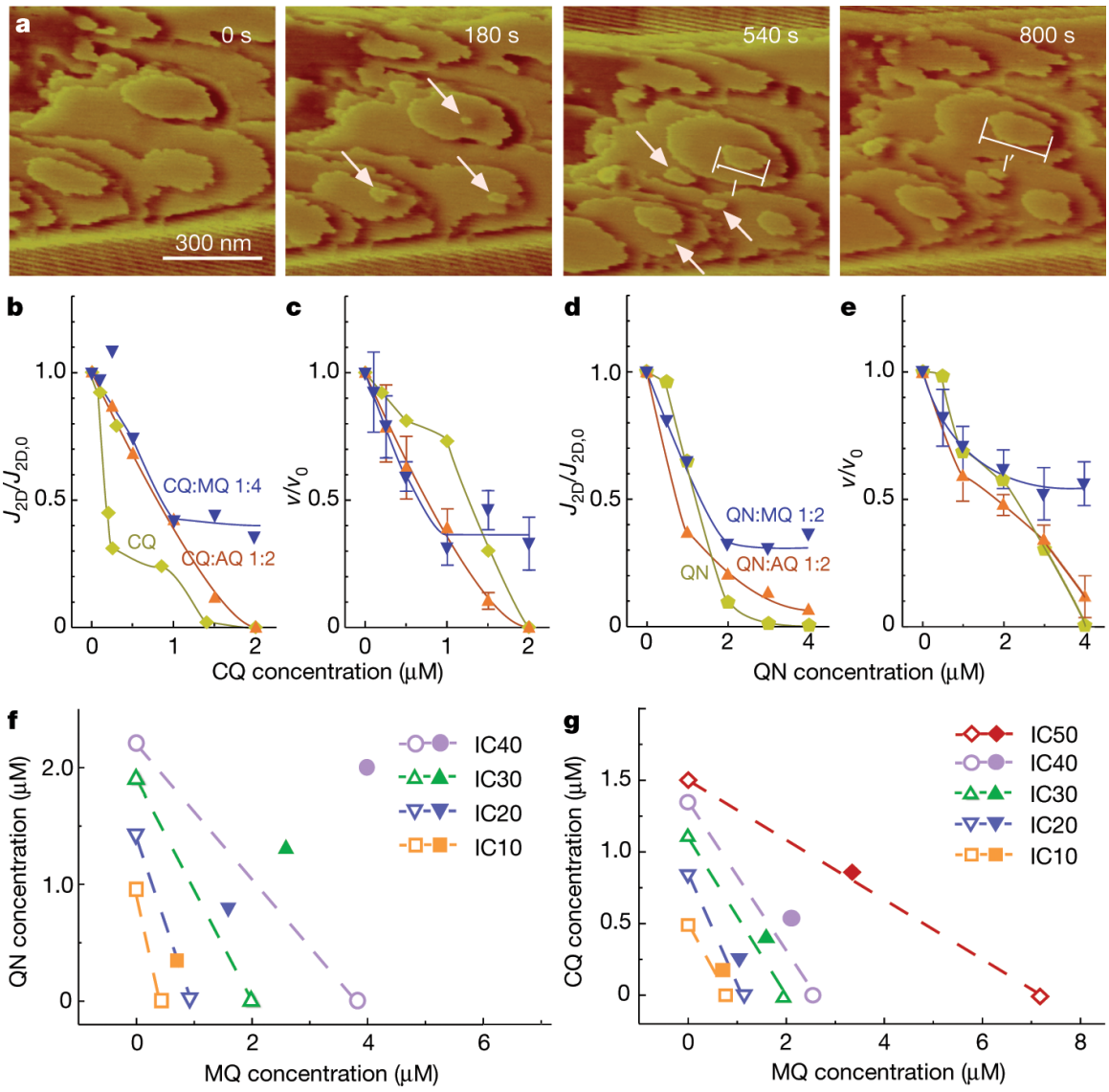

Figure 39. Cooperativity of CQ/MQ, CQ/AQ, QN/MQ, and QN/AQ inhibitor pairs in suppressing layer generation and spreading.

The lack of deactivation due to solution complexation suggests that the antagonistic cooperativity emanates from drug effects on specific surface processes. We characterize the effects of drug combinations on the molecular processes of growth of the (100) face employing *in situ* time-resolved atomic force microcopy (AFM) (*62, 88*). We scrutinize drug effects on the rate of two-dimensional nucleation of new crystal layers J_{2D} and the rate of propagation of steps v. For J_{2D}, we count the number of new layer nuclei that grow

above a critical size R_c per unit area of the surface and unit time. We determine *v* from the displacement of the steps over time(*62*). The correlation between J_{2D} and the concentration of the drugs demonstrates that the addition of the kink blockers MQ and AQ to the step pinner CQ significantly enhances the nucleation of new layers relative to that with solitary CQ, indicating strong antagonism. In suppressing *v* the cooperativity between CQ and MQ and CQ and AQ transitions from additive at low concentrations to antagonistic at concentrations above C_{QN} = 1 mM, $C_{MQ} = C_{AQ}$ = 2 μM. MQ, which in solitary does not suppress J_{2D}, exhibits additive cooperativity with QN at C_{MQ} < 4 μM and antagonism at C_{MQ} < 4 μM. Similarly, AQ, which on its own depresses J_{2D} by up to 60% (*88*), transitions from additivity at C_{AQ} < 2 μM to antagonism at C_{AQ} > 4 μM. Both MQ and AQ strongly inhibit the step velocity *v* when acting alone (*88*) and the similarity between *v*s measured in the presence of the QN/MQ and QN/AQ combination to *v*s obstructed by QN alone (Fig. 2e) signify strong antagonism between MQ and QN and AQ and QN. The cooperatively between the CQ and QN and MQ and AQ can be quantified from the isobolograms (Fig. 2 f and g), in which the doses of paired drugs needed to inhibit J_{2D} and v by a certain percentage are compared to the sum of the responses to each drug applied individually.

Additive and synergistic cooperativity in suppressing J_{2D} and *v* between a kink blocker, such as MQ and AQ, and a step pinner, CQ or QN, can be understood within the realm of common crystal growth models. The binding of MQ or AQ to kinks impedes step motion additively with the depression of the crystallization driving force of curved steps wedged between step pinners (Fig. 1 a and b). We submit that the antagonism between

the two types of inhibitors originates from the reduction of the step line tension γ, a thermodynamic prerequisite for the adsorption of kink blockers at steps (*105*). Per the Gibbs-Thomson relation, γ scales the radius of the critical two-dimensional nucleus according to $R_c = \Omega\gamma/\Delta\mu$ (*105*) (Ω is the molecular volume; $\Delta\mu = k_BT\ln(c_H/c_e)$ is the chemical potential difference between the solution and the crystal; k_B, Boltzmann constant; *T*, temperature; c_H, hematin concentration; c_e, solubility). In turn, lower γ and R_c stimulate faster layer nucleation as $J_{2D} = J_o\exp(-\pi\gamma R_c h/k_BT)$ (*h* = 1.2 nm is the step height) (*62*)and expedite step propagation in the gaps between the adsorbed step pinners (Fig. 1a). The scenarios leading to distinct cooperativities suggest that the classical synergistic and additive cooperativities dominate at low concentrations of kink blockers, whereas the proposed mechanism of antagonism is activated at high MQ and AQ concentrations. This prediction is borne by the J_{2D} and υ correlations.

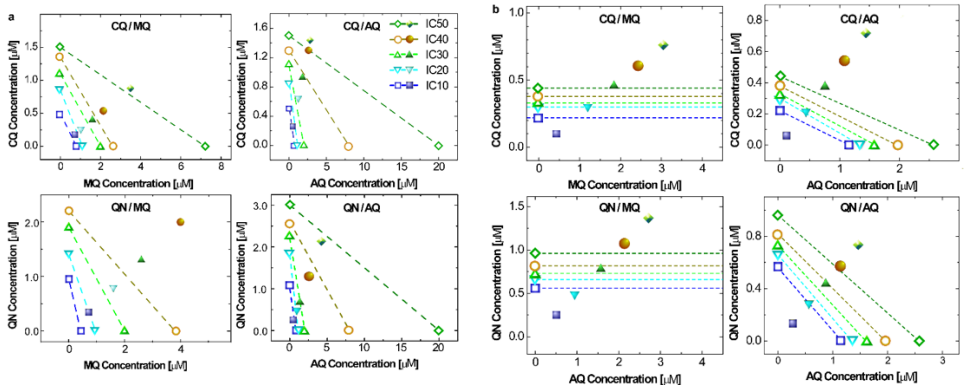

Figure 40. Isobolograms characterizing the cooperativity of the CQ/MQ, CQ/AQ, QN/MQ, and QN/AQ inhibitor pairs in suppressing.

5.5 Determining the surface tension reduction due to the presence of kink blocker

We test three elements of the proposed mechanism of antagonistic cooperativity. Data on the generation and growth of crystal layers in the presence of MQ and AQ demonstrate that: 1. γ contracts in the presence of MQ and AQ. 2. Inhibition of step motion by AQ and MQ correlates with the measured $\Delta\gamma$.

We evaluate the value of γ from the correlation between the radius of the two-dimensional nucleus of new layers R_c and the supersaturation, similarly to determinations in solutions without inhibitors carried out by Olafson and collaborators (62). The critical radius R_c for layer nucleation is defined as the threshold size above which an island has a higher probability to grow. Islands of size $R < R_{crit}$ are more likely to dissolve.

We monitored the size evolution of all newly generated islands employing time-resolved sequences of in situ AFM images and classified the islands as growing or dissolving. The largest sizes reached by dissolving islands and the threshold, above which all islands grew, were averaged to yield R_c. We determined from 25 to 30 independent R_cs at each combination of hematin and MQ or AQ concentrations. Six concentrations of hematin c_H were tested in the presence of 2.5 μM MQ and seven in the presence of 2.5 μM AQ. The R_c values obtained at each concentration of the two inhibitors were averaged and the averages were plotted as a function of the supersaturation $\Delta\mu/k_BT = \ln(c_H/c_e)$ and compared to the values of R_c in the absence of inhibitors (Fig. 3 b and c).

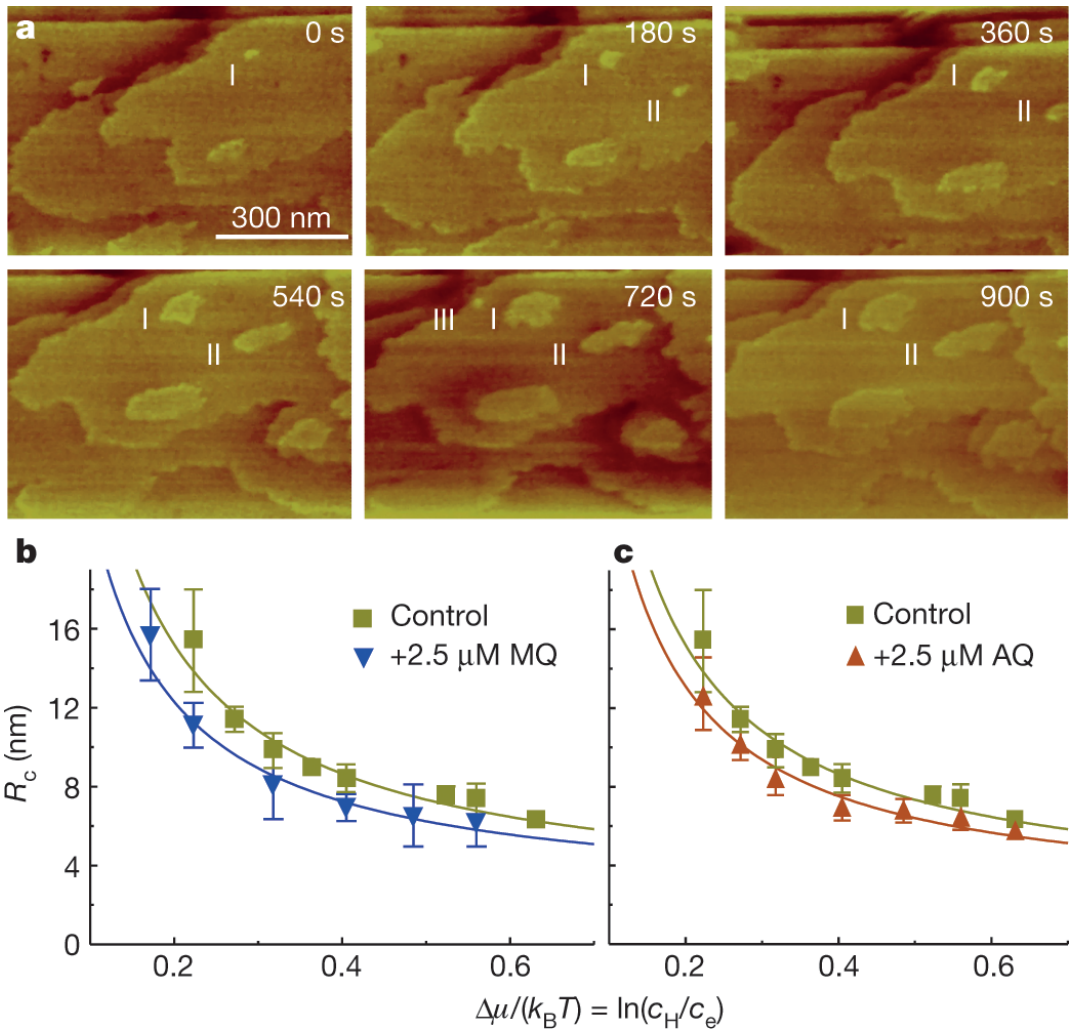

Figure 41. Characterization of the effects of the kink blockers MQ and AQ on layer nucleation.

We directly measured the R_c in the presence on 2.5 mM of MQ or AQ. R_c represents the critical size of a two-dimensional nucleus of a crystal layer below which nuclei tend to dissolve, whereas nuclei larger than R_c have a greater probability to grow (Fig. 3a). We monitored the evolution of about 70 layers nuclei at each value of $\Delta\mu$, enforced through the hematin concentration c_H (Fig. 3b). The $R_c(\Delta\mu)$ correlations (Figs. 3 c and d) are reciprocal, consistent with the Gibbs-Thomson relation, and reveal that the applications of MQ and AQ lower □ from 25 to, respectively, 20 and 22 mJ m^{-2}. These $\Delta\gamma$s invoke an

equivalent contraction of R_c and disproportionally faster v and J_{2D}. Indeed, a 20% decrease in R_c is equivalent to 1.44-fold lowering of the surface coverage □ of adsorbed step pinners. Crystal growth with effectively diminished θ may be as fast as in the presence of heavily reduced solution concentration c_D of CQ or QN, inasmuch as □ and c_D correlation conforms to the Langmuir law, $\theta = K_L c_D/(1 + K_L c_D)$ (K_L is the Langmuir constant) or a similar sublinear dependence. Since J_{2D} and v are highly sensitive functions of c_D of CQ or QN (*88*), the decrease in γ elicits strong boost in these rates.

To relate decreasing γ to the association of MQ and AQ to the kinks, we assume the two drugs adsorb to the steps following a Langmuir-type law. We evaluate $-\Delta\gamma$ using the Gibbs equation of adsorption $\Gamma = -d\gamma/d\mu$, where Γ is the amount of drug absorbed at kinks and $\mu = \mu_0 + k_B T \ln c_D$ is the drug chemical potential, and obtain $-\Delta\gamma = \int_0^{c_D} \Gamma d\mu \approx \frac{k_B T \xi n_{k,0} K_L[D]}{h}$; details of the derivation are provided in the SI. Here $\xi = (v_0 - v_\infty)/v_0$ = 0.54 for MQ and 0.4 for AQ is the maximum degree of inhibition by a kink blocker (*62*), v_0 and v_∞ are the step velocities in pure hematin solutions and at maximum inhibition, respectively, $n_{k,0} \approx 10^9$ m^{-1} is the kink density, and [D] is the concentration of free drug unattached to hematin. To assess [MQ] and [AQ] we rely on the known structures and binding constants of the HD complexes (*62*). In the SI, we model the measured correlations between v and [D] with $v = v_0\left(1 - \xi \frac{K_L \text{Error! Bookmark not defined.}}{1+K_L[D]}\right)$ and obtain K_L = 1.64 μM and 50.0 μM for MQ and AQ, respectively. These computations yield $-\Delta\gamma \approx 5$ mJ m^{-2} for both MQ and AQ (the stronger adsorption of AQ supplements its stronger complexation with hematin (*62*), leaving less

free AQ than MQ), in good agreement with the values for these two drugs assessed from the $R_C(\Delta\mu)$ correlations (Fig. 3 c and d).

The Gibbs-Thomson relation $R_c = \Omega\gamma/\Delta\mu$, where Ω = 0.708 nm^3 is the molecular volume in the crystal, prescribes the values of γ corresponding to each of the $R_c(\Delta\mu)$ correlations: 25 ± 2 mJ m^{-2} is solution without inhibitors, 20 ± 2 mJ m^{-2} in the presence of MQ, and 22 ± 1 mJ m^{-2} in the presence of AQ. The standard deviations of the three γ values arise from the regression analyses of the linear correlations $R_c(\Delta\mu^{-1})$ and reveal that the confidence intervals of γ at the three tested solution compositions partially overlap.

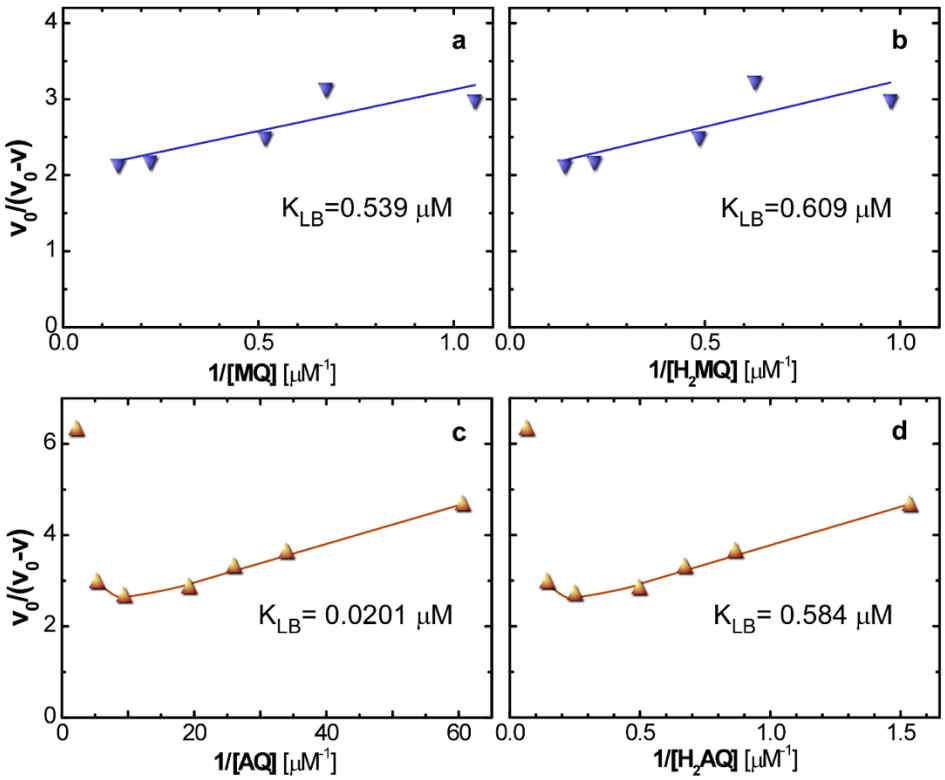

Figure 42. The correlation between the step velocity v and the inhibitor concentration in linearized coordinates $v_0'(v_0' - v)^{-1}$ and c_D^{-1}.

We analyzed the similarity between the three individual values of γ by one-way analysis of variance (ANOVA), a statistical procedure, which compares the variance between two groups to the variance within each group of data. We computed individual γ values from each R_c measurement and examined the similarity between three pairs of γ data sets: no inhibitor/AQ, no inhibitor/MQ, and MQ/AQ. The ANOVA test parameters. The three F values, corresponding to the ratio of the variances within each pair of data sets, are significantly greater than the critical values for groups consisting of 195, 177, and 297 independent measurements. The p values were of order 10-3, 10-6 and 10-7, smaller than the significance level of 0.05. These F and the p values consonantly certify that the hypothesis of equality of the three γ values is rejected.

5.5 Mathematic theories for cooperativities

The drugs MQ and AQ inhibit step motion by adsorbing to the kinks and blocking the access of the solute molecules (Fig. 1c) (*88*). We use the correlation between step velocity *v* and the concentrations of the two inhibitors, measured in our previous work (*88*), to evaluate the parameters that govern their adsorption.

5.5.1 The correlation between step velocity and kink blocker concentration.

To derive an expression for the correlation between the bulk concentration of a kink blocker c_B and *v* we rely on a fundamental tenet of crystallization that *v* is proportional to the kink density n_k (*101, 106-109*). We designate the fraction of kinks occupied by inhibitor molecules θ_B. Often, the fraction of kinks accessible to the adsorbing inhibitors is limited owing to spatial overlap between adsorbed inhibitor molecules, fast kink

dynamics, or alternative mechanisms (*88, 110*). We account for this limitation by a parameter ξ, $0 < \xi < 1$. With these assumptions

$$v \propto n_{k,B} = n_{k,0}(1 - \xi\theta_B) \text{ and } \quad v = v_0(1 - \xi\theta_B)\,, \tag{14}$$

where v_0 and $n_{k,0}$ are the values of v and n_k in the absence of inhibitors and $n_{k,B}$ is the density of kinks unoccupied by kink blocker *B* present in the bulk solution. As $\theta_B \to 1$ v asymptotically reaches its low threshold

$$v_{sat} = v_0(1 - \xi) \text{ and } v_0\xi = v_0 - v_{sat}\,. \tag{15}$$

Combining Equations (1) and (2),

$$v = v_0 - (v_0 - v_{sat})\theta_B\,. \tag{16}$$

We model θ_B with the Langmuir adsorption isotherm, which assumes finite number of equivalent adsorption sites, no interactions between adsorbed molecules, a desorption rate independent of the solution concentration of the inhibitor, and equilibrium between inhibitors on the surface and in the bulk,

$$\theta_B = \frac{K_{LB}c_B}{1+K_{LB}c_B}\,, \tag{17}$$

where K_{LB} is the Langmuir adsorption constant, and obtain

$$v = v_0\left(1 - \xi\frac{K_{LB}c_B}{1+K_{LB}c_B}\right). \tag{18}$$

Equation (5) predicts that as $c_B$increases, *v* decreases monotonically from v_0 at c_B = 0 to its saturation value v_{sat} defined in Equation (2). Our previous work revealed that the correlations of *v* to the concentrations of MQ and AQ comply with this trend (*88*).

To evaluate K_{LB} and ξ from experimentally measured $v(c_B)$ correlations, we follow a similar model for the density of growth sites on crystal surfaces in the presence of inhibitors (*110*) and linearize Eq. (5) in coordinates $v_0(v_0 - v)^{-1}$ as a function of c_B^{-1}, sometimes referred to as "Bliznakov coordinates",

$$v_0 - v = (v_0 - v_{sat})\frac{K_{LB}c_B}{1+K_{LB}c_B} \tag{19}$$

and

$$\frac{v_0}{v_0-v} = \frac{v_0}{v_0-v_{sat}} + \frac{v_0}{v_0-v_{sat}}\frac{1}{K_{LB}c_B}. \tag{20}$$

The intercept of this linear relation equals the parameter $\xi = v_0/(v_0 - v_{sat})$, according to Eq. (2). The ratio of the intercept to the slope yields the Langmuir constant K_{LB}.

In a biomimetic solution in CBSO, both MQ and AQ form complexes with hematin (*88*). The predominant complexes for both MQ and AQ consist of two hematin molecules bound to one inhibitor molecule, with binding constants 14 and 510 mM^{-2}, respectively (*88*). The complexation affects the rate of step propagation in two ways: First, it lowers the concentration of free hematin c_H and enforces a depression of the step velocity proportional to the decrease in hematin concentration (*62*). To account for the depressed crystallization driving force, we evaluate the concentration of free hematin $[H]$ and proportionally adjust the value of v_0. Second, molecular recognition between the kinks and the inhibitor would likely eliminate one of the inhibitor forms present in the bulk solution (free inhibitor and inhibitor-hematin complex) as an active inhibitor. Evidence in the literature falls short of identifying the active inhibitor. We determine the values of

K_{LB} and ξ assuming two alternative scenarios: 1. *v* is inhibited by the unliganded kink blockers and $c_B = [B]$, and 2. The active inhibitor species is the kink blocker-hematin complex and $c_B = [H_2B]$.

The values of [H], [MQ], [AQ], [H_2MQ], and [H_2AQ] at the analytical concentrations of hematin, MQ, and AQ, for which *v* was measured (*88*). The correlation between $v_0(v_0 - v)^{-1}$ versus c_B^{-1} are plotted. The values of K_{LB} and ξ emerging from the analyses based on the assumptions $c_B = [B]$ and $c_B = [H_2B]$.

5.5.2 Evaluation of the decrease of the surface free energy of the step edge $\Delta\gamma$ due to adsorption of inhibitors to the kinks.

To evaluate $\Delta\gamma$, we assume that $n_{s,B}$, the density of kinks occupied by adsorbed kink blockers, is equal to the number of blocker molecules adsorbed at the kinks. With this assumption, $n_{s,B}$ complies with the Gibbs equation of adsorption (*105*)

$$\frac{n_{s,B}}{a} = -\frac{d\gamma}{d\mu_B}, \tag{21}$$

where a is the step height and μ is the chemical potential of the inhibitors in the solution. Owing to the low inhibitor concentrations, the interactions between inhibitor molecules are weak and $\mu_B = \mu_{B0} + k_B T \ln c_B$, where μ_{B0} is the standard value of μ_B, k_B is the Boltzmann constant and *T* is temperature. The sum of occupied and free kinks $n_{s,B} + n_{k,B} = n_{k,0}$ and $n_{s,B} = \theta_B \xi n_{k,0}$.

We integrate the Gibbs equation and substitute the relations for $n_{s,B}$ and μ_B to obtain

$$-\Delta\gamma = \int_0^{c_B} \frac{n_{s,B}}{a} d\mu_B = \int_0^{c_B} \frac{\theta_B \xi n_{k,0}}{a} k_B T d \ln c_B = \int_0^{c_B} \frac{K_{LB}}{1+K_{LB}c_B} \frac{n_{k,0}\xi}{a} k_B T dc_B \quad (22)$$

and

$$-\Delta\gamma = \frac{k_B T \xi n_{k,0}}{a} \int_0^{c_B} \frac{K_{LB} dc_B}{1+K_{LB}c_B} = \frac{k_B T n_{k,0}}{a} \xi \ln(1 + K_{LB}c_B)\,. \quad (23)$$

On the (100) faces of β-hematin crystals the step height $a \cong 1.2$ nm (*62*). The characteristic molecular length is 0.73 nm in the $\vec{b}$ direction and 0.80 nm in the $\vec{c}$ direction (*84*). The kink density along the step is high (*62*) and can be approximated as the reciprocal average of these two lengths, leading to $\frac{n_{k,0}}{a} \approx 10^{18}$ m^{-2}. With this, the constant in Eq. (10) that is independent of the nature of the inhibitor is $\frac{k_B T n_{k,0}}{a} \approx 4 \times 10^{-3}$ J m^{-2}. Using the values of K_{LB} and ξ determined from the $v(c_B)$ correlations in the presence of MQ and AQ (Data Tables 4), we obtain that the dimensionless coefficients, which account for the adsorption of inhibitors at the kinks, $\xi \ln(1 + K_{LB}c_B)$, are in the range 0.55 – 0.67. The estimates for MQ and AQ and for the two alternative inhibitor species, D and H_2D, are close. Using these values, we obtain that the predicted decrease in the surface free energy of the step edge $-\Delta\gamma$ is close to 3 mJ m^{-2}, consistent with the 3 and 5 mJ m^{-2} measured for AQ and MQ, respectively.

5.5.3 The velocity of steps in the presence of both step pinners and kink blockers

We consider the motion of steps governed by three phenomena: 1. Step curvature imposed by step pinners adsorbed on the terraces; the chemical potential of curved steps is elevated (*105*), enforcing lower effective supersaturation and slower step growth. 2. Kink blockers, which bar association of solute molecules to some of the kinks, and 3.

Decrease of the surface free energy γ of the step edges that regulates how they respond to greater curvature.

We define the supersaturation as $\Delta\mu = k_B T \ln(c_H/c_e)$, where $\Delta\mu = \mu - \mu_e = \mu - \mu_c$, μ, μ_e, and μ_c being the chemical potentials of the solute in the growth solution, in the solution at equilibrium with the crystal, and in the crystal, respectively; c_H is are the solute concentration; and c_e is its solubility. This definition relies on the assumption that the ratio of solute activity coefficients in the supersaturated solution and at equilibrium is close to one. For brevity we introduce σ, defined as $\sigma \equiv \Delta\mu/k_B T = \ln(c_H/c_e)$. According to transition state theory the rate of a reversible chemical reaction is proportional to $\left(\exp\frac{\Delta\mu}{k_B T} - 1\right)$(*111*). Accounting for geometric factors and for the change in molecular density upon crystallization, the step velocity relates to the supersaturation as

$$v = \beta\Omega c_e \left(\exp\frac{\Delta\mu}{k_B T} - 1\right) = \beta\Omega(c_H - c_e), \tag{24}$$

where Ω is the molecular volume in the crystal, and β is the kinetic coefficient (*109, 112*). Linear $v(C)$ correlations have been recorded for numerous crystals growing in supersaturated solutions of solute only (*23*).

We assume the step pinners adsorb on the crystal surface with molecular surface concentration $n_P = \theta_P/S_0$, where θ_P is the surface coverage and S_0 is the area per adsorption site. For inhibitors with molecular size commensurate with that of the solute,

S_0 is the dot product of the two lattice vectors parallel to upward facing crystal face. We evaluate the average distance between stoppers as

$$L = n_P^{-0.5} = \sqrt{S_0/\theta_P}. \tag{25}$$

To evaluate θ_P, we assume that adsorption follows the Langmuir relation between θ_P and the solution concentration of the step pinners c_P,

$$\theta_P = K_{LP}c_P/(1 + K_{LP}c_P), \tag{26}$$

where K_L is the respective Langmuir constant. We assume that pinners separated by distance L enforce step curvature with radius $R = L/2$. We obtain

$$R = \frac{1}{2}\sqrt{S_0 \frac{1+K_{LP}c_P}{K_{LP}c_P}} \tag{27}$$

According to the Gibbs-Thomson relation, a step with radius of curvature R is in equilibrium with a solution of concentration c_{eR}, which is greater than the equilibrium concentration of a straight step c_e by

$$\ln\left(\frac{c_{eR}}{c_e}\right) = \frac{\Omega\gamma}{Rk_BT}, \tag{28}$$

where γ is the surface free energy of the step edge. Eq. (15) reverses the familiar application of the Gibbs-Thomson relation to define the radius R_c of a two-dimensional cluster in equilibrium with a solution with concentration c_H greater than the solubility c_e

$$R_c = \frac{\Omega\gamma}{k_BT\ln(c_H/c_e)}. \tag{29}$$

Unifying Eqs. (14) and (15), we obtain an expression for the critical supersaturation σ_d, below which a step cannot penetrate the inhibitor fence and growth ceases

$$\sigma_d = \ln\left(\frac{c_{eR}}{c_e}\right) = \frac{2\Omega\gamma}{k_B T}\sqrt{\frac{1}{S_0}\frac{K_{LP}c_P}{1+K_{LP}c_P}}. \quad (30)$$

The supersaturation range between 0 and σ_d , in which step motions and crystal growth are arrested, is often called "the dead zone". This expression for σ_d is identical to the one derived by Weaver and De Yoreo (*113, 114*).

From Eq. (15), the solution concentration at equilibrium of a curved step with radius R is

$$c_{eR} = c_e \exp\frac{\Omega\gamma}{Rk_B T}, \quad (31)$$

At a concentration $c > c_{eR}$, a step with radius of curvature R grows with velocity

$$v_R = \beta\Omega(c_H - c_{eR}) = \beta\Omega\left(c_H - c_e \exp\frac{\Omega\gamma}{Rk_B T}\right) = v_\infty \frac{c_H - c_e \exp\frac{\Omega\gamma}{Rk_B T}}{c_H - c_e}, \quad (32)$$

where v_∞ is the velocity of a straight step, defined in Eq. (11). An equivalent form of this relation, derived by Weaver, *et al.* (*113*), is

$$v_R = v_\infty\left(1 - \frac{e^{\sigma_d} - 1}{e^{\sigma} - 1}\right). \quad (33)$$

Introducing the step pinning mechanism of inhibitor action, Cabrera and Vermileya (*91*) assumed that owing to non-uniform stopper distribution the steps grow with varying velocities. Correspondingly, they evaluated the effective step velocity as the geometric mean of the maximum velocity, expressed by Eq (11) and corresponding to no stoppers (or very distant stoppers), and the minimum v, enforced by closely spaced stoppers and expressed by Eq. (19). This mode of averaging invoked an exponent of ½ on the expression in the parenthesis in Eq. (19) in the final step motion law. Recent solid-on-solid kMC results reveal that the surface distribution of step pinners has no effect on the step

velocity (*115*), i.e., uniformly distributed pinners inhibit moving steps to the same degree as randomly positioned pinners of the same surface concentration. An analytical model that views step propagation though a fence of randomly distributed stoppers as a percolation transition concurs with this conclusion (*116*). Both results suggest that averaging between inhibited and unaffected step motion is avoidable. The analysis above differs from the model of Cabrera and Vermileya (*91*) in one additional aspect. We refrain from assuming that only the linear part of the Langmuir isotherm, Eq. (13), applies, which leads to a distinct relation for σ_d.

Combining Eq. (19) with Eq. (14) on the relation between the step radius of curvature R, dictated by the surface concentration of step pinners, and the bulk concentration of step pinners c_P engenders a relation between the v and c_P

$$v_R = \frac{v_\infty}{c-c_e}\left(c_H - c_e \exp\frac{2\Omega\gamma}{k_B T}\sqrt{\frac{K_{LP}c_P}{S_0(1+K_{LP}c_P)}}\right). \quad (34)$$

According to Eq. (21), the velocity v_R of a step with curvature *R* enforced by step pinners with solution concentration c_P decreases monotonically from v_∞ at $c_P = 0$ to zero as c_P increases.

Kink blockers present in the solution at concentration c_B, which adsorb to the kinks with Langmuir constant K_{LB}, impact step motion in two ways: 1. they diminish the number of kinks available for solute association, and 2. they lower the surface free energy of the step edge. These two consequences can be quantified by Eqs. (5) and (10), respectively, leading to

$$v_R = \beta\Omega\left(1 - \xi\frac{K_{LB}c_B}{1+K_{LB}c_B}\right)\left(c_H - c_e \exp\left(\frac{2\Omega}{k_BT}\left(\gamma_0 - \frac{k_BTn_{k,0}}{a}\xi\ln(1+K_{LB}c_B)\right)\sqrt{\frac{K_{LP}c_P}{S_0(1+K_{LP}c_P)}}\right)\right), \quad (35)$$

where $v_0 = \beta\Omega(c_H - c_e)$ is the step velocity in the absence of both step pinners and kink blockers and γ_0 is the surface free energy of the step edge in the absence of kink blockers.

5.5.4 Cooperativity between step pinners and kink blockers in suppressing step motion.

According to a recently proposed rationale, the cooperativity between two inhibitors, designated 1 and 2, of any process can be classified as synergistic, additive, or antagonistic (*93*) using the value of a combination index, *CI*, defined as

$$CI = \frac{C_{1,combination}}{C_{1,alone}} + \frac{C_{2,combination}}{C_{2,alone}}, \quad (36)$$

where C_i are the concentrations (or doses, for pharmaceuticals (*83, 86*)) of the respective inhibitor applied to attain a certain degree of inhibition in combination with the other inhibitor or acting alone. If CI = 1, the cooperativity between the two inhibitors is considered additive; CI values lower than one are viewed as indications of synergistic cooperativity and *CI* > 1 designates antagonism. The definition of CI in Eq. (23) implies that only functional relations of a response V (process rate, disease spread, parasite survival, etc.) to C_1 and C_2, which contain linear combinations of these two variables, could result in additive cooperativity. Such dependencies are of the type $V(C_1, C_2) = V(A_1C_1 + A_2C_2)$ and suggest that both inhibitors employ the same mechanism of action, in which inhibition is a linear function of the inhibitor concentration. For instance, if $V(C_1, C_2)$ can be written as $V = V_0/(1 + A_1C_1 + A_2C_2)$, then 50% inhibition by each of the inhibitors acting alone, for which $V_0/(1 + A_1C_\mathrm{i}) = 0.5V_0$, is driven by $C_1 = 1/A_1$ and

$C_2 = 1/A_2$. If the two inhibitors are combined, the equality $\frac{V_0}{1+A_1C_1+A_2C_2} = 0.5\mathrm{V}_0$ is satisfied by $C_1 = 1/2A_1$ and $C_2 = 1/2A_2$. Substituting the four concentration in Eq. (23) yields *CI* = 1. This evaluation yields the same result for *CI* for any other inhibition fraction. An example of a crystal growth inhibition mechanism that complies with the requirements for additive synergy is suppression of step motion by kink blockers, discussed by Sangwal [26,27] and others [28,29]. Functional dependencies that contain the product of C_1 and C_2 can lead to both behaviors. For example, if $V(C_1, C_2) = V(C_1 + C_2 + AC_1C_2)$ then using $A_1C_{1,alone} = A_2C_{2,alone} = C_{1,combination} + C_{2,combination} + AC_{1,combination}C_{2,combination}$ gives $A_1C_{1,alone} = A_2C_{2,alone} = C_{1,combinatino} + C_{2,combination} + AC_{1,combination}C_{2,combination}$ which is always less than 1 for positive A (i.e., the cooperativity is synergistic) and greater than one for negative A (corresponding to antagonistic cooperativity).

Attempts to correlate mechanisms of action of more than one inhibitor of crystal growth to the strict definition of cooperativity in Eq. (23) have been rare and mostly focus on cooperativity between crystal growth inhibitors in bulk crystal production. These investigations concluded that the two inhibitors enhance each other's activity if they suppress adjacent crystal faces (*100, 117*).

The dependence of the step velocity on the concentrations of step pinners and kink blockers $v_R(c_P, c_B)$ in Eq. (22) suggests a definition of cooperativity based on the molecular mechanisms of action of the individual inhibitors. The cooperativity between a step pinner at concentration c_P and a kink blocker at concentration c_B would be additive

if $v_R(c_P, c_B)$ belongs to a straight line anchored at $v_R(c_P, 0)$ and $v_R(0, c_B)$. Values of $v_R(c_P, c_B)$ that are lower or greater that the value belonging to the straight line between $v_R(c_P, 0)$ and $v_R(0, c_B)$ define, respectively, synergistic or antagonistic cooperativity. Unfortunately, the dependence $v_R(c_P, c_B)$ in Eq. (22) is more complex than the three functional forms discussed above. Neither c_P nor c_B can be expressed as analytical functions of v_R at a certain fraction inhibition. Consequently, cooperativity analysis in terms of Eq. (23) of the combined action of step pinners and kink blockers on step growth can only be carried out numerically. Plots of $v_R(c_P, c_B)$ using independently determined governing parameters reveal that for low degrees of inhibition, $v_R/v_0 > 0.7$, the $v_R(c_P, c_B)$ is concave, i.e., a combination of a the two inhibitors achieves a certain degree of inhibition at concentrations c_p and c_B that are lower than those at the straight line connecting $v_R(c_P, 0)$ and $v_R(0, c_B)$, an indication of synergistic cooperativity. In contrast, for $v_R/v_0 < 0.7$ the $v_R(c_P, c_B)$ surface is convex indicating that the concentrations of the two inhibitors required to reach a certain degree of inhibition at higher than those along the line connecting the anchor points at $v_R(c_P, 0)$ and $v_R(0, c_B)$, a signature of antagonistic cooperativity. This partition between synergistic and antagonistic cooperativities conforms with data on the inhibition of hematin step velocity v by the joint action of CQ/AQ, CQ/MQ, QN/MQ, and QN/AQ in Fig. 2 c, e and the respective isobolograms.

Eq. (22) allows an alternative approach to rationalize the cooperativity between step pinners and kink blockers. We distinguish between synergistic and antagonistic

cooperativities using the signs of the derivatives $\left(\frac{\partial v_R}{\partial c_P}\right)_{c_H,c_B}$ and $\left(\frac{\partial v_R}{\partial c_B}\right)_{c_H,c_P}$. If both of derivatives are negative in a certain range of c_P and c_B, the cooperativity between step pinners and kink blockers would be synergistic. Transition from negative to positive values of one of these derivatives would mark a crossover to antagonistic cooperativity.

The derivative $\left(\frac{\partial v_R}{\partial c_P}\right)_{c_H,c_B}$ characterizes the response of the step velocity to increasing concentration of step pinners c_P at constant concentrations of solute $c_H > c_e$ and kink blockers c_B,

$$\left(\frac{\partial v_R}{\partial c_P}\right)_{c_H,c_B} = \left(\frac{\partial v_R}{\partial R}\right)_{c_H,c_B}\left(\frac{\partial R}{\partial c_P}\right)_{c_H,c_B}. \tag{37}$$

Here R is the radius of step curvature governed by the separation between step pinners adsorbed on the surface, quantified by Eq. (14), so that

$$\left(\frac{\partial R}{\partial c_P}\right)_{c_H,c_B} = -\frac{S_0}{8RK_{LP}c_P^2}.$$

From Eq. (19),

$$\left(\frac{\partial v_R}{\partial R}\right)_{c_H,c_B} = \frac{v_B}{c_H-c_e}\frac{\Omega\gamma_B}{R^2k_BT}c_e\exp\frac{\Omega\gamma_B}{Rk_BT}.$$

We obtain

$$\left(\frac{\partial v_R}{\partial c_P}\right)_{c_H,c_B} = -\frac{v_B}{c_H-c_e}\frac{S_0}{8R^3K_{LP}c_P^2}\frac{\Omega\gamma_B}{k_BT}c_e\exp\frac{\Omega\gamma_B}{Rk_BT}, \tag{38}$$

where $v_B = v_0\left(1-\xi\frac{K_{LB}c_B}{1+K_{LB}c_B}\right)$ is the step velocity in the presence of kink blockers only, Eq. (5), and $\gamma_B = \gamma_0 - \Delta\gamma = \gamma_0 - \frac{k_BTn_{k,0}}{a}\xi\ln(1+K_{LB}c_B)$, Eq. (10), is the surface free energy of the step edge reduced by the adsorption of kink blockers; both v_B and γ_B are

positive. With this, $\left(\frac{\partial v_R}{\partial c_P}\right)_{c_H,c_B}$ is always negative, i.e., the addition of step pinners lowers the step velocity at any concentration of kink blockers.

The derivative $\left(\frac{\partial v_R}{\partial c_B}\right)_{c_H,c_P}$ predicts how step motion reacts to the presence of kink blockers. Since kink blockers affect both the density of kinks available for solute incorporation and the step edge surface free energy, the expression for this derivative contains two summands,

$$\left(\frac{\partial v_R}{\partial c_B}\right)_{c_H,c_P} = \left(\frac{\partial v_R}{\partial v_B}\right)_{c_H,c_P}\left(\frac{\partial v_B}{\partial c_B}\right)_{c_H,c_P} + \left(\frac{\partial v_R}{\partial \gamma_B}\right)_{c_H,c_P}\left(\frac{\partial \gamma_B}{\partial c_B}\right)_{c_H,c_P}. \quad (39)$$

From Eqs. (19), (5) and (10),

$$\begin{aligned}
\left(\frac{\partial v_R}{\partial v_B}\right)_{c_H,c_P} &= \frac{1}{c_H - c_e}\left(c_H - c_e \exp\frac{\Omega\gamma_B}{Rk_BT}\right), \\
\left(\frac{\partial v_B}{\partial c_B}\right)_{c_H,c_P} &= -v_0 \frac{\xi K_{LB}}{(1+K_{LB}c_B)^2}, \\
\left(\frac{\partial v_R}{\partial \gamma_B}\right)_{c_H,c_P} &= -\frac{v_B}{c_H - c_e}\frac{\Omega}{Rk_BT} c_e \exp\frac{\Omega\gamma_B}{Rk_BT}, \text{ and} \\
\left(\frac{\partial \gamma_B}{\partial c_B}\right)_{c_H,c_P} &= -\frac{\xi k_B T n_{k,0}}{a}\frac{K_{LB}}{(1+K_{LB}c_B)}.
\end{aligned} \quad (40)$$

Substituting these expressions into Eq. (26),

$$\left(\frac{\partial v_R}{\partial c_B}\right)_{c_H,c_P} = -\frac{v_0}{c_H - c_e}\frac{\xi K_{LB}}{(1+K_{LB}c_B)^2}\left(c_H - c_e \exp\frac{\Omega\gamma_B}{Rk_BT}\right) + \frac{v_B}{c_H - c_e}\frac{\Omega n_{k,0}}{Ra}\frac{\xi K_{LB}}{(1+K_{LB}c_B)} c_e \exp\frac{\Omega\gamma_B}{Rk_BT}. \quad (41)$$

The first summand in this expression describes the reduction of the number of kinks available for solute incorporation and it is, accordingly, always negative. The second summand accounts for the reduction of surface free energy due to the adsorption of kink blockers to the step edge and it is positive. The difference between the magnitude of the

two summands determines the sign of $\left(\frac{\partial v_R}{\partial c_B}\right)_{c_H,c_P}$. Since $\left(\frac{\partial v_R}{\partial c_P}\right)_{c_H,c_B}$ is always negative, the sign of $\left(\frac{\partial v_R}{\partial c_B}\right)_{c_H,c_P}$ determines the type of cooperativity between step pinners and kink blockers. At low values of c_P, the enforced step curvature radius R is high and the correction to c_e, which reduces the magnitude of the first summand of Eq. (28), is small. This negative second summand dominates the expression on the left-hand side of Eq. (28) and determines the sign of $\left(\frac{\partial v_R}{\partial c_B}\right)_{c_H,c_P}$, leading to synergistic cooperativity of the kink blockers with the step pinners, as observed in Fig. 2 c and e in the same c_P range. Elevated concentrations of step pinners lead to high density of adsorbed pinners on the crystal surface and low R. The correction to c_e increases, which minimizes the driving force for step growth, $\left(c_H - c_e \exp\frac{\Omega\gamma_B}{Rk_BT}\right)$ in the first summand of Eq. (28). The dominance of the second positive summands enforces a positive sign of $\left(\frac{\partial v_R}{\partial c_B}\right)_{c_H,c_P}$, indicating that higher concentrations of step pinners lead to faster v_R. Remarkably, positive values of $\left(\frac{\partial v_R}{\partial c_B}\right)_{c_H,c_P}$ that correspond to the counterintuitive faster step growth at higher kink blocker concentrations are only possible in the presence of step pinners. If c_P = o, $\left(\frac{\partial v_R}{\partial c_B}\right)_{c_H,c_P} = \left(\frac{\partial v_B}{\partial c_B}\right)_{c_H}$ and, according to Eq. (28), is always negative.

Within this line of argument, the line defined by the relation

$$\left(\frac{\partial v_R}{\partial c_B}\right)_{c_H,c_P} = 0 \tag{42}$$

may be viewed as another approximate diagram of the areas of synergistic and antagonistic cooperativity in the (c_P, c_B) plane. Figure 42 reveals that synergistic cooperativity defined using the derivate $\left(\frac{\partial v_R}{\partial c_B}\right)_{c_H, c_P}$ is confined to low concentrations of the two inhibitors; by contrast, elevated concentrations of c_P and c_B lead to antagonistic cooperativity.

5.5.5 Cooperativity between step pinners and kink blockers in suppressing the generation of new crystal layers by 2D nucleation.

On the (100) surface of β-hematin crystals, new layers are generated by two-dimensional nucleation. The rate of generation of new layers J_{2D} is governed by the supersaturation according to the relation (*62, 118*)

$$J_{2D} = J_0 \exp -\frac{\pi \Omega \gamma^2 h}{\Delta \mu k_B T}. \quad (43)$$

In Eq. (30), J_0 account for the association of molecules to newly nucleated islands. It is often assumed that J_0 relates to the solute concentration c_H in a manner similar to that of v (*118*). Whereas this may be true for relatively large 2D nuclei that form at low supersaturations, the 2D critical radii on hematin crystal surfaces range from 8 to 16 nm (see Fig. 3). At these sizes, the curvature of the nucleated islands may enforce kink structures and densities, which diverge significantly from those on straight steps. Thus, the association of kink blockers to the edges of newly nucleated islands may deviate from the mechanism that underlies Eqs. (1) – (7) above. Even though explicit relations on the effects of kink blockers on J_0 are a challenge, it is likely that the association of kink blockers to the edges of the island nuclei will lower J_0.

Both step pinners and kink blockers may affect the ratio in the exponent in Eq. (30). Step pinners adsorbed on crystal surfaces enforce additional curvature on nucleating 2D islands. The excess curvature would effectively increase the solubility. A possible way to account for the solubility increase is through the Gibbs Thomson relation, Eq. (18), which leads to

$$\frac{\Delta\mu_R}{k_BT} = \ln\frac{c_H}{c_e} - \frac{\Omega\gamma}{Rk_BT} = \frac{\Delta\mu_0}{k_BT} - \frac{\Omega\gamma}{Rk_BT}, \tag{44}$$

where R is the average distance between adsorbed stoppers, defined by Eq. (14), and $\Delta\mu_0$ is the supersaturation. Kink blockers adsorbing on the island edge lower its free surface energy γ, as defined in Eq. (10). Quantitative predictions of the degree of inhibition induced by these mechanisms would be inaccurate owing to the poorly understood structure of the island edge.

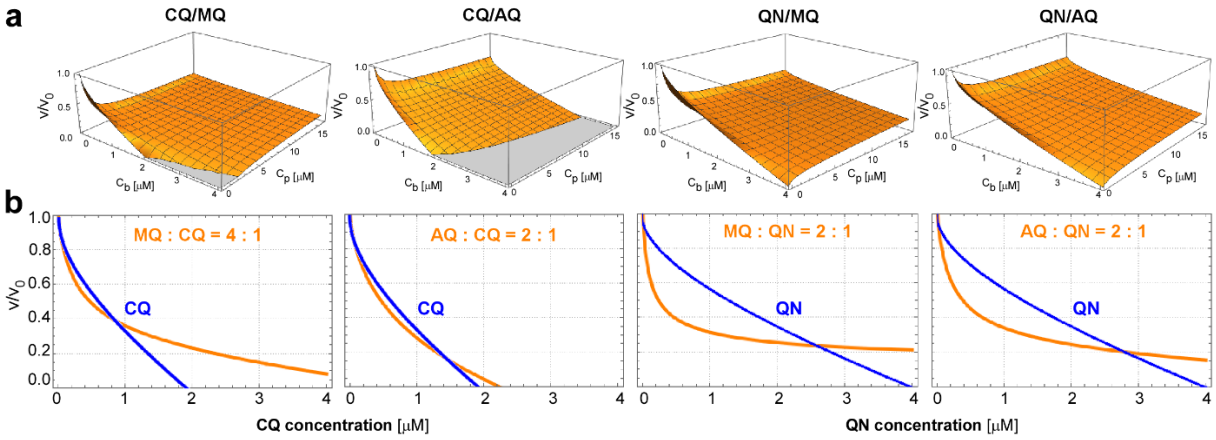

Figure 43. The step velocity v in the presence step pinners and kink blockers, relative to that in pure solutions v_0 **c**omputed.

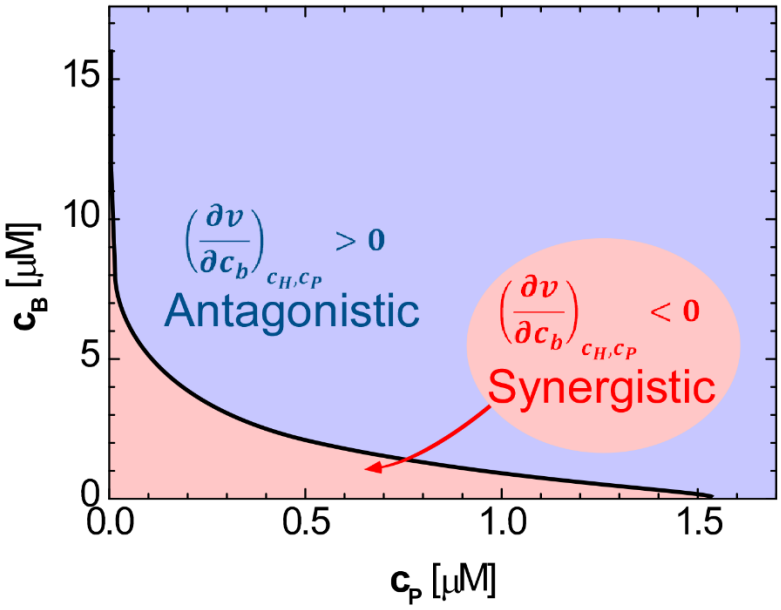

Figure 44. The pairs of concentrations of step pinners c_P and kink blockers c_B that satisfy the equality $(\partial v_R/\partial c_B)_{c_H,c_P} = 0$, where $(\partial v_R/\partial c_B)_{c_H,c_P}$.

Still, these qualitative considerations suggest that step pinners inhibit the 2D nucleation rate by cutting down the effective supersaturation that drives nucleation. Kink blockers inhibit 2D nucleation by suppressing J_0 synergistically with the step pinners, but may weaken the effect of step pinners by lowering γ. Since γ impacts more strongly the nucleation rate J_{2D} than the velocity of propagation of layers v, this effect on γ indicates that the kink blockers constrain the inhibition of J by step pinners to a greater extent than that of v. This prediction is borne for three of the four tested pairs of inhibitors (CQ/MQ, CQ/AQ, and QN/AQ) by isobolograms and the Combination Index values, which reveal stronger antagonism between the two classes of inhibitors in suppressing J_{2D} than in impeding v.

Table 1

The values of the Combination Index CI for the four listed step pinner/kink blocker pairs calculated for the inhibition of crystal length in bulk crystallization experiments, the step velocity, and the 2D nucleation rate of new crystal layers.

IC	CQ/MQ	CQ/AQ	QN/MQ	QN/AQ
		Crystal Length		
10	0.223	1.628	0.232	0.359
20	0.217	2.548	0.230	0.419
30	0.215	2.545	0.227	0.460
40	0.698	1.560	0.297	0.232
50	1.089	1.266	0.318	0.240
		Step Velocity		
10	1.260	1.263	2.200	0.875
20	1.251	1.917	2.256	1.107
30	1.164	1.783	1.984	0.968
40	1.208	1.325	1.962	0.920
50	1.039	1.099		0.975
		Nucleation Rate		
10	0.460	0.372	0.438	0.470
20	0.995	1.033	0.726	0.843
30	1.403	1.608	1.072	1.153
40	1.603	1.983	1.306	1.285
50	1.731	2.189	1.525	1.394

≤0.7	0.7 - 0.85	0.85 - 0.9	0.9 - 1.1	1.1 - 1.2	1.2 - 1.3	≥1.3
Synergism	Moderate Synergism	Slight Synergism	Nearly Additive	Slight Antagonism	Moderate Antagonism	Antagonism

Table 2

Values of the ANOVA parameters used to test the distinction between the values of the surface free energy γ in hematin solution in the absence of inhibitors and in the presence of AQ or MQ

Source of Variation	Sum of Squares	Degrees of freedom	Mean squares	F	P-value	F critical
			No inhibitor/AQ			
Between Groups	100.7	1	100.7	9.43	0.00247	3.89
Within Groups	1858.3	194	10.6			
Total	1959.1	195			Confidence interval	95%
			No inhibitor/MQ			
Between Groups	327.2	1	327.2	23.15	3.50E-06	3.90
Within Groups	2204.9	176	14.1			
Total	2532.2	177			Confidence interval	95%
			MQ/AQ			
Between Groups	306.7	1	306.7	25.3	8.33E-07	3.87
Within Groups	3581.9	296	12.1			
Total	3888.6	297			Confidence interval	95%

Table 3

Concentrations of free hematin [H], free inhibitors [D], and kink blocker-hematin complexes [H_2B], governed by inhibitor-hematin complexation, evaluated at analytical concentrations of hematin c_H and inhibitor C_B using complexation constants 14 and 510 mM^{-2} for MQ and AQ, respectively (*88*).

c_H, mM	C_B, μM	[H], mM	[B], μM	[H_2B], μM	$[B]^{-1}$, μM^{-1}	$[H_2B]^{-1}$, μM^{-1}	$v_0' v_0^{-1}$	v, nm s^{-1}	$v_0'(v_0' - v)^{-1}$
MQ									
0.28	2.0	0.278	0.948	1.025	1.054	0.976	0.983	0.654	2.990
0.28	3.0	0.277	1.486	1.594	0.673	0.627	0.973	0.673	3.239
0.28	4.0	0.276	1.936	2.063	0.516	0.485	0.966	0.579	2.500
0.28	9.0	0.271	4.501	4.619	0.222	0.216	0.923	0.500	2.182
0.28	14.0	0.266	7.106	7.034	0.140	0.142	0.883	0.470	2.1403
AQ									
0.28	0.66	0.279	0.016	0.65	60.5	1.534	0.989	0.776	4.637
0.28	1.2	0.278	0.029	1.15	34.0	0.864	0.981	0.711	3.632
0.28	1.5	0.277	0.038	1.48	26.0	0.672	0.975	0.679	3.298
0.28	2.0	0.276	0.051	2.00	19.3	0.498	0.967	0.623	2.814
0.28	4.1	0.272	0.106	4.01	9.41	0.249	0.934	0.583	2.663
0.28	7.1	0.266	0.190	6.95	5.21	0.144	0.885	0.584	2.948
0.28	15.0	0.251	0.457	14.6	2.19	0.068	0.755	0.635	6.302

Table 4

Values of the Langmuir constant for adsorption of MQ and AQ at kinks K_{LB} and the limiting fraction of occupied kinks ξ determined from the linear plots assuming that unliganded MQ and AQ are the active inhibitors.

	Assuming unliganded MQ and AQ are the active inhibitors		Assuming the complexes H_2MQ and H_2AQ are the active inhibitors	
	MQ	**AQ**	**MQ**	**AQ**
K_{LB}, μM^{-1}	1.9	50	1.64	1.74
ξ	0.54	0.4	0.54	0.4
$[B]$ or $[H_2B]$ at c_B = 2.5 μM	1.2	0.06	1.3	2.45
$\xi K_{LB}[B]$	1.22	1.09	1.15	1.7
$\xi \ln(1 + K_{LB}[B])$	0.64	0.55	0.62	0.67

Kinetic Monte Carlo (kMC) simulations of step motion in the presence of kink blockers and step pinners illustrate that 3. Kink blockers associated to steps passing between step pinners drive faster motion of curved steps.

5.6 Kinetic Monte Carlo model of cooperativity between step pinners and kink blockers.

We employ a standard solid-on-solid kinetic Monte Carlo (kMC) model of crystal growth. We use a surface of a Kossel crystal consisting of N_x = 50 by N_y = 100 sites occupied by N = 5000 surface molecules. In the kMC algorithm, a surface site is chosen at random and one of the possible kMC actions is performed based on the probability of the various actions; N repetitions of this act comprise one kMC time step. In the absence of inhibitors, three actions are possible at a surface site: a molecule attaches to the site, the molecular occupying the site detaches, or nothing happens (i.e. the molecule remains fixed). The probability for attachment is $dt \times \nu e^{\mu/k_B T}$, where dt is the kMC time step, ν is the inverse kMC time scale, μ is the chemical potential, T is the temperature, and k_B is Boltzmann's constant. The probability for a molecule to detach from site i is $dt \times \nu e^{E_i/k_B T}$, where E_i is the energy of the surface molecule at site i. The energy E_i is evaluated as the sum of the bond energies of the molecule with its six nearest neighbors. In a pure crystal, the bond energy is taken to be the same in all directions and is denoted ε. By expressing temperatures in the dimensionless form $k_B T/\varepsilon$ the physical value of ε is not needed. Given that a molecule in the bulk crystal has six bonds with the energy shared between it and its neighbors, the binding energy in the bulk is 3ε per molecule and so the equilibrium chemical potential is μ_{equil} = 3ε.

Inhibitors are handled in two district ways. Static inhibitors function as step pinners. They are deposited on the surface at the beginning of a simulation and do not participate in the kMC actions. When a crystal molecule is next to a static pinner, the bond energy between the two is taken to be zero. Thus, the only parameter needed to characterize the pinners is their surface density. Because they do not contribute to the binding of molecules to the crystal, the pinners disrupt and impede the growth of surface layers. For conceptual simplicity, we arrange the pinners in a square grid (Figure 4c). If the pinners are too close together (i.e. if their surface density is too high), the step velocity is zero and crystal growth is arrested. The physics of step blocking by such inhibitors, the criterion for step pinning, and a demonstration that inhibition is independent of the physical arrangement of the step blockers has been extensively discussed in Lustsko, *et al*. (*115*).

A new feature of the present simulation work is the model of kink blockers. Similar to the solute molecules, the kink blockers are dynamic. In the presence of kink blockers, the pool of possible events at a crystal site is expanded to include their attachment and detachment. To block the kinks, the kink blockers must differ from the solute species and from the step pinners. We assume, for simplicity, that kink blockers do not bind to step pinners. We also assume that the kink blockers bind to the molecules in the crystal with a non-zero binding energy, otherwise, they would not exhibit a preference for kink sites. The kink blocker can only impede step growth if the bonding is weaker than the intermolecular bonds in the crystal □. On the other hand, weakly bound inhibitors would have a low residence time at the kinks and have little or no effect on step growth (*115*). To reconcile these two requirements, we assume that the kink blockers bind anisotropic

ally. We assume that the only non-zero bonds formed by kink blockers are to in-plane crystal molecules. Furthermore, we assume that the in-plane bond strengths are not equal. Two out of the four in-plane bonding directions are randomly assigned bond strength 2ε and the other two, 0.5ε. The bond energy of a solute molecule deposited on top of a kink-blocker is ε.

The total energy of a kink blocker surrounded by crystal molecules is 6ε, equal to the crystal molecules so that the incorporation of kink blockers does not change the energetics of crystal growth. On the other hand, the asymmetry of their binding to the crystal surface modifies the kinetics of step growth. A kink blocker attached to a kink site with orientation that promotes two bonds of total energy 4ε will be bound stronger than a solute molecule bound with energy 3ε. Such kink blockers are unlikely to detach. On the other hand, the bonds that this kink blocker molecule can form with the incoming solute molecules are weak and solute molecules that deposit next to it are more likely to detach than if deposited in a free kink. These dynamics impede step growth. A kink blocker attached to a kink in an unfavorable orientation, or adsorbed at a non-kink surface site, would have a total energy of 2.5ε or less and will tend to detach.

Our kMC model is subject to several constraints. First, the only model parameters that one can easily vary are the bond strengths in the various directions. Second, a foreign molecule acts as a kink blocker if (a) it is attracted to kink sites; (b) it inhibits step growth; and, (c) it has a long-enough residency time to affect the step growth dynamics. These requirements inevitably lead to asymmetric lateral bonds with a total binding energy in a

kink site equal to or more than the energy of a crystal molecule in a kink site. Within these constraints, we do not expect our results to depend much on the numerical values chosen.

Errors were estimated by averaging the step velocity over windows of 1,000 surface updates thus producing a set of independent estimates of the velocity during the simulations. The arithmetic average of these values gives the overall estimate of the step velocity and the root-mean-squared deviation from the average is used to estimate its standard deviation. The error-bars reported in the figures are the standard errors of the step velocities calculated as their standard deviations divided by the square root of the number of samples.

We examined by kinetic Monte Carlo simulations the generality of the proposed model of antagonistic cooperativity between two classes of crystallization inhibitors. We developed a Solid-On-Solid model for step growth (*115*), in which molecules associate and dissociate from steps; for simplicity, we ignore surface diffusion on the terraces. The rate of solute association depends on the supersaturation, whereas the probability of detachment is dictated by bonds a molecule forms with its neighbors. We assume that kink blockers associate and detach analogously to solute molecules and the relevant dynamics are governed by their concentration and the number and strength of bonds at an adsorption site. These assumptions lead to preferential binding to the kinks on steps (Fig. 4a) and constrained v (Fig. 4b). We assume that step pinners bind strongly to the crystal surface but that have no interactions parallel to that plane. The surface is decorated with a square array of step pinners and they remain static throughout the

simulation (Fig. 4c); assuming random step pinner surface distribution has no effect on the step velocity (*115*). Remarkably, the computed correlations between *v* and inhibitor concentrations are akin to those observed experimentally for both the kink blockers MQ and AQ, for which *v* levels off at ca. 50% inhibition, and the step pinners CQ and QN, which induce complete growth arrest at moderate drug concentrations (*88*).

Combining step pinners at a concentration above the threshold for complete growth arrest (Fig. 4e) with kink blockers un-pins the steps and resets their growth. The simulations reveal that at the microscopic level, the antagonistic cooperativity is due to the stabilization of step edge fluctuations by associating kink blockers. Steps infiltrate the pinner palisade by fluctuations that penetrate and join up behind the pinners (*115*). Closely spaced pinners suppress the extent and lifetime of the fluctuations and restrain step growth. The blockers bind to the kink-rich fingers embodying the fluctuations and increase their lifetime. At the macroscopic level, the stabilized fluctuations manifest as a decrease in γ. The attenuated γ enforces shorter R_c, which, in turn, allows step progress between the pinners.

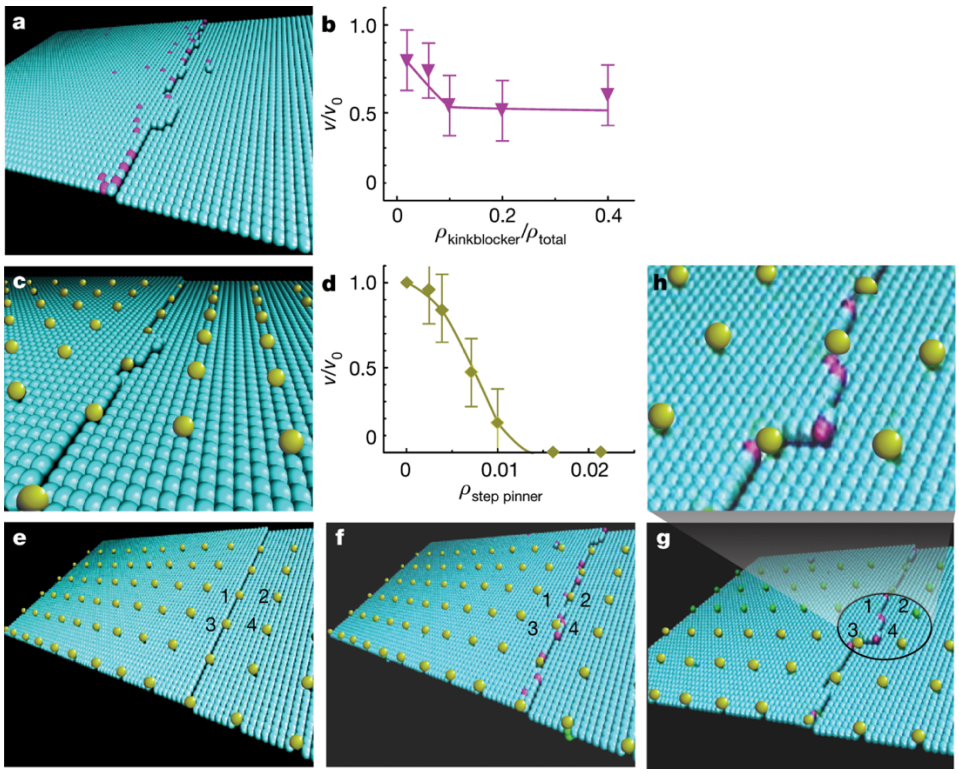

Figure 45. Solid-on-solid kinetic Monte Carlo (kMC) modelling of the action of kink blockers and step pinners on step propagation.

In summary, we put forth a mechanism of antagonistic cooperativity between crystallization inhibitors by which kink blockers attenuate the step line tension and facilitate step propagation through the palisade of step pinners. This mechanism provides guidance in the search for suitable members of antimalarial drug combination. The insights on the interactions between modifiers mediated by structures on growing crystal surfaces further the understanding and control of ubiquitous processes in nature and industry, which exploit crystallization from multicomponent environments.

Chapter 6 The roles of artemisinin class antimalarials

The increased number of malaria deaths last century attributed to quinoline resistance(*119*) has been reversed by implementation of effective artemisinin combination therapies(*120*). Artemisinin-class drugs are activated by reduced haeme, released after haemoglobin endocytosis and catabolism. Resulting cleavage of the endoperoxide bridge generates a free radical that damages bystander proteins and lipids in human patients(*121, 122*), with a concomitant 10,000-fold reduction in parasite density(*123*). Recently, a delayed clearance phenotype(*124*) deemed resistance to artemisinins has emerged in Southeast Asia, and has been linked, via an altered Kelch13 gene(*125*), to decreased haemoglobin supply at the ring stage of the parasite life cycle, leading to a marked tolerance of ring stage parasites to artemisinins(*126, 127*). Parasites in the subsequent trophozoite stage are susceptible to activated artemisinins(*128, 129*), yet the mechanism of retained trophozoite sensitivity has been elusive. Here we show that adduct metabolites formed between artemisinins and haeme, previously thought to be a benign biomarker of activated drugs, potently kill the parasites when exogenously added to Plasmodium falciparum cultures at low nanomolar concentrations. We show that haeme-drug adducts bound to haemozoin crystals are recovered from treated parasites, while time-resolved atomic force microscopy of growing β–haematin crystals confirms that bound haeme-drug adducts inhibit crystal surface growth. Moreover, we demonstrate the haeme-drug adduct operates by a unique mechanism of irreversible inhibition of β-haematin crystal surface growth in contrast to the reversible processes reported for quinolines(*88, 130*) and most common

crystal growth inhibitors. Our findings highlight a dual mechanism of the artemisinin-class drugs, which complements suicide activation and radical damage, and defeats malaria trophozoite resistance.

7.1 Mechanism of artemisinin and artesunate

In previous studies, we noticed that artemisinin and artesunate won't inhibit hematin crystallization though they are the most commonly used drugs in the combination therapy. Questions remains for the mechanism how ARTs exert to affect the malaria parasites.

Several general beliefs were proposal and explored for further understanding and drugs from artemisinin class. More debates happen in the artemisinin case as a process of activation is required for artemisinin to be functional in inhibiting crystallization. The formation of heme – artemisinin adducts have been showed in many vitro and vivo studies. Some studies concur that the activity of ART may be results from the reaction after the scission of peroxide bridge by heme in the acid digestion vacuole. On the hands, ART might be a target for intracellular ion-Sulphur containing enzymes.

From the biochemical standpoint, a protein, Plasmodium falciparum phosphatidylinositol-3-kinase (PfPI3K), was proposed to be the potential primary marker. PfPI3K is a protein known for regulating the levels of the kinase, as well as its lipid product phosphatidylinositol-3-phosphate (PI3P) and studies showed the level of Pi3P gives the predictive of the artemisinin resistance. Besides, The Evidence have showed that the C580Y, a strain is resistance to artemisinin therapies, contained larger amount of mutated PfPI3K, that limited proteolysis of PfPI3K and thus increased levels

of the kinase. Considered all the factors, PfPI3K could be a key for controlling artemisinin resistance as the specific region for the mutation of genes is proposed.

From the physiological point. In the lifecycle of the malaria parasite, they decompose the protein hemoglobin for energy and source while producing hematin as a byproduct at the intraerythrocytic stage (but Pro. Sullivan mentioned the microcrystal in the ring stage). As hematin is toxic to cells, parasites begin to transform free hematin in the solution to hematin crystals at the parasite lipid layer to reduce the level of hematin. A general understanding (no argument for CQ) appeals that antimalarial drugs are functional for stopping the crystallization process and the accumulation of hematin will eventually kill the parasite.

6.1 The activation of artemisinin and artesunate

Here we design an *in vitro* protocol to synthesize the haeme-drug adducts of artemisinin-class drugs and test their activity in suppressing *P. falciparum* and the associated molecular mechanisms. We place artemisinin or artesunate in contact with haeme(III) and a reducing agent (dithionite) in a biphasic butanol-water solvent. The resulting reactions and purification by chromatography lead to the haeme-drug adduct in ~50% yield.

Haeme solutions were prepared by a modified method using the same procedure as CBSO, but substituting n-octanol with n-butanol. Sodium dithionite and artemisinin (ART) were dissolved in DI water and n-butanol, respectively. The haeme solution was filtered with a 0.2 μm nylon membrane filter and placed in contact with the dithionite solution in a glass vial to yield a net molar ratio of 1:2:5 haeme: ART:

sodium dithionite. The vial was sealed under flow of nitrogen gas to create an inert atmosphere. The reaction involved the reduction of haeme(III) to haeme(II) with dithionite acting as the reducing agent. The system was maintained at 50 °C using a water bath (Super-Nuova™ Multi-Position Digital Stirring Hotplates). The aqueous and organic phases were rigorously mixed by shaking for ca. 30 seconds until the color of the solution changed from dark green to pink, indicating the reduction of haeme. The mixture was allowed to sit under static conditions for at least 20 minutes to allow for the separation of organic and aqueous phases, after which the artemisinin solution was injected into the organic (top) fraction. The reaction between haeme(II) and artemisinin happened immediately after the injection, as surmised by the instantaneous change in color from pink to orange. After allowing ca. 30 minutes for the reaction to reach completion, the organic layer was collected for later purification of the product, haeme – artemisinin adduct (or H-ART).

The procedure for synthesizing haeme – artesunate adduct (H-ARS) was identical to that of H-ART with the replacement of ART with artesunate (ARS). The same reaction procedure was used with the only noticeable difference being a faster reaction to generate H-ARS (or haeme – artesunate adduct), as gleaned by a more rapid color change following the addition of ARS to the haeme(II) solution. A detailed reaction mechanism of heame – drug adduct generation.

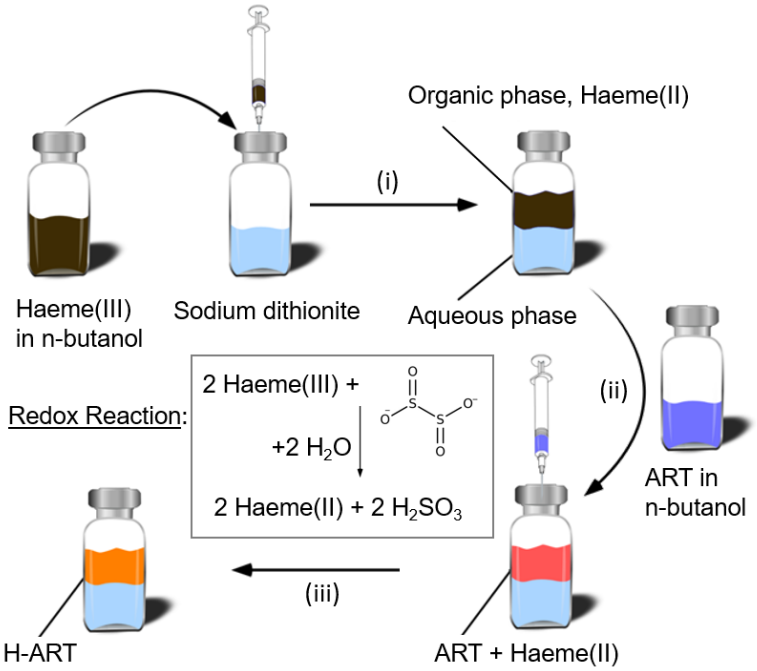

Figure 46. Steps involved in the synthesis of haeme-drug adducts.

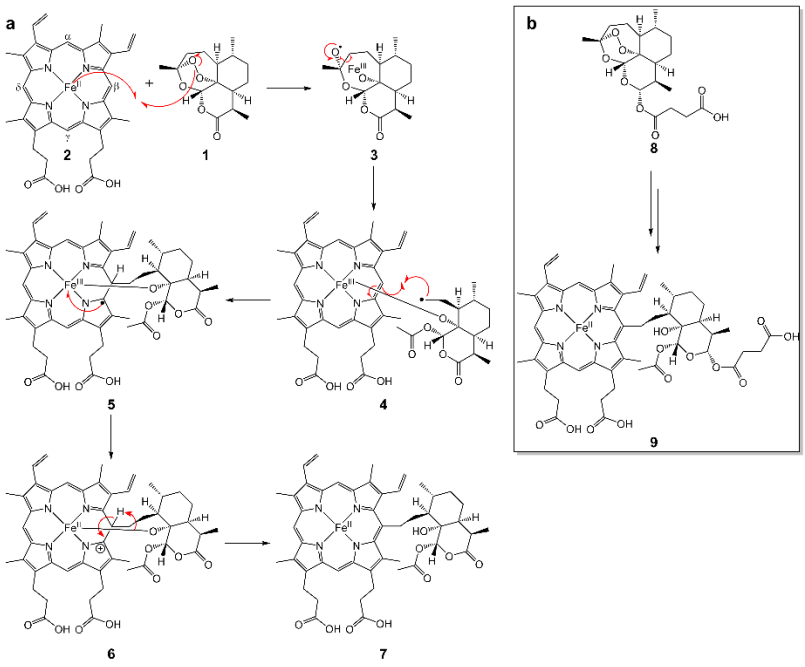

Figure 47. Reaction pathway for the synthesis of haeme – drug adduct.

The mass-to-charge (m/z) ratio of haeme and haeme – drug adducts were determined using a Bruker MicroToF ESI LC-MS at Rice University. Electrospray ionization was used with the offset voltage of 4000 V and a mobile phase of 50/50 water/acetonitrile to transfer haeme (dissolved in n-butanol), H-ART (dissolved in n-butanol or methanol/acetonitrile/water), and H-ARS (dissolved in n-butanol or methanol/acetonitrile/water) into the electron spray ionization (ESI) source. Mass spectrometry (MS) identified the characteristic mass-to-charge (*m*/*z*) ratios of H-ART as 838 and 898 (Fig. 1f) and of H-ARS as 1000.1 (Fig. 1g); the *m*/*z* values for H-ART (Fig. 1g) are similar to those of H-ART extracted from the spleens of malaria-infected mice treated with ART (*130*). MS spectra also revealed the absence of residual ART (*m*/*z* = 282.3, inset of Fig. 1f) and ARS (*m*/*z* = 383.4, inset of Fig. 1g). These analyses confirm the synthesis of adducts H-ART and H-ARS, which both lack functional endoperoxides.

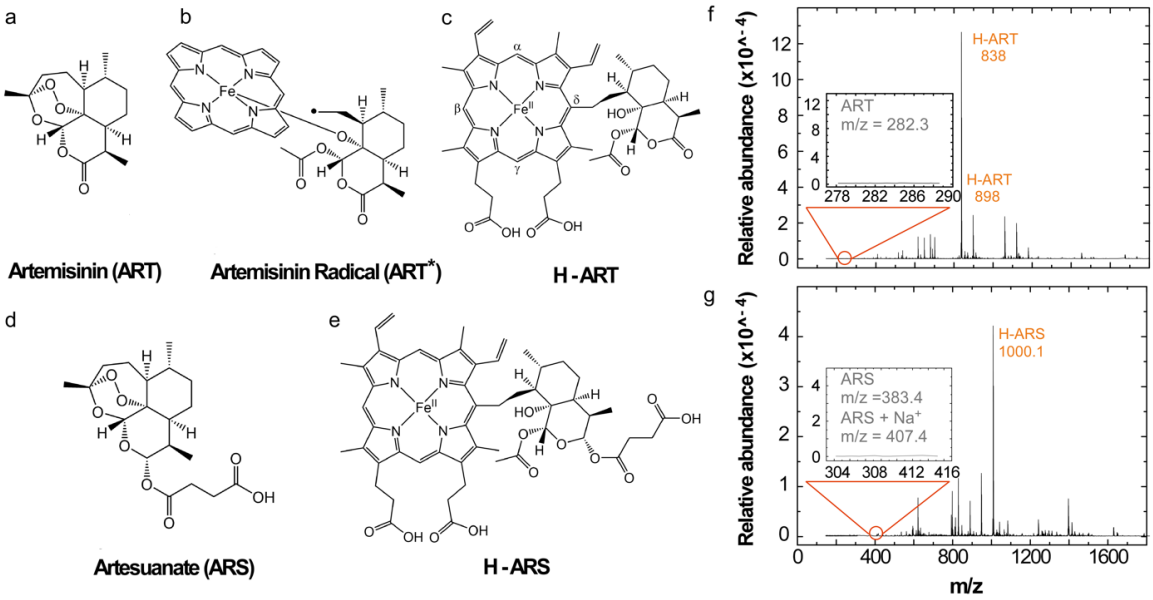

Figure 48. In vitro activation of artemisinins to haeme-drug adducts.

The collected organic fraction from the biphasic reaction was first passed through a 0.2 μm filter before injecting the solution into a high pressure liquid chromatography (HPLC) system (LC-20AD prominence liquid chromatograph, Shimadzu Corporation) equipped with a C18 column (Luna C18(2) 5um 250x4.6mm^2, Phenomenex) and two UV-Vis detectors with absorption wavelengths set at 215 nm to detect unreacted parent drug (ART and ARS) and 470 nm to detect the haeme – drug adducts (H-ART and H-ARS) as well as unreacted haeme(III). For the separation, we modified a common mobile phase reported in literature[131] using a composition of 5% methanol, 45 % acetonitrile, and a 50% mixture of formic acid (0.1%) in DI water (note that percentages are based on mass). Unreacted haeme(III) elutes at a retention time of t = 23.5 minutes), whereas both adducts (H-ART and H-ARS) elute at a nearly equivalent retention time of t $\approx$ 5.8 minutes.

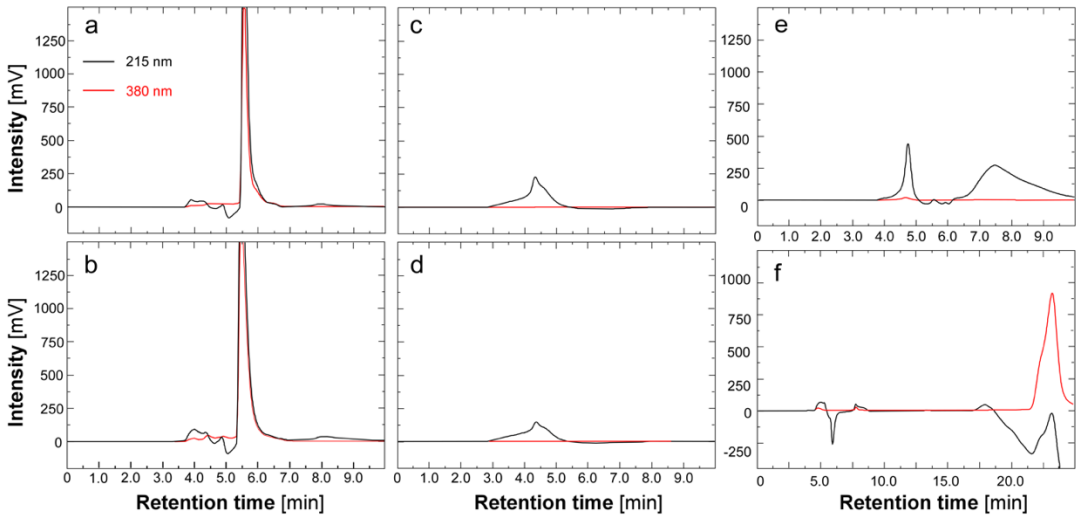

Figure 49. High-performance liquid chromatography separation.

The signature endoperoxide group of artemisinin-class drugs, such as artemisinin and artesunate is activated by reduced haeme iron(II) to generate a carbon-centered

radical, which can alkylate and damage nearby Plasmodium proteins and lipids(*121*). This suicide activation imparts a rapid lifesaving 10,000-fold drop in parasite density over the first 48 hours(*123*). The radicals terminate by alkylating haeme to generate respective haeme(III)-drug adducts, which have been thought only as correlative biomarkers of the activity of artemisinin-class drugs(*132, 133*). Parasites treated with radiolabeled [14C] ART accumulate H-ART, retaining 75% of the applied drug in close association with haemozoin(*134*). Similarly, haeme-artemisinin adducts were found in the spleens and urine of artemisinin-treated Plasmodium infected mice(*135*). Analyses of haemozoin crystals extracted from parasite culture kept under oxidizing conditions favoring haeme(III) have established that the endoperoxide bridge of artemisinins remains intact, and the inactive drug does not inhibit crystallization(*136*); however, reducing conditions favoring haeme(II) leads to the generation of haeme-drug adduct, which has been proposed to function as a haemozoin growth suppressor(*137, 138*). Haeme-artemisinin adducts were detected in P. falciparum cultures at ring, trophozoite, and schizont stages; notably, the Kelch13 mutants, associated with the delayed clearance phenotype, displayed lower adduct concentrations(*139*). In all of these findings, the exact role of the haeme-artemisinin adducts and their mechanism of action remained elusive.

6.2 Biological assays of H – ART and H – ARS against malaria

We added known quantities of haeme-drug adducts to parasite cultures of three P. falciparum strains: chloroquine (CQ) and artemisinin sensitive NF54, CQ-resistant and artemisinin sensitive CamWT, and CQ and artemisinin resistant C580Y. Traditional 72-

hour continuous half maximal inhibitory concentration (IC50) assays (*140*) were performed using radiolabeled hypoxanthine [3H] incorporation to assess the impact of adducts and their corresponding parent drugs on parasite growth (Fig. 47a,b). The IC50 values were below 10 nM for both H-ARS and H-ART (Fig. 47c), similar to the IC50 of ART and ARS alone. The low nanomolar IC50 values for H-ARS and H-ART suggest an independent mechanism of action from the radical damage caused by the parent drug. In order to assess ring stage survival of the three P. falciparum strains treated with parent drugs and corresponding haeme-drug adducts, we pulsed 500 nM of H-ARS or H-ART for 6 hours at ring and trophozoite stages in parallel with the same concentration of parent drug (ARS or ART) and CQ, which was used as a reference. Interestingly, the C580Y isolate had a survival rate of 21% when exposed to H-ARS compared to 42% for the parent drug (Fig. 47d), whereas values for H-ART, ART, and CQ were similar within experimental error. H-ART and ART result in approximately 17% survival in NF54 and CamWT, which both lack the mutant Kelch 13 gene of C580Y. A short pulse of CQ was effective against chloroquine-sensitive NF54, but more than 60% of parasites survived in the CQ-resistant CamWT and C580Y isolates. A 6-hour pulse at the trophozoite stage killed 95% of all three isolates for all five drugs.

6 hour drug pulse on rings and trophs of NF54, C580Y and CamWT. Parasite cultures will be synchronized to the ring stage 48 hours before pulse and immediately before the pulse. The troph pulse will be performed 24 hours after the ring pulse and will use the same drug concentrations as the ring pulse. Drug will then be washed off of parasites and parasites will be resuspended in fresh media with [3H] hypoxanthine to

mark growth. Parasites will then be frozen and processed after an additional 66 hours of incubation (72 hour total assay time).

Each drug will be pulsed at 3 concentrations: one below the IC_{50} (~1/3X), one slightly above the IC_{50} (~2X), and one well above the IC_{50} (5X) for 6 hours. The table below shows the three drug pulse concentrations I have selected for pyronaridine, chloroquine, and amodiaquine based off of their respective IC_{50}s. I'm deciding to go for a concentration slightly above the IC_{50} (not right at the IC_{50}) because the culture will likely survive better in this pulse environment where the drug is on for a shorter amount of time compared to the 72 h.

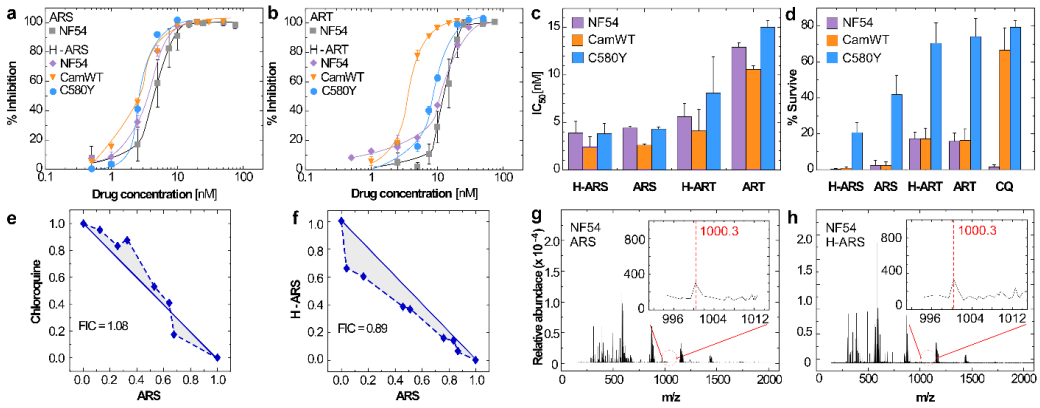

Figure 50. P. falciparum inhibition by haeme-drug adducts.

Antimalarials are often administered as combination therapies to achieve synergism; however, recent findings have provided examples where certain combinations of drugs can give rise to antagonistic cooperativity (*141*). Construction of isolobolograms help distinguish the cooperativity of drug combinations, which were used here to test binary mixtures of ARS with CQ (Fig. 47e) and H-ARS (Fig. 47f). *P. falciparum* culture with the former results in no observable changes off the line of addition, indicating additivity.

The combination of ARS and H-ARS, however, shows a change from strict additivity to mild synergistic cooperativity. This finding indicates that activation of ARS to H-ARS leads to enhanced efficacy, which is consistent with IC_{50} assays (Fig. 47c). We tested whether haeme-drug adducts directly associate with haemozoin crystals in *P. falciparum* culture. We pulsed NF54 at the trophozoite stage for 6 hours with 500 nM ARS (Fig. 47g) and H-ARS (Fig. 47h) in comparison to a control (i.e. no drug). Haemozoin was extracted from the parasite to assess residual compounds adsorbed on crystal surfaces. Analysis by MS revealed no remnants of the parent drug (ARS), whereas spectra of extracts from isolates exposed to parent drugs or haeme-drug adducts contained peaks corresponding to either H-ARS (insets of Fig. 47g and h) or H-ART. These findings provide further evidence of haeme-drug adduct formation *in vivo*, and their association with haemozoin crystals.

6.3 Monitor hematin crystallization in the presence of H – ART and H – ARS

Time resolved in situ atomic force microscopy was applied to monitor the growth of β–hematin crystal surfaces. The growth of surfaces suggested that H-ART modified the growth of β-hematin crystal by reducing the density of available kink sites where hematin molecules incorporate into the crystals that showed similarity to the mechanism applied for some of the quinoline class drugs.

Molecular confirmation of drug-crystal association and its impact on crystal growth inhibition was obtained using time-resolved *in situ* atomic force microscopy (AFM) to monitor □-haematin surface growth in a biomimetic solution containing supersaturated haeme (*62*) in the presence or absence of antimalarial drugs. Focusing on the basal (100) face(*62*), we observe the presence of unfinished layers with heights *h* =

1.17 ± 0.07 nm (Fig. 3a), close to the relevant unit cell dimension (a = 1.22 nm) (*84*). The dynamics of surface growth captured by AFM reveals a classical layer-by-layer mechanism wherein islands nucleate and grow by the attachment of solute molecules to steps(*62*). Analysis of *in situ* AFM images permits the determination of two variables used to assess the efficacy of antimalarials: the rate of layer nucleation J_{2D} as the number of islands that nucleate per unit area per time, and the velocity v of advancing steps (*88*). We recently examined the impact of quinoline-class antimalarials on β-haematin surface growth and observed distinct modes of drug-crystal binding(*62*). One of the most prominent mechanisms of crystal growth inhibition is step pinning, which occurs when drugs bind to terrace sites on the crystal surface and impose a curvature (i.e. surface tension) on advancing steps that can lead to growth succession at appreciable drug concentration. A second mode of growth inhibition is kink blocking,(*142, 143*) which occurs when drug molecules bind to the most favorable sites on the crystal surfaces for solute incorporation (kink sites) and markedly slow, but not fully suppress, the rate of growth.

AFM images extracted from growth assays in the presence of H-ART and H-ARS reveal virtually no change in the rate of layer nucleation with increasing drug concentration when scaled by the value in the absence of drug, $J_{2D,o}$. In contrast, there is a noticeable reduction in step velocity in the presence of drugs relative to the control (i.e. step velocity in the absence of drugs, v_o. Interestingly, the pristine (or inactivated) forms of artemisinins, ART and ARS, have no observable effect on β-haematin surface growth(*35, 121, 144, 145*), whereas their activated forms (H-ART and H-ARS) are effective growth

modifiers that reduce step velocity by nearly 60%. The step velocity versus drug concentration profiles for both haeme-drug adducts are signatures of a kink blocking mechanism, which was verified by replotting the data in the well-known Bliznakov coordinates (*88*) where the linearized data confirms that adducts preferentially bind to kink sites on β-haematin surfaces.

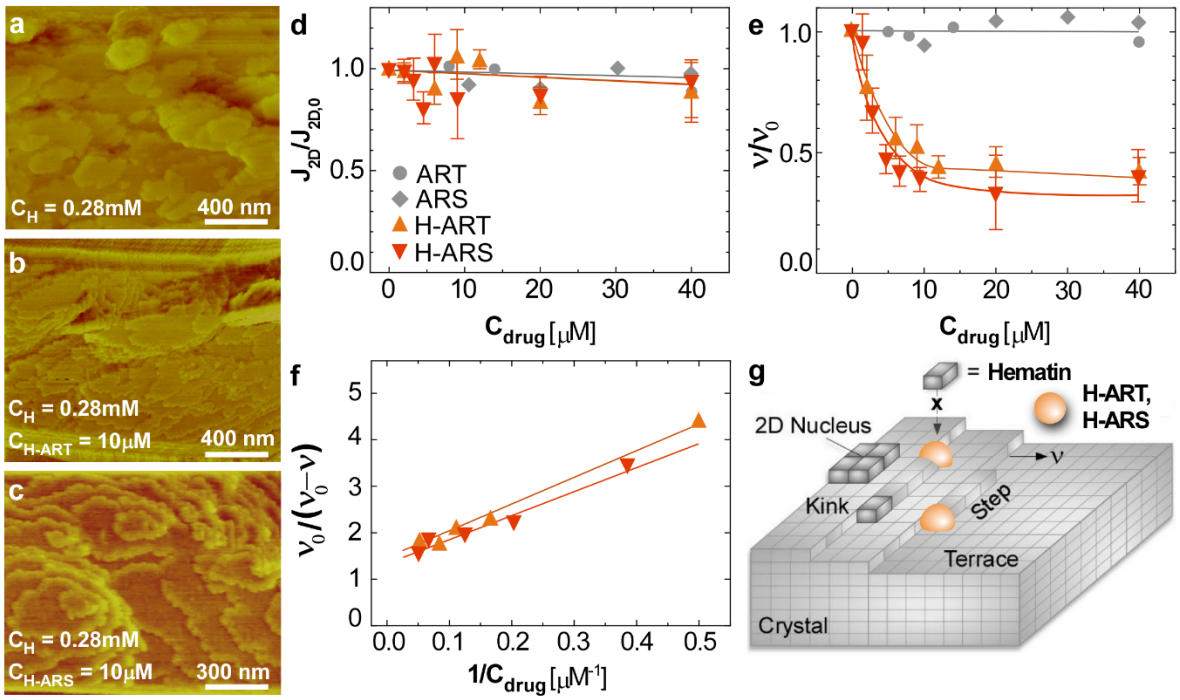

Figure 51. AFM analysis of parent drug and haeme-drug adduct inhibition of β-haematin growth.

To further confirm that artemisinin adducts can impact hematin crystallization by adsorbing on the crystallization surface. P. falciparum cultures were synchronized to the ring stage by incubation in 5% sorbitol. After 24 hour progression to the trophozoite stage, drugs were added at 500 nM for 6 h. The parasites were harvested by saponin lysis and frozen at –80 °C. Parasites were resuspended in 0.2% SDS/100 mM bicarbonate at pH 10 and centrifuged. Parasites were then resuspended in 100 mM bicarbonate pH 10 and

centrifuged. The hemozoin pellets were then washed 4 times in DI water. Frozen hemozoin was then “decrystallized” (or dissolved) with ammonium hydroxide before mass spectrometry analysis.

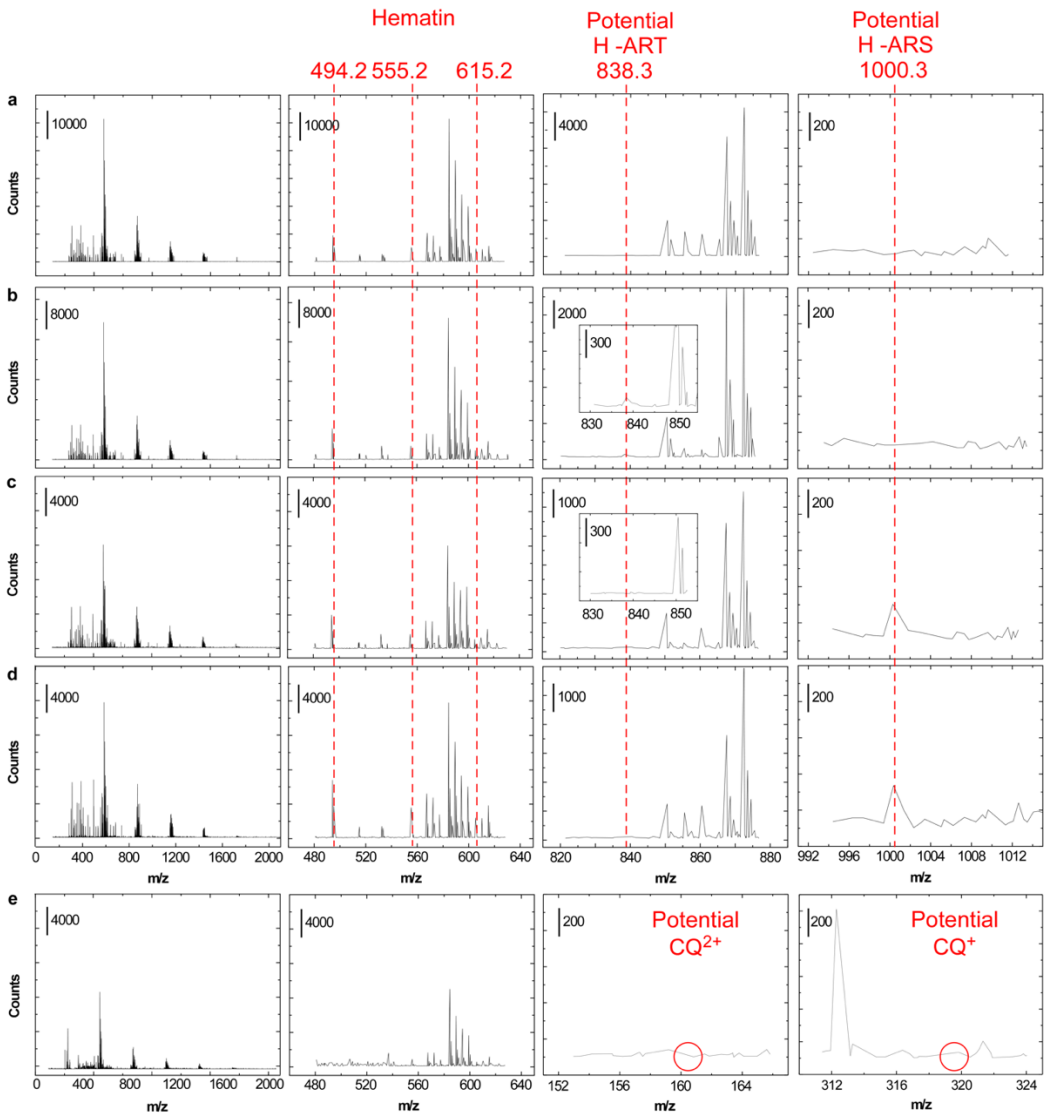

Figure 52. Evidence of drug association with haemozoin crystals.

6.4 Dual mechanisms of adducts

The idealized scheme in Fig. 51a depicts the erythrocyte stage of the *P. falciparum* life cycle. Chronic asexual replication is depicted in optical micrographs of *P. falciparum* cultures showing the early ring stage (Fig. 51a, I) followed by the trophozoite stage (Fig. 4a, II), which is marked by parasite growth and a change in morphology. During this period there is a breakdown of haemoglobin, generating free haeme (Fig. 51b) and initiating the formation and accumulation of haemozoin crystals. Nuclear division of trophozoites signals the onset of the schizont stage (Fig. 51a, III). *P. falciparum* cultures with known Kelch mutations have shown sensitivity to ART in the early ring and trophozoite stages (Fig. 51b, red shaded regions). Given that haemoglobin digestion is highest during the trophozoite stage, it is expected that H-ART would be most prevalent during this period where we have demonstrated its effective inhibition of haemozoin formation. Interestingly, *in vitro* assays reveal the haeme-drug adduct operates by a unique mode of action wherein exposure of β-haematin crystals to H-ART leads to irreversible inhibition, such that removal of H-ART does not lead to the recovery of crystal growth. Direct evidence for irreversible inhibition was obtained by monitoring the dynamic response of β-haematin crystal surfaces and the velocity of step advancement in the presence of H-ART and after its removal from the solution. Time-resolved *in situ* AFM measurements were conducted using concentrations of H-ART and haeme estimated from *P. falciparum* cultures: 10 □M H-ART is comparable to the dihydroartemisinin (DHA) concentration found in trophozoites exposed to DHA(*139*), and 0.28 mM haeme is comparable to concentration of soluble haeme in DCP Cam580Y trophozoites(*146*). At these conditions,

H-ART results in ca. 40% reduction in step velocity (Fig. 51c, stage 2). Holding H-ART concentration fixed, we increased the concentration of haeme to 0.50 mM to simulate an escalation in free haeme during the trophozoite stage due to the combined actions of haemoglobin digestion (Fig. 51b) and reduced haeme detoxification by H-ART crystal growth inhibition. This elevated haeme concentration promotes β-haematin crystallization in the growth medium, resulting in the deposition of nanocrystals (ca. 200 nm) on the (100) surface (arrow in Fig. 51d). While increased supersaturation is expected to result in higher growth rates, the nanocrystalline deposits inhibit the propagation of adjacent layers, leading to no observable change in step velocity (Fig. 51c, stage 3). This level of crystal growth inhibition was maintained even upon removal of H-ART from the growth solution (Fig. 51c, stages 4 and 5), signifying irreversible inhibition of step growth.

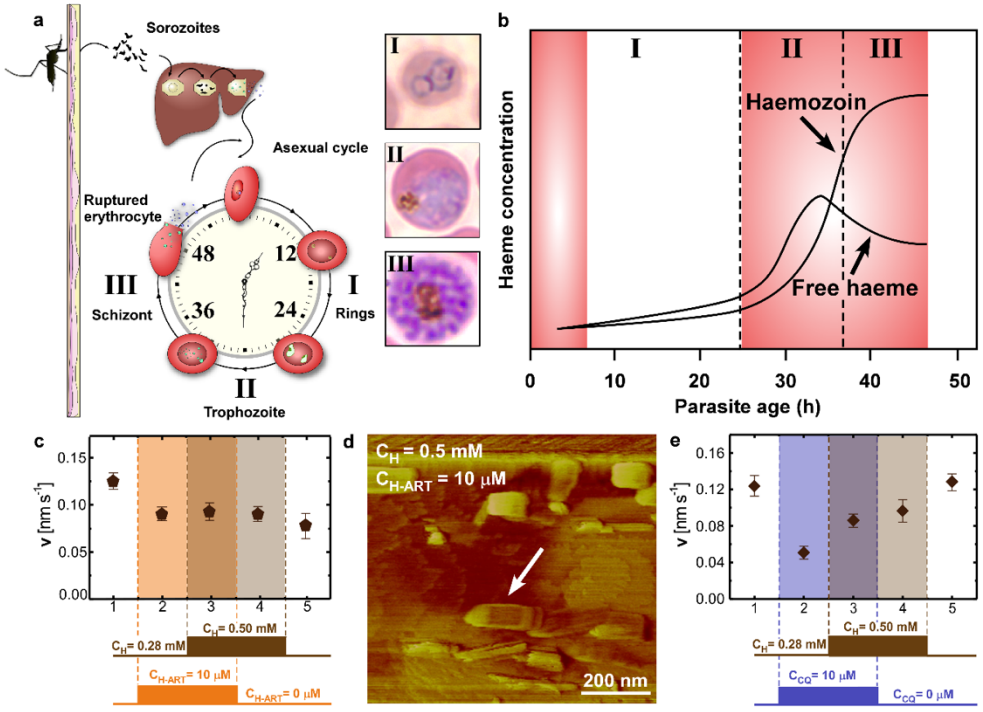

Figure 53. Dual action mechanism of artemisinin.

For comparison, a similar staged *in situ* AFM experiment was performed with CQ (Fig. 51e). Unlike H-ART, a step increases in haeme concentration in the presence of CQ did not lead to a noticeable generation of □-haematin crystals in the growth medium. Moreover, increased supersaturation resulted in a higher step velocity (Fig. 51e, stage 3) while the removal of CQ from the growth solution resulted in a progressive increase in step velocity such that a full recovery to the initiate state was observed within 2 - 3 hours of continuous imaging (Fig. 51e, stage 5). This indicates that the action of CQ is fully reversible, in stark contrast to the unique behavior of H-ART. These findings incite new questions regarding the generality of irreversible inhibition among artemisinins and how this additional mode of action could potentially alter artemisinin dosing regimens.

In summary, we address the prevailing hypothesis that artemisinin-class drugs exhibit a singular mode of action involving suicide activation and radical damage. Indeed, we show that adducts largely believed to be an inactive biomarker of artemisinins operate by a second mode of action during the trophozoite stage of the parasite life cycle. The efficacy and mechanism of haeme-drug adducts synthesized with two artemisinins were tested by a combination of *P. falciparum* cultures and *in situ* AFM measurements of β-haematin crystallization. Our findings reveal that both adducts efficiently kill parasites in cultures. For artemisinin-resistant strains, adducts are more effective than their respective parent drugs at lower doses. Analysis of haemozoin crystals isolated from parasites treated with artemisinins demonstrates that adducts H-ART or H-ARS are associated with the crystals, consistent with time-resolved measurements of β-haematin crystallization with varied haeme and drug concentrations, revealing a unique mode of

irreversible crystal growth inhibition. This unanticipated mechanism has potential implications for understanding haeme detoxification *in vivo*, such as the ability of haeme-drug adducts to force free haeme concentrations above the toxicity limit after depletion of the drug in resistant parasites. Retained suppression of haeme detoxification after drug removal is a direct way to circumvent resistance to artemisinins via a mechanism that is distinctly unique compared to those of quinoline-class antimalarials.

Chapter 7 Nonclassical inhibition of crystal growth by promoting cooperativity in the solution and at the growth interface

Crystallization is the central process of materials synthesis in biological, geological, and extraterrestrial systems. Nature achieves remarkable diversity of shapes, patterns, compositions, and functions of the arising crystalline structures by combining simple strategies to control the number of nucleated crystal and the sizes to which they grow. To promote or inhibit crystallization in both natural and engineered environments, soluble foreign substances are deployed that interact with the solute or the crystal-solution interface. For solution grown crystals, the formation of hematin crystals follows a classical mechanism whereby new crystal layers are nucleated on top of existing ones and spread to cover the entire face. Direct observations established two classes of quinoline inhibition mechanisms. In the first mechanism, known as step-pinning, inhibitors bind to flat terraces and arrest step growth over broad areas of the crystal surface. Alternatively, inhibitors may associate and block kinks, the sites where solute molecules incorporate into steps. We examine the growth of beta-hematin crystals, a component of the physiology of malaria parasites, in the presence of artemisinin and quinoline derivatives, drugs that represent the current front line of antimalarial defense. We demonstrate two novel mechanisms of growth inhibition. At moderate hematin concentrations, a heme-artemisinin adduct, H-ART, promotes copious nucleation of hematin nanocrystals in the solution bulk, but impedes their growth above ca. 100 nm. The nanocrystals associate to the surface of larger hematin crystals and completely arrest their growth. The strain due to the imperfect incorporation of the nanocrystals constrains

growth even after H-ART is removed, leading to irreversible inhibition. Pyronaridine, PYR, a quinoline of relatively large size, suppresses nucleation of nanocrystals in the solution bulk and exhibits an entirely different mechanism of growth suppression. PYR stabilizes pairs of steps and leads to abundant step bunching. At elevated hematin concentrations, the step bunches engender solute occlusions that resolve as screw dislocations outcropping on the crystal interface. The high density of steps originating at the screw dislocations strongly delays step propagation owing to competition for supply between adjacent steps. Removal of PYR does not restore the initial growth rate value since the high step density is preserved. Besides, we demonstrate that drug pairs, whose constituents employ distinct mechanisms of hematin crystallization inhibition, kink blocking and a step pinning, exhibit both synergistic and antagonistic cooperativity depending on the drug combination and applied concentrations. Whereas synergism between two crystal growth modifiers is expected, the antagonistic cooperativity defies current crystal growth models. We demonstrate that the kink blockers reduce the line tension of the step edge, which facilitates both the nucleation of new crystal layers and the propagation of the steps through the gates created by step-pinners. The two examples of functionalities of inhibitors may provide guidance in the search for suitable inhibitors control crystallization of pathological, biomimetic, and synthetic materials. In a broader context, our results highlight modifier interactions mediated by the dynamics and structures in the solution and on the crystal interface as a primary element of the regulation of the shapes and patterns of crystalline structures in nature and industry.

7.1 Nonclassical Crystal pathways

From previous works, we concluded that inhibitors can block crystallization that follow classical nucleation theory by incorporating into kink sites or adsorbing on the crystal terrace. With the solute or the crystal-solution interface are deployed to promote or inhibit crystallization (*24*). Nature achieves remarkable diversity of shapes, patterns, compositions, and functions of the arising crystalline structures by applying ingredients that control the number of nucleated crystals and their anisotropic rates of growth (*22, 23, 147-149*). The consequences of additives on crystal nucleation are typically discussed within the models of heterogeneous nucleation and modifier adsorption,(*105, 150, 151*) whereas their effects on crystal growth are rationalized within two established mechanisms:(*17, 62, 82, 88, 100, 110, 114, 115, 152-158*) step pinning, in which inhibitors bind to the terraces and arrest layer growth over broad areas of the surface)(*152*) and kink blocking, where the inhibitors occupy kinks, the only sites where solute molecules incorporate into steps.

Physiological crystallization, such as the accumulation of cholesterol crystals in arterial walls,(*159*) often selects lipid environments. The interactions of an organic solvent with the solute and modifier and the contacts between solute and modifier molecules are largely constrained to van der Waals forces and may drastically diverge from those operating in water-based solutions, where H-bonding dominates (*160-163*). The disparity in the interactions that regulate the molecular-level structures and dynamics in organic crystallization may mobilize distinct operating mechanisms. In contrast to aqueous solvents, the level of understanding of the fundamental processes of crystal growth from

organic solvents is severely limited (*164-166*). In most cases, optimization of the growth processes is carried out by trial-and-error or by mimicking practices developed for other compounds (*167*). The lack of insight into the fundamental mechanisms of how foreign compounds modify the molecular pathways of crystallization has emerged as a major obstacle to a rational approach to optimize and control organic crystallization (*168*).

The accepted models of modifier activity presume that crystal nucleation and growth advance along classical pathways. Perhaps the most sequential assumption of the classical approaches, the "Szilard postulate"(*169*), is that crystals nucleate and grow by association of single solute molecules (*170*). In the last 15 years, elaborate experiments accumulated significant discrepancies with the nucleation and growth behaviors predicted by classical theory (*20, 171-173*). Many of the deviant features involve mesoscopic crystallization precursors, ordered or disordered, which assemble in the solution independently of crystallization and may both facilitate nucleation and feed a fast mode of crystal growth (*20, 171, 174-176*). With a few exceptions,(*24, 29, 177, 178*) how additives impact the properties of the crystallization precursors to enhance or suppress crystal nucleation and growth has not been examined.

Another gap in our understanding of how foreign compounds affect crystallization relates to the activity of two modifiers that operate in tandem to alter crystallization processes (*179-181*). Intuitively, we expect a second inhibitor to enhance the impact of its partner; such cooperativity would be classified as synergistic or additive according to whether the response to a combination of two inhibitors is stronger or equal to the sum of the responses to individual doses (*93*). Surprisingly, examples of antagonistic

cooperativity, where a pair of inhibitors suppress crystal growth less than the sum of their individual activities, abound (*48, 100*). The insight into the molecular mechanisms that may guide the three distinct cooperativity modes appears to be limited to a recent work by our group on the combined action of step pinners and kink blockers (*182*).

7.2 nonclassical inhibition induced by antimalarial drugs

Malaria parasite can digest hemoglobin in its lifecycle and one of the byproducts, hematin, is highly toxic to the parasite's membrane. The parasite reduces the concentration of free hematin by transferring hematin into hematin crystals. When classical antimalarial drugs given to a patient, they entered the human circulatory system to reach the parasite DV, stop the crystallization and raise the level of hematin. We explained the mechanisms how antimalarials stop hematin crystallization at the supersaturation around 1.7. When the crystallization stopped initially and the hematin begins to accumulate in the DV. As the high concentration increases the driving force for nucleation and crystal surface expansion, will the antimalarial drugs still stop the hematin crystallization. Will the antimalarial drugs stop the crystallization with same mechanism or they take an alternative pathway? Besides, As the life time of antimalarial drugs are general shorter than period for every dosage applied to a patient, how could those antimalarial drugs remain effective? To answer those question, the response of hematin surface was tested at raised hematin concentration in the presence of antimalarials.

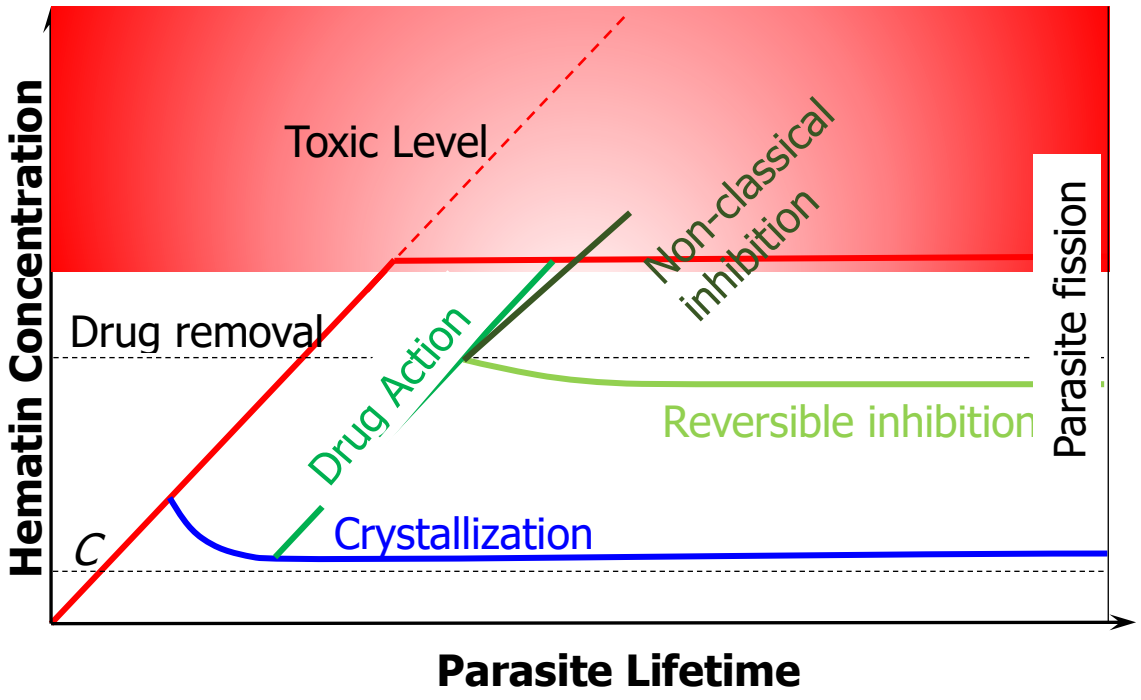

Figure 54. Hypotheses of consequences at high concentration of hematin.

7.3 Monitor the nucleation rate with dynamic light scatting

We monitored the nucleation of hematin in the presence of antimalarial drugs. Dynamic light scattering (DLS) records the movement of molecule visible by measuring the amount of light diffracted by the particles. Three different concentrations of hematin, compared with four different drugs, CQ, PY, H – ART, MQ, were tested how antimalarials impact on the timescale of increasement of DLS correlation function.

7.3.1 Pure hematin solution

For pure hematin, we test time evolution of three different concentrations, 0.28 mM, 0.50 mM and 0.60mM. Freshly hematin solutions were prepared and filtered with 0.20 μm membranes. The measurement displayed a linear line at t = 0min, that indicts the solution did not contain any particles within the detectable range. The correction

function began to show at around t = 10 min (180 min for 0.28 mM hematin solution) and the amplitude kept increasing until reached a maximum value equals to 0.9. The size calculated from the correlation function showed that the particle generated from solution is about 200 nm in diameter that indicts those particles should be nanocrystals as the cluster has a much smaller size in general. The amplitude indicted that the amount of particle is increasing overtime and increasing time in amplitude of correlation function is enhanced with higher concentration. The observation fits the expectation that increasing concentration will increase the rate of 3D nucleation. The fact that mo secondary shoulders were observed though larger crystals appeared in the later experiments suggested that 200 nm is maximal size that the buoyance can hold. Any particles larger than the size will deposit on the bottom of a vial and did not get recorded in the experiments.

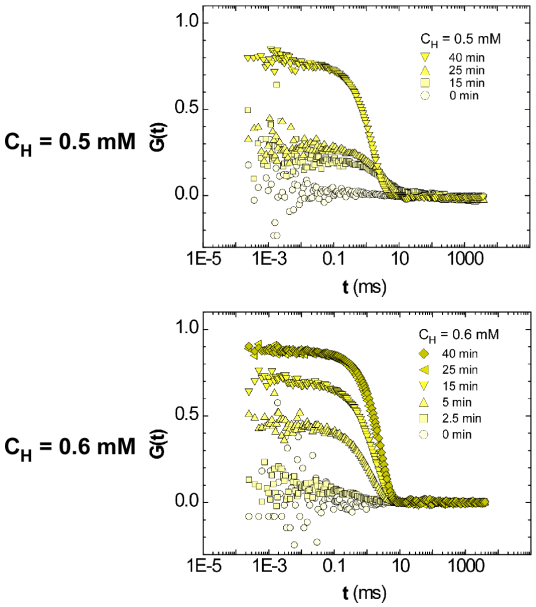

Figure 55. Time evolution of DLS correlation function for pure hematin.

7.3.2 hematin with antimalarial drugs

Freshly prepared hematin solution was mixed with different antimalarial drugs. The concentrations of antimalarial drugs were determined from previous experiments (*75*). Mixed solutions were filtered with 0.2 μm membrane and the time evolution were monitored with DLS. All solutions displayed a similar correlation function after they reached the plateaus for amplitude that indicts same nanocrystals with size around 200 nm were generated. Those antimalarials did not change the morphology of crystals. For all four drugs, CQ and MQ did not change the nucleation rate, PY decreases the nucleation rate and H – ART reversely increase nucleation rate. The phenomenon will be further discussed in the cluster chapter.

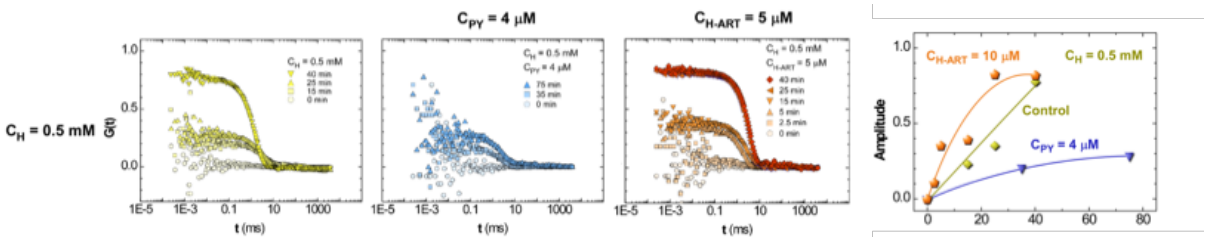

Figure 56. Time evolution of hematin solution in the presence of antimalarials.

7.4 Nonclassical behaviors of (100) hematin surface at high hematin concentration

Intricate crystal architectures in nature evolve shepherded by minority solution components (*183-185*). Industrial crystals are guided to preferred morphologies by select modifiers (*149*). In both cases, the modifiers' activity is commonly ascribed to their reversible adsorption to crystal surfaces (*152, 186*) or to kinks along the growth steps (*110, 112*) where they, respectively, pin the steps or block the kinks needed for growth; these two classical models inevitably predict that growth resumes after the inhibitor is removed.

Copious instances of permanently poisoned crystals and terminal crystal sizes persist out of the realm of the classical mechanisms and remain elusive. A mechanism of irreversible inhibition, sometimes discussed in the literature, relies on accumulation of foreign molecules in the crystal bulk that strain the lattice, increase its chemical potential and thus lower the crystallization driving force. Two novel mechanisms of irreversible inhibition that initiate by cooperative phenomena either in the solution or on the growing crystal surface are suggested by our preliminary results below.

Research initiatives towards discovery of high concentration response will explore the molecular details of the mechanisms of irreversible growth inhibition. The sought insights will guide the rational identification of molecules projected to invoke either of the two mechanisms.

Previous results indict that at high supersaturations, the structure of the surface of a growing hematin crystal dramatically changes (*72*). To probe the consequences of the expected structural evolution of the crystal surface and the phenomena in the solution bulk driven by high supersaturation, we monitored the dynamic response of hematin crystal surfaces and the velocity of steps *v* in the presence of a heme-artemisinin adduct, H-ART,(*187*) pyronaridine, PY,(*88*) and chloroquine, CQ,(*88*) and after the removal of these inhibitors from the solution (Fig. 5). Time-resolved *in situ* AFM observations reveal that introduction of H-ART at 10 μM to 0.28 mM hematin solutions reduces the velocity of growth steps by about 40%, consistent with previous findings (*88, 187*).

As discussed in the previous chapter, growth rate increases linearly while 2D nucleation rate increases exponentially with concentration. AFM images of (100) surface in pure hematin solution displayed that more 2D nucleus are generated on the terrace at high concentration. The crystal may adopt a new method of growth at very high concentration where the rate of nucleation exceeds the ability for 2D nucleus to spread. The surface begins to transfer from a smooth surface to the rough surface characterized the interstep distance reduces to an indistinguishable level. The work is described elaborately in Katy Olafson's work (*188*). In the presence of antimalarials, the surface remains smooth as a result that the nucleation is largely hindered.

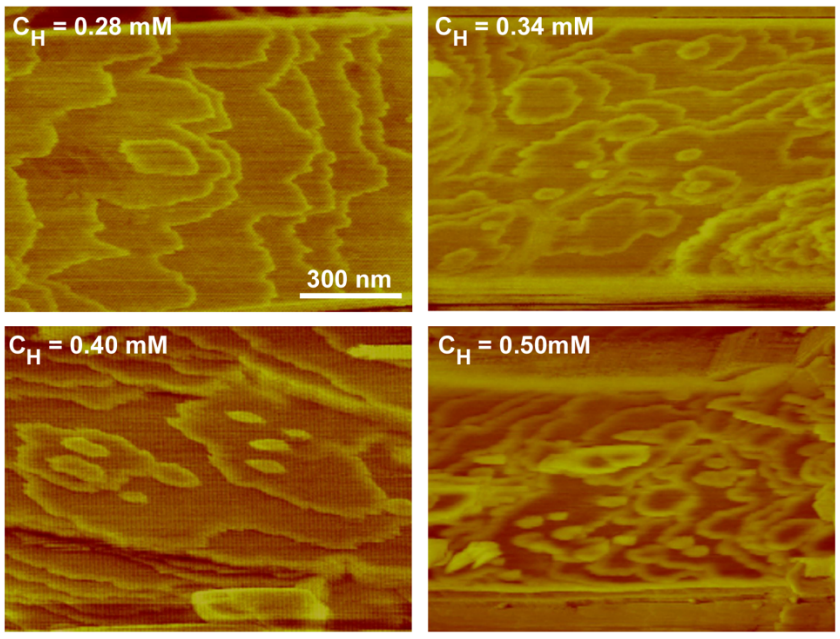

Figure 57. Images of (100) surface at different hematin concentration.

A few small crystals were observed dropping on the hematin surface at high concentration that is consistent with DLS results that small crystals are forming rapidly.

Those small crystals can grow larger on the surface and incorporate into the original crystal.

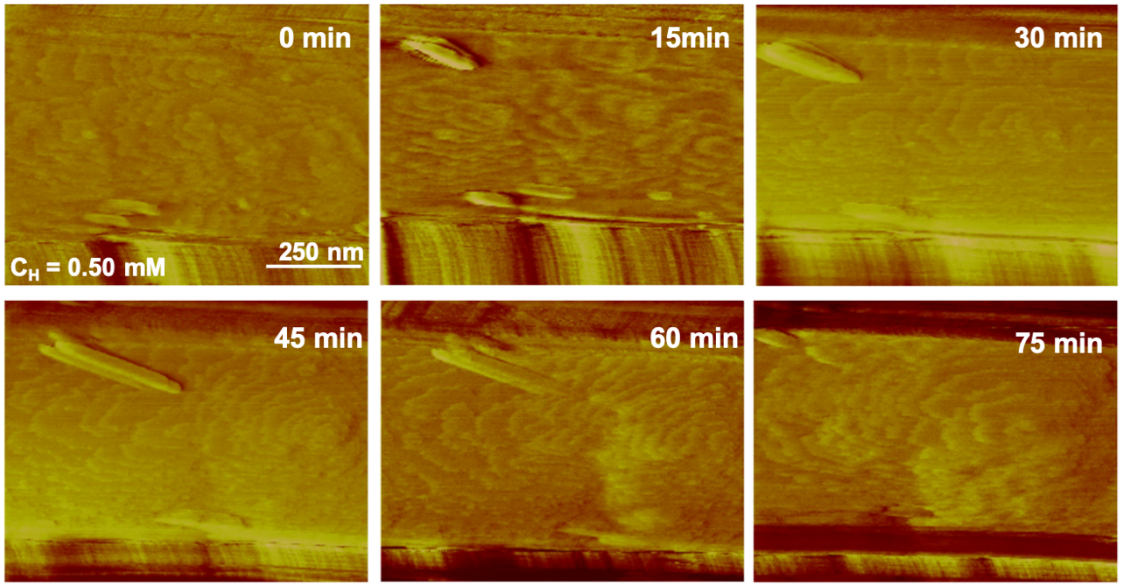

Figure 58. AFM images of small crystal dropped on the surface can grow into structure.

DLS showed that MQ and CQ won't affect the nucleation rate while previous AFM studies showed MQ inhibits hematin crystal by kink blocking and CQ modify crystal growth by step pining mechanism. At high concentration, crystal surface displayed similar behaviors that performed at low concentration. Steps are slightly conjugated due to the inhibition effects from inhibitors.

The delay in the increment of correlation function in the presence of PY indicts PY can somehow modify the pathway of nucleation of hematin. The mechanism behind the change is vague and only few researches reported that the nucleation rate can decreased (*11*). Previous study proposed that the Mg^{2+} can stable the amorphous calcium by changing the water structure on the surface that may not apply in our case. The

mechanism for PY was proposed as a step punching inducer that can crosslink steps and lead to the formation of multilayers. AMF images showed that PY can induce macro steps on the terrace that developed into dislocation center later. The dislocation centers are increasing when increase hematin concentration and eventually thrift hematin crystallization from 2D nucleation dominates to desolation dominates. At high concentration, steps are closely packed and the step distance is low. The intently packed steps reduced the molecules incorporated from surface diffusion pathway and enhance at the high concentration the growth rate is lower than it displayed for pure hematin solution.

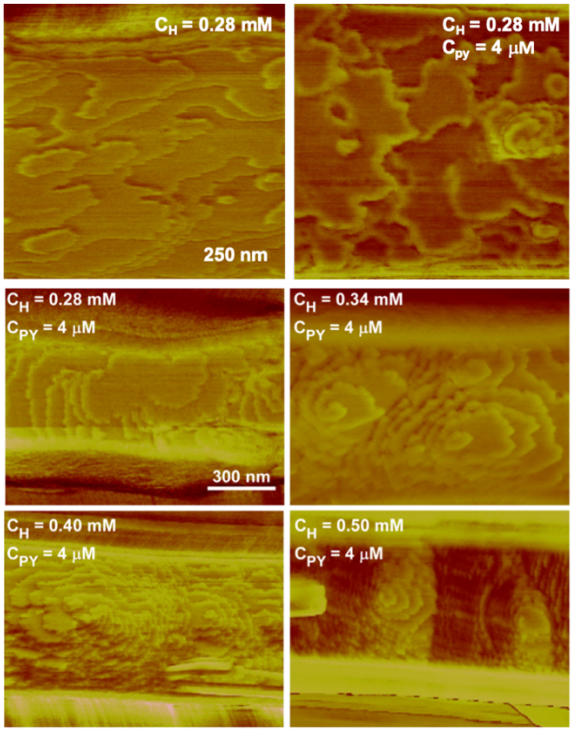

Figure 59. Macrosteps on the terrace and lead to dislocations. Dislocation distribution according to the hematin concentration.

Inversely, H – ART promotes the nucleation of hematin. When H – ART concentration is 5 μM, the time to reach the plateaus is about a quarter of pure hematin solution at 0.5mM. The correlation function indicted the nanocrystals have the same size with those produced in pure hematin solution. Besides bulk studies showed that the final crystals grown from those nanocrystals have identical morphology and PXRD patterns. All the results suggested that antimalarial drugs can alter the nucleation without changing final products.

The increasing nucleation rate lead to a boost in the number of crystals dropped on the surface. Unlike small crystals generated on the pure hematin solution, those small crystal won't grow on the hematin terrace and steps under and around the attached crystals are growing significantly slower than free steps.

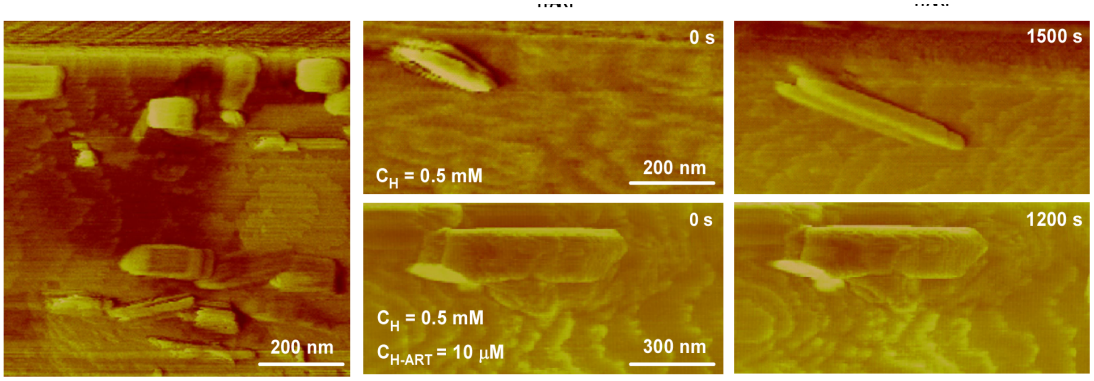

Figure 60. H – ART increased the formation of crystals and restrained the growth of crystals.

7.5 Irreversible inhibition induced by nonclassical pathways

At high hematin concentration, we observed that PY and H – ART modified crystallization pathway either by inducing the dislocation center or promoting the generation of strained small crystals. As we discussed before, we are investigating the

period that drugs passed their lifetimes and yet the new doses have not been applied. To understand how antimalarials drugs remain effective during this period of time, we replaced the growth solution with pure hematin solution after the crystals have been in contact with the drug solution for certain amount time. Furthermore, we reduced the hematin concentration back to the initial state and monitor the behaviors of (100) hematin crystal surface. The results were characterized by measurements of growth rate and 2D nucleation rate. The results indict that MQ and CQ may be reversible inhibition that means crystal can back to grow in the normal 2D pathway as we removed antimalarial while crystals in contact with PY and H – ART will remain inhibited though the pure hematin was used by two different mechanisms.

AFM images displayed that MQ and CQ can both lead to a relative rough surface at high concentration of hematin. The growth rate and nucleation rate are still increasing by increasing hematin concentration despite the presence of CQ and MQ. After the remove of drugs, the surface remains inhibited for a short time though the increment in both growth rate and nucleation rate were observed. The surface is still relatively rough due to the high concentration of hematin that the system is already in the regime of roughing transition state. After drop the concentration of hematin solution back to 0.28 mM, Fewer nucleus are observed on the surface and those islands begin to spread. Eventually, the surface become smooth and has similar outfits with the surface grow in the pure solution. Besides, the growth velocity and 2D nucleation rate turned back to the normal state. We proposed that hematin crystal inhibited by CQ and MQ is a reversible process. After parasite sequestrate all the drugs from DV, hematin crystals may back to

grow and reduce the efficiency of killing rates. One thing we have not concluded is how much drugs will be presented in the malarial parasite DV and how long will it take to get rid of all the drugs. To answer those question, we collaborated with Victoria Balta and Dr. David Sullivan to test the real responses of malarial to antimalarials drugs during the ring stage and trophozoite stage.

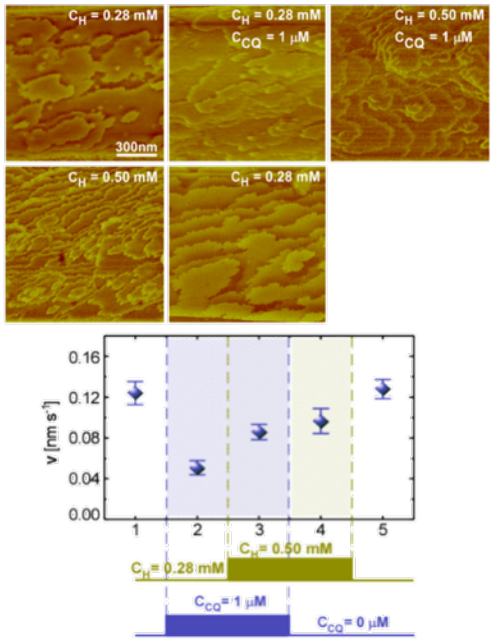

Figure 61. Irreversible test for CQ.

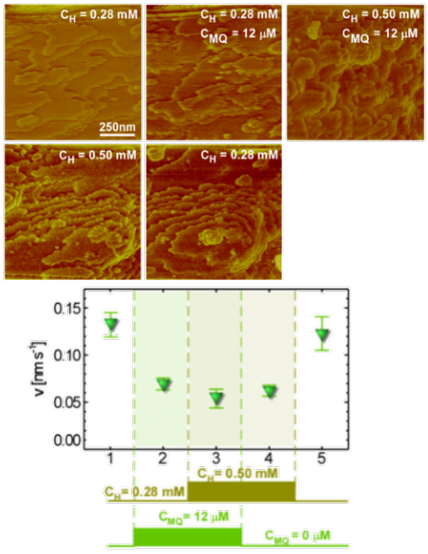

Figure 62. Irreversible test for MQ.

As discussed before, PY can induce dislocations by generating macrosteps. When PY was introduced at high concentration of hematin, high density of dislocations is generated on the (100) surface. Dislocations are most likely from the line tension induced by the PY and will not disappear after the removal of PY. Reducing hematin concentration back to 0.28 mM only slightly increases the step distance due to the highly packed dislocations. Furthermore, the crystal is adopting dislocation as the growth mechanism instead of 2D nucleation. The overall growth rate will not go back to the original speed.

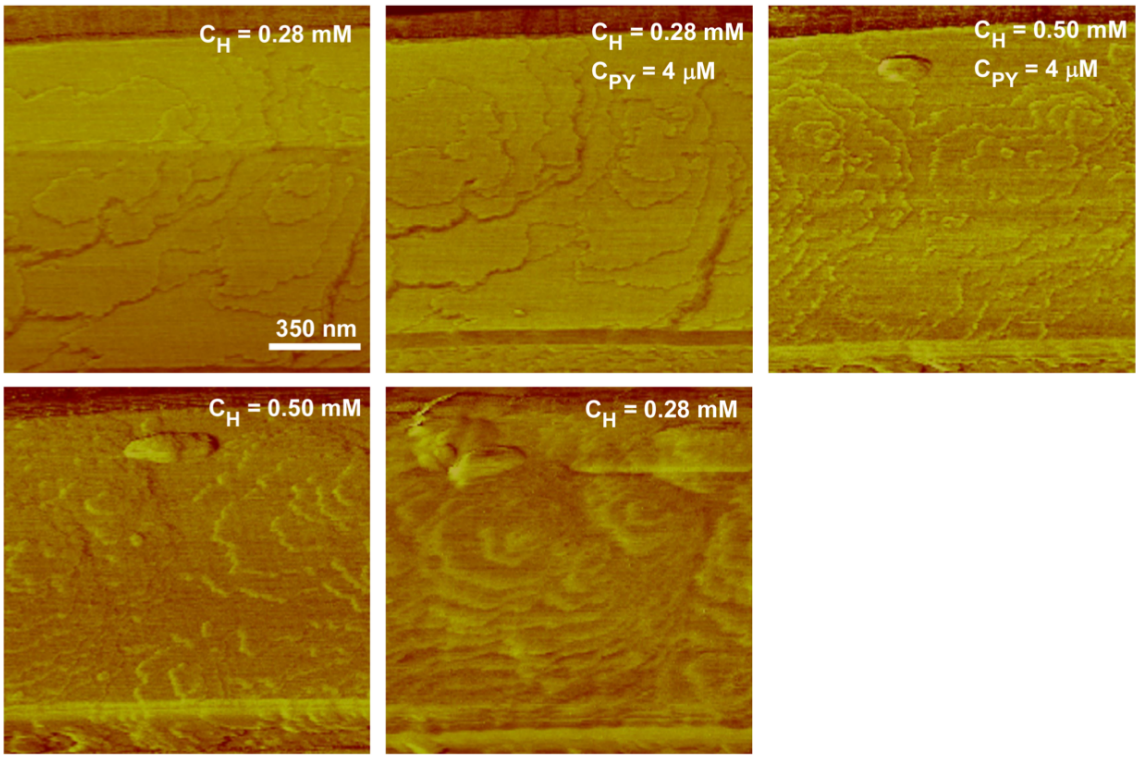

Figure 63. Reversible test for PY.

We found that at the hematin concentrations elevated to 0.5 mM, H-ART enhances the nucleation of hematin nanocrystals (similar to the effect of the heme-artesunate adduct and then suppresses the growth of the nanocrystals when they reach length of about 200 nm. The nanocrystals land on the surface of a growing large hematin crystal. Removing H-ART from this solution arrests the nucleation of nanocrystals. The nanocrystals already on the surface of the large crystal are buried under growing steps. Their incorporation in the crystal at non-crystallographic orientations strains the lattice (*103, 189*). The accumulated elastic energy lowers the driving force and delays step propagation at both hematin concentrations: 0.5 and 0.28 mM.

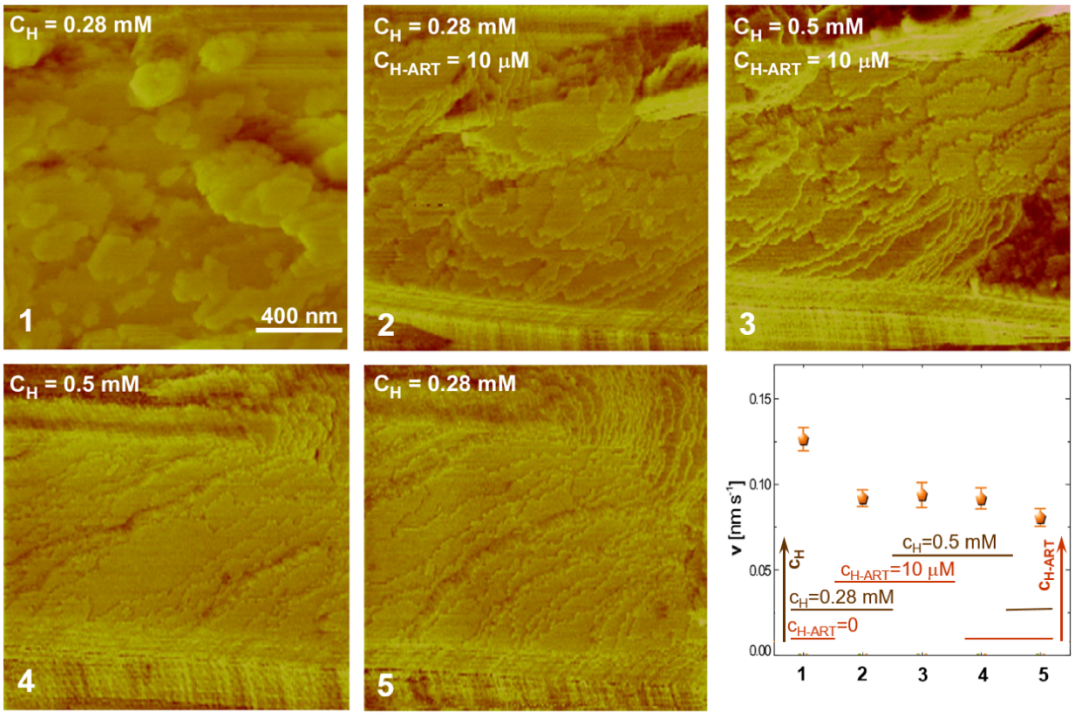

Figure 64. Reversible test for H – ART.

7.6 Reversibility in bulk crystallization and malaria assays.

The reversibility of 5 different drugs, CQ, MQ, H – ART, H – ARS and PY were further test in bulk crystallization assays. Hematin crystals were grown with the method described in the previous chapter at a concentration of 0.20 mM with antimalarial drugs. Small crystals were observed at the interface of two deposited glass slides after three days after located in the dark. One slide was transferred into a freshly prepared solution with same components like the solution applied before and another one was transferred to the pure hematin solution with a same concentration. The transferred crystals are left in the dark for 7 more days. Final crystals were imaged with scan electron microscopy and characterized by the length and width.

The difference between the length reviewed whether the crystal still remains inhibited after the removal of drugs. The irreversible inhibition will lead to a larger

difference because the crystal cannot fully recover once the features were developed during the first three days.

The data indicated that PY and H – ARS lead to an irreversible inhibition, that is partially consistent with the conclusion from AFM studies. H – ART displayed a reversible result in the bulk study that indicts that surface may be able to fully recover after long term exposure to pure hematin solution as the contact time in bulk study is about 20 times longer than the exposure time in AFM. H – ARS remains irreversible as H -ARS presented a much stronger ability to increase the rate of nucleation and the defected surface may take longer time for recovery compared to H – ART. Crystals from PY batches are heavily tapered at the crystal edge which might be a consequence of changing the growth pathway.

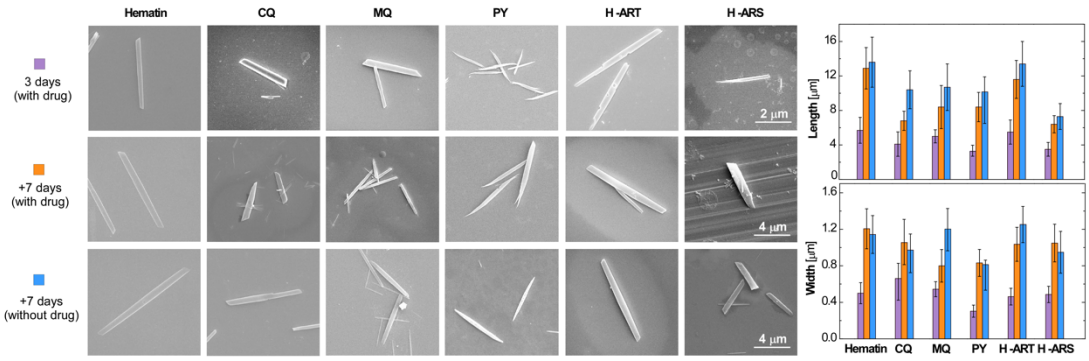

Figure 65. Bulk assays for crystals grown from different intermedium.

We expect to have more answer from biological tests. Antimalarial drugs were applied at different stages of malaria and the survival rates were compared. The result partially indicted the existence of irreversibility may lead to the delay of recovery of malaria population. However, more information is required to draw the conclusion as the

mechanism how drugs transfer into the parasite DV and released by the parasite is still unknown.

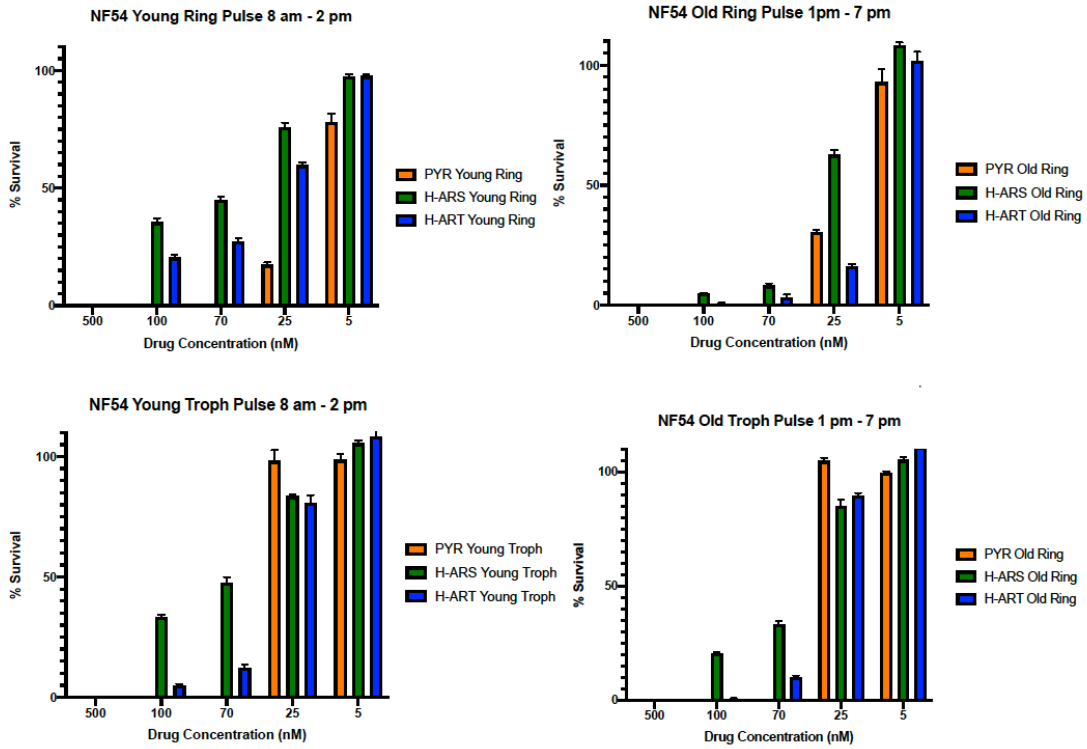

Figure 66. Parasite survival rate after different concentrations of antimalarials were applied to three different stages of parasite lifecycle.

Additional information for who wants to work in hematin work:

Lumefantrine may also change the pathway of hematin nucleation. Aggregation were observed and the transformation was partially confirmed. Data won't show here.

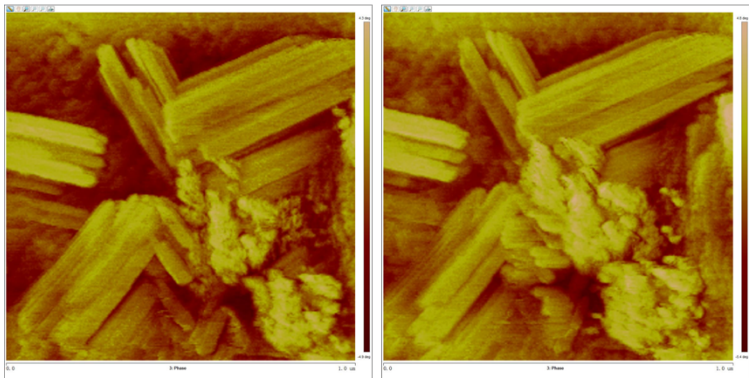

Reserved figures.

Chapter 8. suppression and enhancement of crystal nucleation by controlling the population of nucleation precursors.

Classical nucleation theory (CNT) identifies three parameters that govern the rate of crystal nucleation: the solution supersaturation, the surface free energy of the interface between the nucleus and the solution, and the solute concentration. The concentration correlates to the supersaturation, which, in turn, is a coarse regulator of nucleation. Modest supersaturation variations often completely suppress nucleation or invoke dramatic shifts to unwanted crystal morphologies and polymorphs. Efforts to modify the free surface energy γ by surfactants are constrained by the negative adsorption of modifiers that increase γ, a corollary of the Gibbs adsorption principle. Surfactants have been employed to enhance nucleation rates, and their activity has been attributed to their positive adsorption on the nuclei.[100,101]

An alternative means to enhance crystal nucleation is to engage heterogeneous substrates that support the emerging crystal nuclei.[1,13] CNT suggests that the barrier for nucleation assisted by heterogeneous substrates is lower owing to the smaller volume of nuclei that strongly adhere to the substrate,[1] which drives nucleation rates faster by orders of magnitude.[13]

Numerous industrial tasks require suppression of nucleation.[104] The elaborate structures of minerals suggest precise nucleation control that consists of suppression of nucleation throughout and enhanced nucleation at a perfectly selected location.[105–107] Robust suppression of nucleation cannot be understood or designed within the realm of classical theory. Strategies to suppress nucleation, however, naturally arise for two-step

nucleation. Nucleation can be inhibited by destroying the disordered precursors that host crystal nuclei or by engineering the cluster properties to constrain crystal nucleation.

8.1 Antimalarial modifies hematin nucleation

Nucleation is the first step for crystallization and plays an important role in controlling the polymer. Controlling nucleation is an important strategy to control the properties of crystals. However, the major challenge, both in space and in time, held the step of development. Nucleus and intermedium formed from nucleus are usually in a dimension of nanometer and the rate of formation is in the scale of microsecond. Existing techniques, such as in-situ TEM, can only partially reveal the progress of nucleation and the detailed mechanisms are still veiled. Following previous study that showed antimalarial drugs can modify the rate of generation of hematin nanocrystal, we continued investigating how antimalarial drugs can modify the nucleation time and try to understand the importance of clusters behaviors.

The conclusion of DLS measurements showed that CQ and MQ won't change the nucleation time, PY prolongs it and H – ARS / H – ART accelerate. We hypothesis that crystal nucleation can be inhibited by suppressing the population of nucleation precursors in the solution. We will establish the mechanism of formation of the nucleation precursors in organic solutions and propose means to control their concentration and volume.

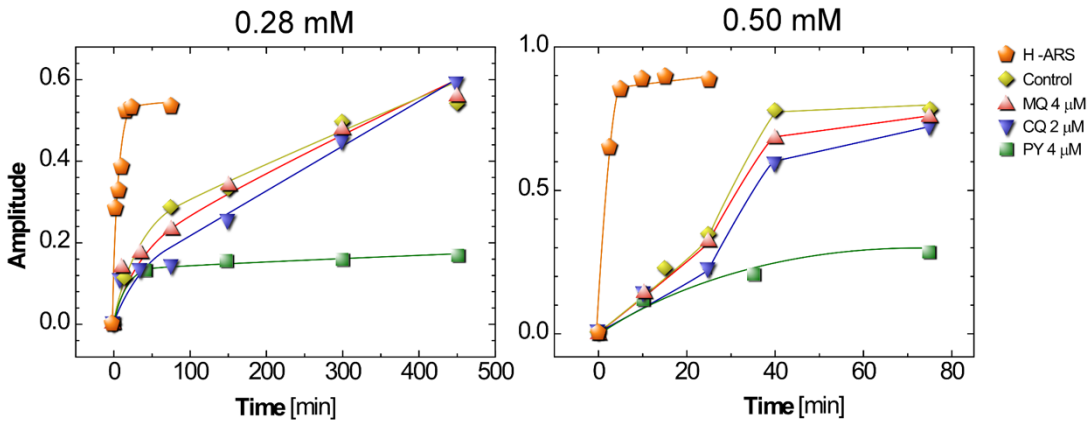

Figure 67. A conclusion of the evolution of amplitude of hematin solution in the presence of antimalarial drugs

8.2 Cluster behaviors in the presence of antimalarials

Hematin forms crystals elongated along their $\vec{c}$ crystallographic axis (*62, 66, 73, 84*). In a supersaturated solution with C = 0.50 mM (the solubility at 22°C is 0.12 mM) the scattered light intensity and the respective correlation function $G(\tau)$ (τ, lag time) rapidly grow announcing fast nucleation of crystals (Fig. 4B). The addition of the heme-artesunate adduct H-ARS(*187*) substantially accelerates nucleation, whereas mefloquine (MQ) and chloroquine (CQ)(*88, 190*) are passive bystanders. Importantly, pyronaridine (PY)(*88*) suppresses nucleation. The nucleation enhancement by H-ARS and the passivity of MQ and CQ can be understood within the CNT predictions (*23, 170*). The nucleation suppression by PY falls outside of the realm of CNT and suggests that hematin crystal nucleation may follow a non-classical pathway (*170*). Transmission electron microscopy (TEM) characterization of supersaturated hematin solutions supports this hypothesis. The micrographs reveal the presence of amorphous particles with diameters ranging from 70 to 250 nm that assist the nucleation of elongated hematin crystals, analogously to

previous observations on crystal nucleation of perylene(*191*) and several proteins and minerals (*170, 173, 175, 192*). Further evidence that the amorphous particles host crystal nucleation emerges from the electron diffraction patterns of several particles that represent superpositions of amorphous and crystal signatures.

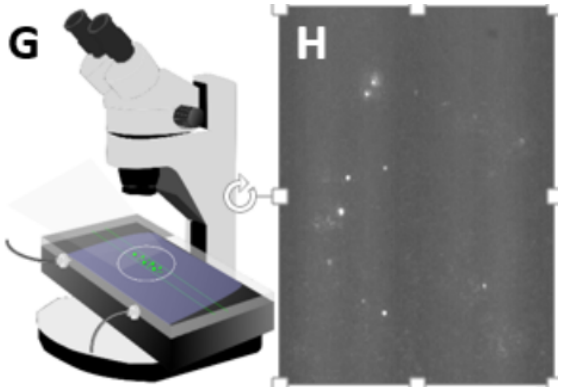

Figure 68. Illustration of nanosite and particle observed from camera view.

In the DLS studies, we reported the size of nanocrystals evolution time and the resolution was limited to test the behaviors of clusters. To achieve more information, we adopted nanosite to monitor the movement of individual cluster and estimate the size distribution by tracking the trace of random walk.

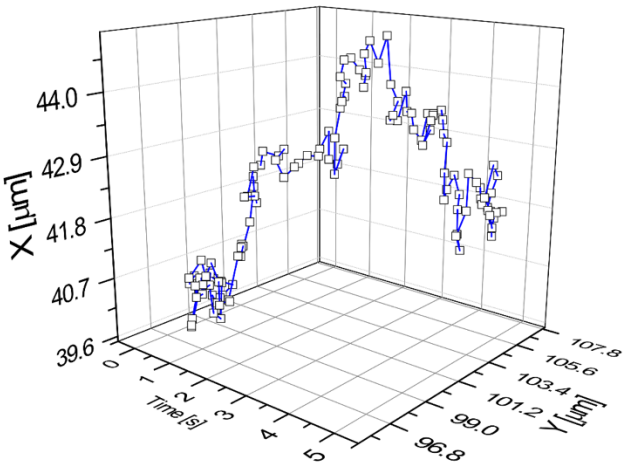

Figure 69. The trace of the movement of single cluster in the solution.

As the movement of every particle was recorded and the size was calculated, the size distribution can be extracted for different solutions. Eventually, the average size of particles in the solution was reported.

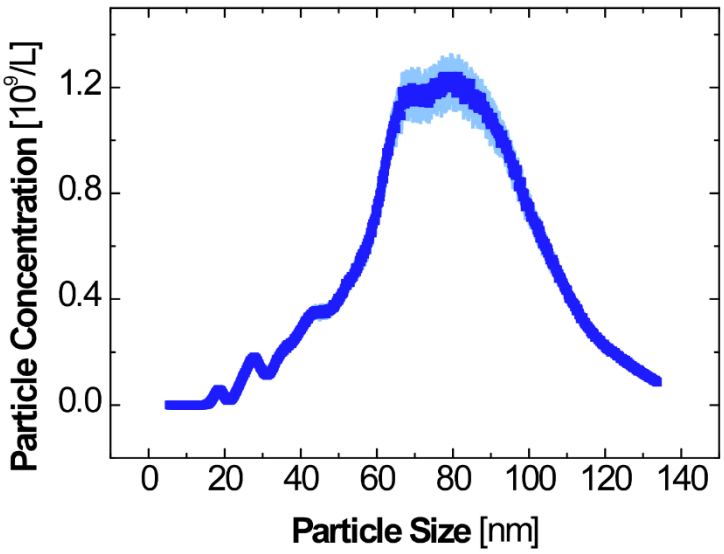

Figure 70. Size distribution of particles in the hematin solution.

To further confirm observed particles are clusters, the evolution of particle over time was recorded. At the solubility, particles remain stable after 24 hours test. Varying the centration of hematin won't change the size of particle. Those facts indicted that those particles are clusters.

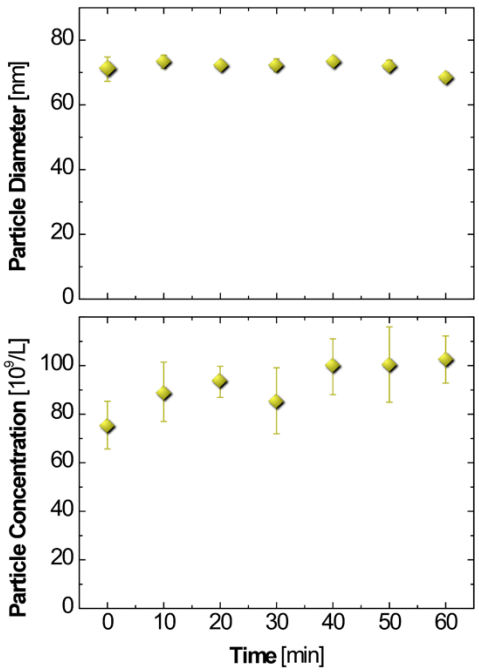

Figure 71. Time evolution of hematin solution at solubility.

Two important properties can be extracted from Nanosight videos are the density of clusters in the solution and its size distribution. We tested different concentrations of pure hematin solution and hematin solution along with antimalarial drugs. At concentration 0.13 mM that is lower than the solubility 0.16mM at the room temperature, a few clusters were observed. The existence of particles in the under supersaturated solution suggested that those particles should be clusters instead of nanocrystals because no crystals can be generated in the undersaturated solution. Those particles remain the

same size after several hours with a relatively constant population density. The number of particles increased dramatically by increasing hematin concentration from 0.13 mM to 0.28 mM and the size of particles remain the same. When the hematin solution beyond the solubility, those clusters will growth largely and eventually transferred to hematin nanocrystal. We applied double layer polarizer between the camera and the view window. The double polarizer can block all the scattered light from reaching the camera expect light passed through crystals. The fact that more and more light spots can be observed confirmed that cluster can be transfer into crystals in the supersaturated solution.

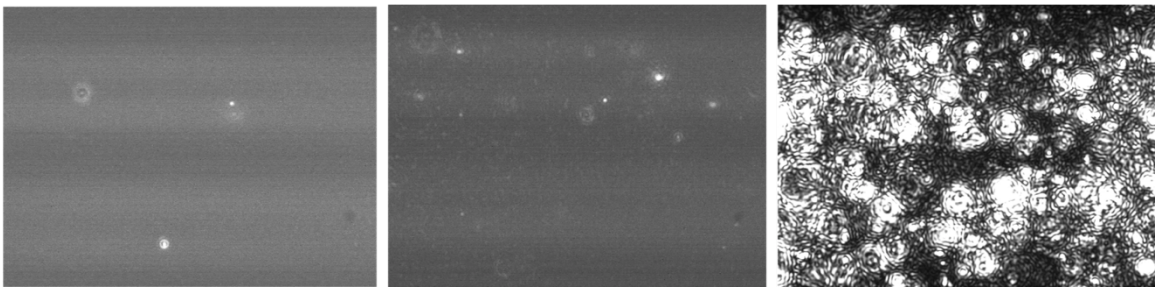

Figure 72. Clusters Observed at different concentration of hematin.

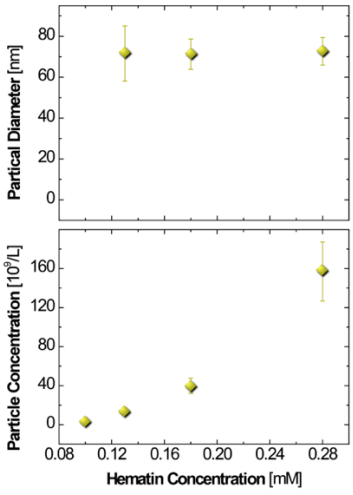

Figure 73. Particle size and density at different hematin concentration.

Nanosite movies were recorded and processed for the assays of hematin solution in the presence of antimalarials. The density and population were reported. The reported size of cluster at all conditions was equivalent. Similar to the DLS results, CQ and MQ displayed a similar density of clusters at pure hematin solution, PY reduced the density and H – ARS largely increased it. To test how the concentration of antimalarials impact the cluster formation, hematin concentration was kept constant at 0.28 mM and increase the amount of antimalarials in the solution. Similarly, CQ and MQ won't affect the cluster behaviors. PY can fully stop the formation at around 4 μM. Those results confirmed the observed spots are likely to be cluster precursors and the number of clusters will directly impact the nucleation time and formation of nanocrystals.

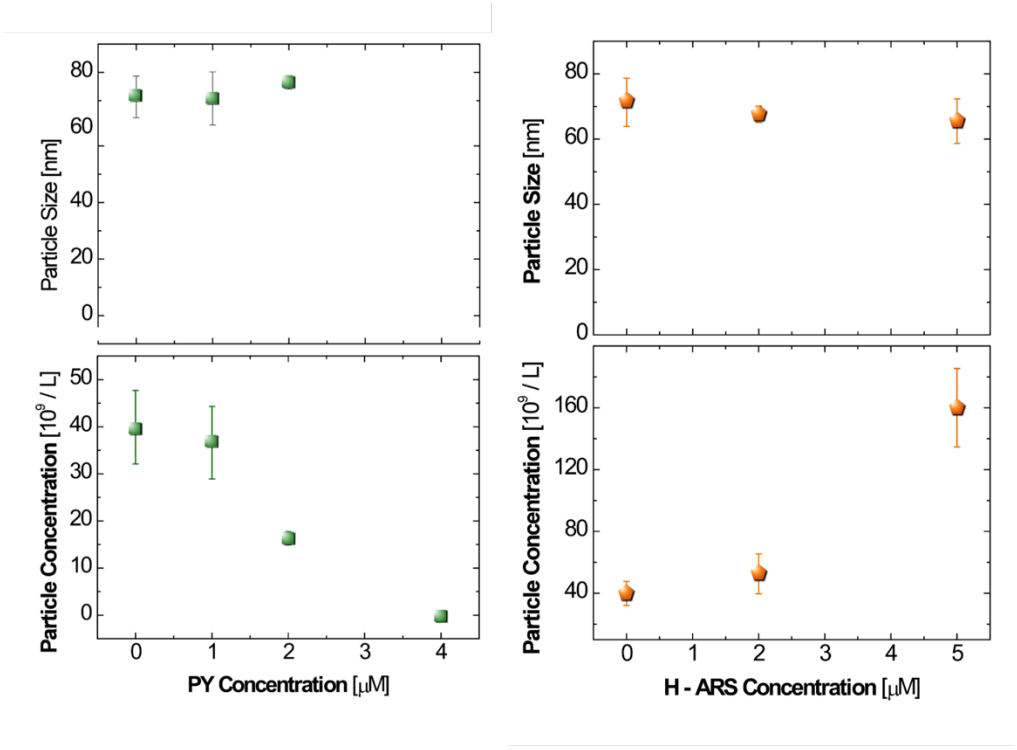

Figure 74. Cluster density varying with PY and H – ARS concentration.

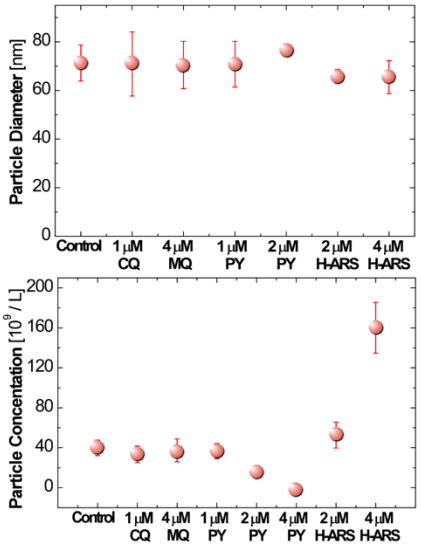

Figure 75. Conclusion of average size and density of particles in the presence of antimalarials.

The observed *d*s are consistent with the diameters of the amorphous aggregates observed by TEM. Both *d* and *N*, the number of aggregates per unit volume, are steady for at least one hour, behaviors that stand in contrast to expectations for domains of classical liquid or solid condensates due to a first-order phase transition,(*193, 194*) whose their nucleation and growth persist and *d* and *N* increase (*195, 196*). In further contradistinction to typical condensed phases, the aggregates size is independent of the hematin concentration. The reversibility of the aggregates is revealed by the concentration dependence of *N*, which declines about 15-fold in response to a two-fold reduction of concentration. The exaggerated response of *N* to reduced concentration indicates that the aggregates are not irreversible agglomerates, whose concentration is diluted in parallel with that of the solute, but rather condensates existing in dynamic equilibrium with the host solution (*197*).

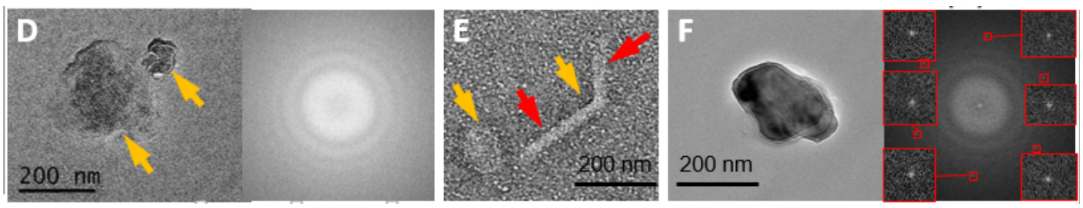

Figure 76. TEM micrograph from a cluster that hosts one or more crystals as certified by the electron diffractogram, which superimposes amorphous and crystalline signatures.

These behaviors of the hematin aggregates cohere with previous observations of mesoscopic solute-rich clusters of olanzapine (*198, 199*) and numerous proteins (*200-203*). We conclude that the hematin aggregates are mesoscopic solute-rich clusters. According to recent models the mesoscopic clusters, they exist owing to the accumulation of transient dimers (*203-205*). The cluster size is determined by the balance between the lifetime of the transient dimers and their rate of outward diffusion from the cluster core and is, hence, independent of the solute concentration and steady in time (*204, 206*). By contrast, the amount of solute captured in the clusters, and the related number of clusters and cluster population volume, increases exponentially with the solute concentration as a consequence of the thermodynamic equilibrium between the clusters and the bulk solution (*204, 206, 207*). The mesoscopic clusters of hematin appear to remarkably well comply with the predictions of this model (*197, 203*).

In further compliance with the model, the addition of CQ, MQ, PY, and H-ARS does not affect the clusters size. These additives, however, invoke disparate responses of the cluster concentration *N*. *N* is indifferent to CQ and MQ; PY enforces strong suppression of cluster formation, whereas H-ARS amplifies *N* four-fold. Remarkably, these responses of

the cluster population to the four additives run parallel to how they suppress of enhance crystal nucleation, coherently with the role of clusters as crystal nucleation sites. Collectively, the TEM observation of cluster-assisted nucleation and the parallel trends of additive activity on the cluster population and crystal nucleation support a mechanism of nucleation control employing additives that enhance or suppress the population of nucleation precursors.

Chapter 9. Nonclassical pathways of cholesterol crystallization thought the attachment of clusters on the surface.

One of the most relevant, yet the least investigated pathological crystal is cholesterol, which is a principle component of gallstones (1-5) and atherosclerosis (6, 7). Prior studies have largely focused on the effects of phospholipids and bile salts on the formation of cholesterol crystals;(8) however, few groups have examined the mechanism(s) of crystallization. To this end, we conducted preliminary studies revealing cholesterol crystal growth occurs by a combination of classical and nonclassical (9) pathways involving the addition of monomer and precursors (i.e. clusters), respectively. In situ AFM confirmed the addition of clusters while dynamic light scattering (DLS) indicated their presence over a range of temperatures and solute concentrations. It was found that growth at high supersaturation leads to layered surfaces populated with step bunches and double steps that grow at reduced rates. At low supersaturation, we observe highly unusual step advancement mediated by the presence of protrusions. Collectively, our preliminary data indicates that cholesterol grows by pathways that are distinct compared with other pathological crystals.

We develop an improved understanding of cholesterol crystallization with an emphasis on the assembly and role of clusters (i.e. nonclassical pathways). This research will predominantly employ in situ AFM to elucidate layer generation and spreading at physiologically-relevant conditions. AFM has proven to be a powerful technique for probing growth dynamics and molecular interactions at crystal surfaces with near molecular resolution (*208-212*). Once establishing growth mechanisms over a range of

conditions, we will begin to identify potential inhibitors (i.e. organics with similar structures as cholesterol). The selection of molecules will be guided by heuristics established in our group for a variety of organic crystals, thus enabling our detailed investigation into the processes of cholesterol crystal growth inhibition.

Previous studies forced on investigating the role of hepatic secretion of biliary cholesterol, phospholipids and bile salts that may govern the crucial steps of formation of gallbladder. Those results unveiled pathways to modify or stop the formation of cholesterol crystals from controlling the precipitation, growth or agglomeration. However, Difficulties built in the nature of cholesterol crystallization build a wall that barricade a deep understanding of molecular mechanisms. The extreme fast nucleation and growth rate outrun the rate that we can catch. In recent studies, we establish a system mimicking the environment in where cholesterol crystal forms while regulating the rate of crystal growth within a rage that can be monitored by atomic force microscopy. The result revealed that cholesterol crystallization follows a novel nonclassical pathway in which the clusters were involved.

9.1 Gallstones and cholesterol crystals

Approximately twenty percent of adults have gallstones making gallstone disease is one of the most common biliary tract diseases caused by a combination of genetic and environmental factors. Gallstones occur when the chemical constituents of bile become imbalance. Precipitation of solid cholesterol crystals from supersaturated bile plays an essential role in gallstone formation. Gallstones can cause various problems: biliary colic/cholecystitis; Jaundice; ascending cholangitis; pancreatitis; Bouveret's syndrome

and gallstone ileus and Gallbladder cancer. The most common treatments for gallstone disease are drug dissolution therapy and open surgery. The understanding of the mechanism behind cholesterol crystallization will provide insights for designing more effective therapeutic drugs to prevent or remove gallstones.

Cholesterol stones are composed of more than 80% cholesterol. They often contain alternating layers of cholesterol crystals and mucin glycoproteins. Some calcium salts and bile pigments can also be included in the stone. The addition of the proteins improves the strength of cholesterol stones are pure cholesterol crystals are soft (*213*).

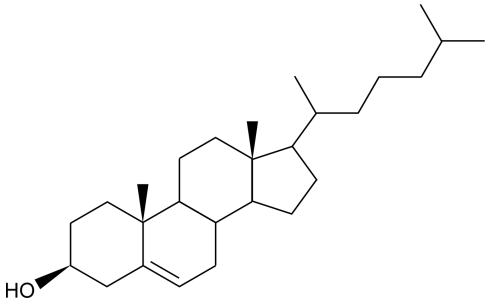

Figure 77. Chemical structure of cholesterol.

The formation of gallstones was initialized when the amount of cholesterol carried by lipoprotein exceeded the limitation. Cholesterol usually nucleates at the wall of blood vessel and those small crystals further accelerated the crystallization process. When a galls tone causes blockage of cystic duct, it leads to severe episodes of pain (*214*). The plaque of cholesterol crystals can also lead to heart attack or sudden cardiac death, accompanied with stroke, chest pain, leg pain, leg cramps, sudden numbness, weakness and dizziness.

9.2 Cholesterol Structure

Cholesterol crystals have several polymorphs depending on the growth solution. The two most common ones are cholesterol monohydrate and anhydrous cholesterol. Cholesterol monohydrate crystals have bilayer structure with space group P1. The unit cell crystallographic dimensions are as follows: a =12.39 Å, b = 12.41 Å, c = 34.36 Å, α = 91.9°, β = 98.1°, and γ = 100.8 ° (*215*). The largest plate face is the (001) face.

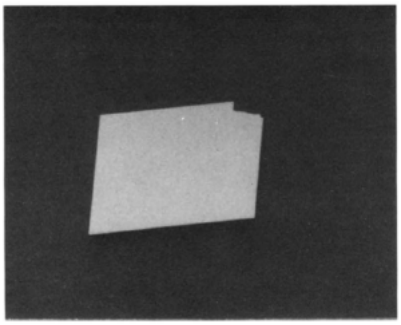

Figure 78. Image of Cholesterol monohydrate crystal (*216*).

Anhydrous cholesterol crystals are triclinic with a space group of P1. cholesterol monohydrate. The unit cell dimensions are a = 14.17 Å, b = 34.21 Å, c =10.48 Å, α = 94.6°, β = 90.7°, and γ = 96.3° (*215*). The observed morphology is clearly distinct from cholesterol monohydrate as needlelike crystals.

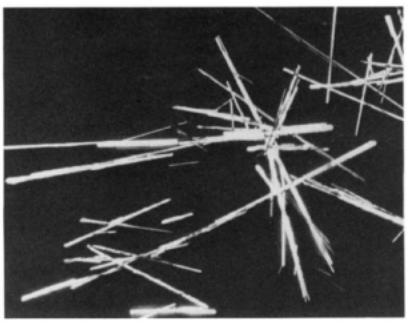

Figure 79. Image of anhydrous cholesterol crystal.

The final polymorphs largely depend on the accessibility of water. In previous studies, we noticed that crystals synthesized from pure organic solvents are appeared to the anhydrous form. When water was added to the system, the final crystal form is monohydrate. Interestingly, in the butanol with 3% water solvent, needle like anhydrous cholesterol crystal was first observed in the solution and later transform into monohydrate cholesterol crystal. The assumption that anhydrous polymorph always generated first in the solution was partially proved in Nam-Joon's work. They tracked the nucleation of cholesterol on the lipid layers and imaged with fast scan camera. Images showed that needle like crystals were generated on the surface first, then the edge of those needles begin to partial dissolve and finally transformed to the rectangular shape (*217*). The transformation happened within 20s.

9.3 Syntheses of cholesterol crystals.

Cholesterol crystallization follows the basic principle that can be controlled by adjusting the supersaturation. As cholesterol crystal grow extremely fast, a method of slow evaporation over 2 weeks from solutions of 95% ethanol and 5% distilled water has been utilized. The crystals are originally transparent or clear, but after a few hours of exposure to air a transformation to opaque crystals transpires due to dehydration of the crystalline structure. As the monohydrate cholesterol is the most common crystals found from gallstones, crystals are stored in the solution to maintain the morphology before the experiments performed later.

Cholesterol is small organic small molecules have extreme high solubility in organic solvent while almost insoluble in water solution. However, water in the system plays an

essential for the formation of monohydrate polymorph. To set a controller growing system can be plant in the AFM study while mimic the environment inside human blood vessel, Megan Ketchum measured the extinction coefficients and solubilities in various environments. Those measurements guiled the choice of the solution in the later experiments.

Table 5

Extinction coefficients of cholesterols in various solvents.

Solvent	ε [$mM^{-1}cm^{-1}$]	λ [nm]
Methanol	4.11 ± 0.08	201
Ethanol	3.36 ± 0.06	202
Ethanol + 5% H_2O	4.10 ± 0.04	202
Ethanol + 7.5% H_2O	4.6 ± 0.2	201
Ethanol + 10% H_2O	5.10 ± 0.09	201
Butanol	2.87 ± 0.05	204
Butanol + 2.5% H_2O	3.03 ± 0.05	204
Butanol + 5% H_2O	3.56 ± 0.08	203
Butanol + 7.5% H_2O	3.81 ± 0.07	203
Hexanol	2.30 ± 0.04	205
Hexanol + 2.5% H_2O	3.54 ± 0.08	204
Hexanol + 5% H_2O	2.73 ± 0.05	205
Octanol	3.24 ± 0.06	202

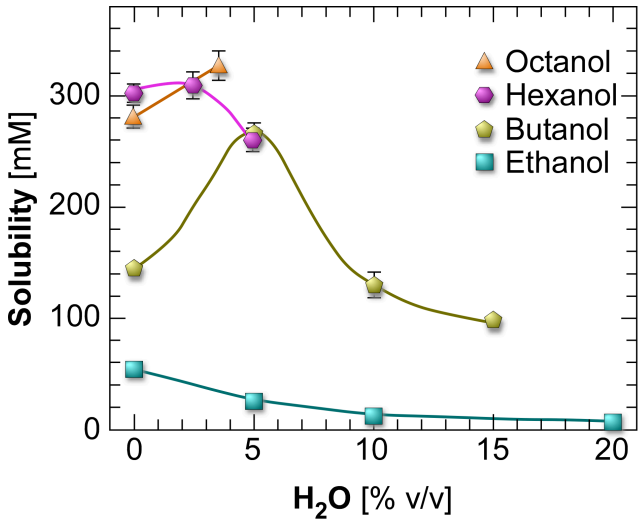

Figure 80. Solubilities of cholesterol in different solvents at 25 Celsius.

According to all the data, we aimed to select ethanol as the candidate for cholesterol growth in the AFM studies as the growth rate can be readily controlled through the percentage of water content. The PH of the mixture is feasible to be adjusted by changing the aqueous phase to a desired buffer. Crystals can be generated through cooling a supersaturated solution slowly or reducing the amount of solvent by evaporating. Both methods achieved to create a small step of supersaturation over long period of time. Monohydrate crystals were produced with an average dimension of 300 nm in length.

9.3 Decipher the cholesterol crystallization mechanism

Studies were mainly forced on the function of phospholipids in the formation of gallbladder (*8, 218-220*). Cholesterol molecules are usually highlighted with special dyes to track how cholesterol molecules assembly from bulk solution into crystal forms (*221*). Studies displayed both the heterogeneous nucleation and crystal growth at the surface of phospholipids at the microscopic level. Recent studies in Jennifer (*222*) illustrated the

dissolution of monohydrate cholesterol crystal in the presence of bile salts. However, the growth mechanism of cholesterol crystallization at crystal interface is unknown.

The challenge landed in monitoring the growth mechanism is both from the complexity of the growing system in which cholesterol displayed a huge discrepancy in solubility and the nature of cholesterol crystallization that the fact growth rate beyond the tracking ability of most techniques. To solve those problems, we tested various solvents and selected the water/ethanol mixture as the candidate for controlling the growth rate. Besides, we implanted the fast scan AFM that can track the movement of steps with 20 Hz. During the scanning, the temperature was controlled to 37 Celsius and the inlet solution must be kept at 39 ~ 45 Celsius to avoid the participate of cholesterol crystals.

The (001) surface was monitored with supply of cholesterol water/ethanol solution that contains 35% water. Reducing the amount of water with the same supersaturation will largely increase the growth rate. Around 20%, the generation of dislocation and spread can be observed in micrometer scare that can be monitored by optical microscopy (suggested solution for microfluid device studies in the future). 35% water/ethanol solution provides a feasible growth rate among the desired supersaturation ratios.

9.3.1 Polymorphs and dissolution

The AFM images revealed that the top layers of the crystal surface were dissolving even though the concentration beyond the solubility, measured for

monohydrate crystal at this temperature. In the meantime, the bottom layer of cholesterol crystal can grow. We proposed that the monohydrate cholesterol crystal can readily transform to the anhydrous form as the surface is exposed to the air during the preparation. The PXDR indicted that monohydrate crystal can fully transform to the anhydrous form and the solubility of anhydrous crystal appears to have higher solubility in the ethanol solution. The data indicate that the layer on the top may either dilute back to the bulk solution or go through a morphology transformation in the solution. The solubility difference is much smaller in water/ethanol mixture than the pure ethanol solution. The case suggested the existence of polymorph exchange when water is present.

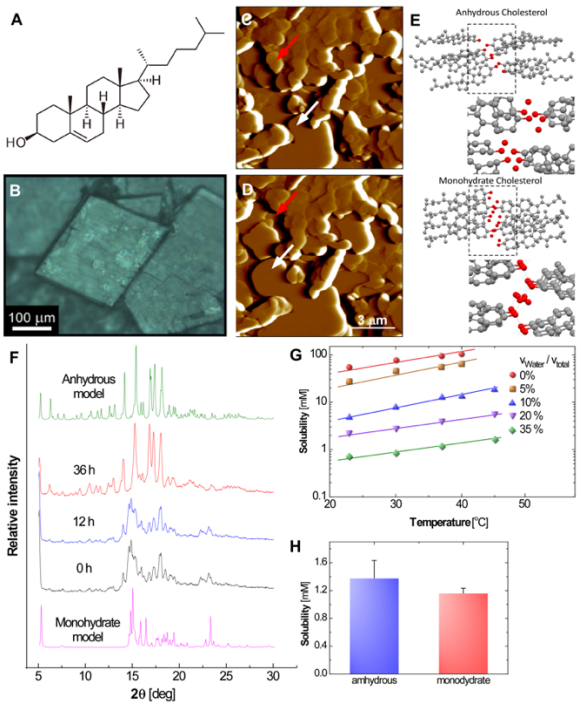

Figure 81. Demonstration of cholesterol crystals. Morphologies; Dissolving while growing; solubility test.

9.3.2 Deposition of particles on the surface

Nearly one layer or double layer steps are appeared after the dissolution of top layers. Those steps are moving with a relevant slower step rate for a very short period of time and then begin to accelerate in several seconds. In the meantime, we begin to observe that particles are dropping on the terrace. Those particles displayed a size ranged from 40 nm to 100 nm in height. The indentation measurement suggested that those particles are solids though it cannot exclude the possibility that those particles can transform from condensed liquid phase to the solid phase on the surface.

Particles dropped on the terrace were merely observed when the contact mode, an AFM select that interferences much more with the scanned area than the tapping mode we usually applied. The case suggested that those particles are likely coming from the solution phase. In the contact mode, the tip was moving around the surface and removing all the coming particles. One evidence is that grown particles were observed outside the scanning area. Interesting, the particle can change the pathway of growth pathways of (001) surface of cholesterol crystal discussed later. Cholesterol followed a classical pathway in the absence of deposits that layers were growing from step advancement. The mechanism is likely to the dislocation pathways though few dislocations are recorded duo to the scale.

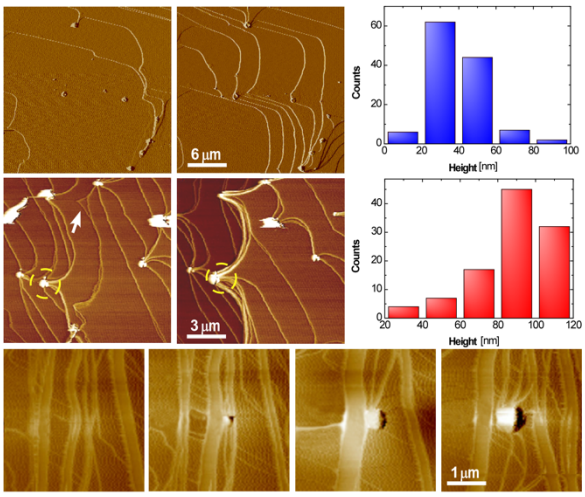

Figure 82. Particles initially dropped on the terrace with the size distribution. Particles may grow large and multiple layers bridges were forming between two deposits.

9.3.2 Characterization of clusters

We concluded that particles dropped on the surface and guide the crystal to a new pathway of growth are likely coming from solution phase. To confirm the hypotheses and characterize particles in the solution, DLS and nanosite offered important information for particles in the solution. As the technique was mentioned in the previous chapter, the detailed introduction will be skipped.

DLS data displayed a constant correlation function reached the maximum amplitude at the beginning of experiment that suggested that formation of clusters for cholesterol is extremely fast process. Like the hematin experiments, the correlation functions are similar for supersaturated solution and under supersaturated solution that gave the size of cluster 80nm. The correlation function remains unchanged after leaving in the constant departure for 3h. No evaporation was considered as the contained was

well sealed. Unlike the hematin solution, cholesterol cluster can be detected by DLS method. This offers an opportunity to confirm whether the particles are clusters with a test shows how size of particles depend on the temperature. The measurement showed that the size of particles is reducing as temperature increase. Those features fit the properties of precreation intermedium, cluster. The Nanosite video feedback the similar result and hence we proposed that clusters in the solution may vary the growth mechanism both from the nucleation part but also from surface growth viewpoint.

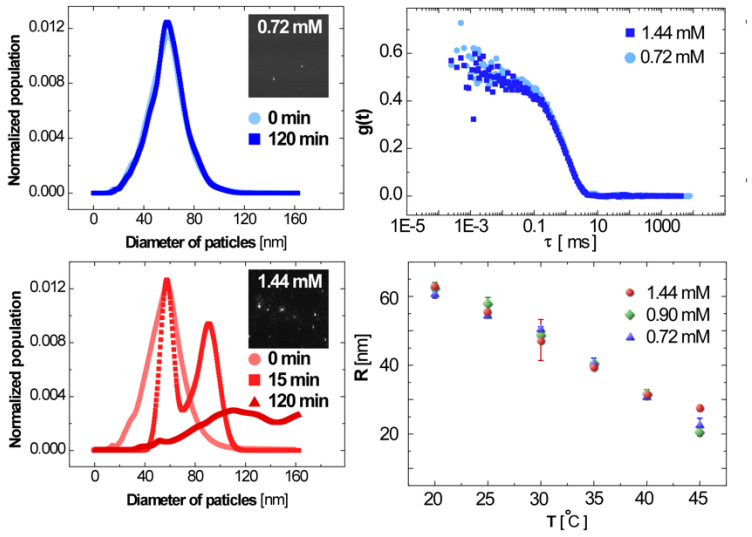

Figure 83. DLS and Nanosite investigation of clusters in the cholesterol solution.

9.3.3 Nonclassical growth lead by deposits on the surface.

Collected data indicted cholesterol follows a really complex pathway. The AFM studies indicated that crystal follows the classical pathway without deposits. Several consequences lead to a special pathway after particles deposited on the surface. The first thing we noticed layers are accelerated around the deposits and curved multiple step are formed. This phenomena is similar to the reversed process of the inhibited dissolution

buy dropped particles described in Chernov's work (*64*). Yet it holds a brand-new mechanism for us to explore. The acceleration of steps may be explained by the hypothesis that the deposited particles with a different morphology lead to the strain at the contact point and the strain drives the dilution of those misaligned molecules. This process created a regime of high concentration that speed up the steps approaching those deposits. However, the hypothesis cannot explain the growth of those deposits we saw in the AFM studies. Some of deposits on the surface can continue growing in to a huge extrusion with a high range from a hundred nanometer to one micrometer. In large scale, those protrusions also can connect steps with curved stage. The mechanism remains unknown.

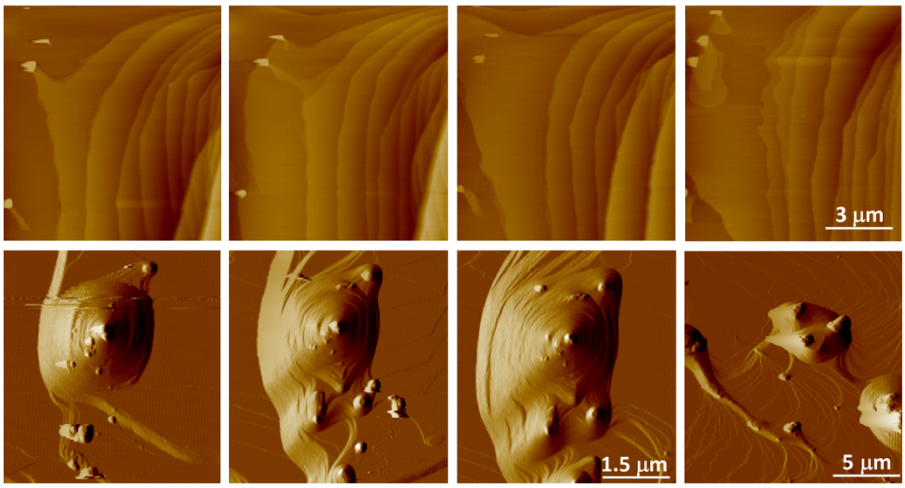

Figure 84. Cluster behaviors on the surface. They attract step; generate new steps; construct curve bridges; grow into mountains.

9.3.4 Characterize the crystal growth and future work

Crystal growth is characterized by growth rate. As no 2D nuclei or clear dislocation center was observed. The detailed mechanism required more information. The step

growth rate with different step separation also performed to check the surface diffusion. We also noticed the temperature may affect the level of curvature of steps. As the large discrepancy landed in the various solvents, does the clusters still remain same features. More work will be done to answer all those questions.

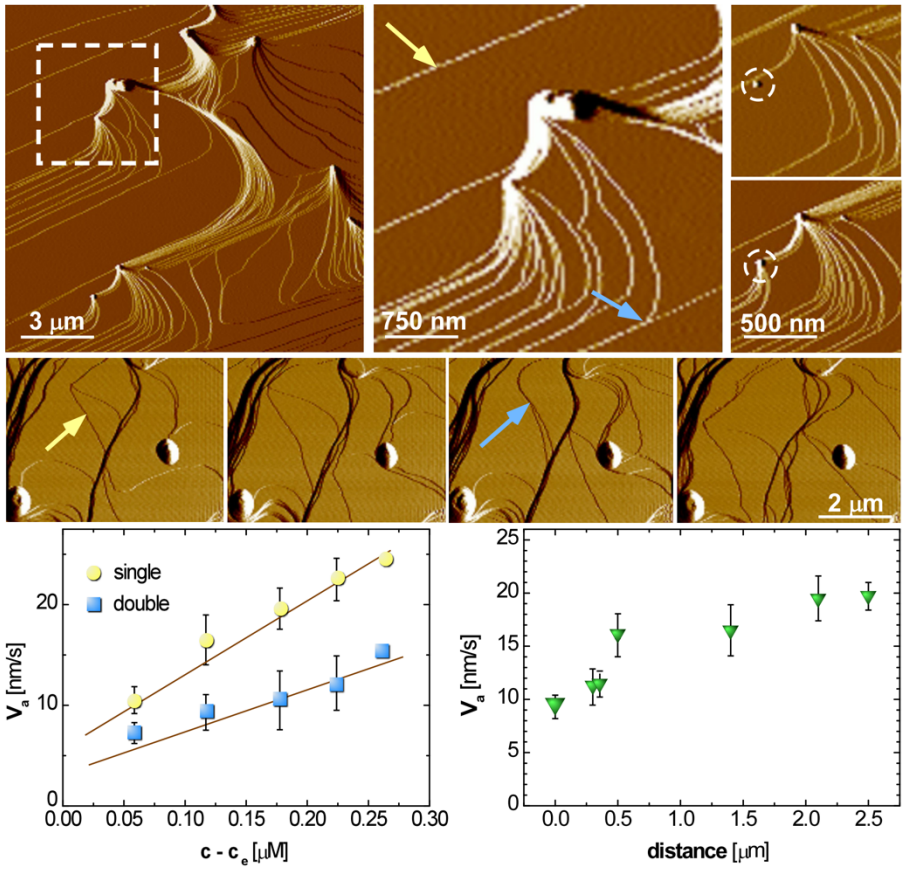

Figure 85. Step advancement measurement.

Conclusions

Crystallization is one of the most important process that reveals the mixture of complexity and regularity of rules that govern the operation of our daily lives. In the previous study, from studying the hematin crystallization existed in the malaria parasite, we illustrated how modifiers can change the pathway of crystal growth and further pushed the phenomenon to a common theory that may apply to other crystallization systems. We discovered the dual mechanism of new class antimalarial drugs, artemisinin, that the drug can react with the free heme to produce a new compound that can attack both the crystallization process and the crucial protein sequence for malarial parasite to multiply. Besides, it is so interesting and excising if we can develop a theory that can explain what's really going on between the nucleation formation and the existed intermediates composed of monomer and enhance to control the nucleation process. Besides, the cholesterol crystallization remains a huge opening for the future study. The special interaction between deposits and steps may lead to a series of new hypotheses. I am looking forward to answer the mystery interaction that can drag close steps to the rounds deposits; to test how the mechanism related to inhibition of cholesterol crystallization and cure of relative diseases; to eventually understand the cholesterol crystallization in the real human system, which is a way more complex system involving the crystallization but also the incorporation of salts.

Science is a beauty that expands the broader of our freedom.

References

1. P. Portincasa, E. Molina-Molina, G. Garruti, D. Q. H. Wang, Critical Care Aspects of Gallstone Disease. *J Crit Care Med (Targu Mures)* **5**, 6-18 (2019).
2. S. M. Strasberg, The pathogenesis of cholesterol gallstones—A review. *Journal of Gastrointestinal Surgery* **2**, 109-125 (1998).
3. A. Sedaghat, S. M. Grundy, Cholesterol crystals and the formation of cholesterol gallstones. *N Engl J Med* **302**, 1274-1277 (1980).
4. R. E. Glasgow, M. Cho, M. M. Hutter, S. J. Mulvihill, The spectrum and cost of complicated gallstone disease in California. *Arch Surg* **135**, 1021-1025; discussion 1025-1027 (2000).
5. G. Sanders, A. N. Kingsnorth, Gallstones. *BMJ* **335**, 295-299 (2007).
6. A. Janoudi, F. E. Shamoun, J. K. Kalavakunta, G. S. Abela, Cholesterol crystal induced arterial inflammation and destabilization of atherosclerotic plaque. *European Heart Journal* **37**, 1959-1967 (2016).
7. S. M. Nidorf, A. Fiolet, G. S. Abela, Viewing atherosclerosis through a crystal lens: How the evolving structure of cholesterol crystals in atherosclerotic plaque alters its stability. *Journal of Clinical Lipidology* **14**, 619-630 (2020).
8. M. R. Elkins, I. V. Sergeyev, M. Hong, Determining Cholesterol Binding to Membrane Proteins by Cholesterol 13C Labeling in Yeast and Dynamic Nuclear Polarization NMR. *Journal of the American Chemical Society* **140**, 15437-15449 (2018).
9. James J. De Yoreo, Pupa U. P. A. Gilbert, Nico A. J. M. Sommerdijk, R. Lee Penn,Stephen Whitelam, Derk Joester, Hengzhong Zhang, Jeffrey

D.Rimer,Alexandra Navrotsky, Jillian F. Banfield, Adam F. Wallace, F. Marc Michel,Fiona C. Meldrum, Helmut Cölfen, Patricia M. Dove., Crystallization by particle attachment in synthetic, biogenic, and geologic environments. *Science* 349, 498-+ (2015).

10. Monika Warzecha 1, Lakshmanji Verma, Blair F. Johnston 1,3, Jeremy C. Palmer, Alastair J. Florence and Peter G. Vekilov ., Olanzapine crystal symmetry originates in preformed centrosymmetric solute dimers. *Nature Chemistry* **12**, 914-920 (2020).
11. Marie Albéric, Luca Bertinetti, Zhaoyong Zou, Peter Fratzl, Wouter Habraken, and Yael Politi., The Crystallization of Amorphous Calcium Carbonate is Kinetically Governed by Ion Impurities and Water. *Advanced Science* **5**, 1701000 (2018).
12. Sanja Sviben1, Assaf Gal1, Matthew A. Hood, Luca Bertinetti, Yael Politi, Mathieu Bennet, Praveen Krishnamoorthy, Andreas Schertel, Richard Wirth, Andrea Sorrentino, Eva Pereiro, Damien Faivre, Andre´Scheffel, A vacuole-like compartment concentrates a disordered calcium phase in a key coccolithophorid alga. *Nature Communications* **7**, 11228 (2016).
13. M. H. Nielsen, S. Aloni, J. J. De Yoreo, In situ TEM imaging of $CaCO_3$ nucleation reveals coexistence of direct and indirect pathways. *Science* **345**, 1158-1162 (2014).
14. J. D. Rodriguez-Blanco, S. Shaw, P. Bots, T. Roncal-Herrero, L. G. Benning, The role of pH and Mg on the stability and crystallization of amorphous calcium carbonate. *Journal of Alloys and Compounds* **536**, S477-S479 (2012).

15. W. D. Bischoff, Dissolution Enthalpies of Magnesian Calcites. *Aquatic Geochemistry* **4**, 321-336 (1998).

16. Dongsheng Li, Michael H. Nielsen, Jonathan R. I. Lee, Cathrine Frandsen, Jillian F. Banfield, James J. De Yoreo, Direction-Specific Interactions Control Crystal Growth by Oriented Attachment. *Science* **336**, 1014 (2012).

17. A. I. Lupulescu, J. D. Rimer, In Situ Imaging of Silicalite-1 Surface Growth Reveals the Mechanism of Crystallization. *Science* **344**, 729 (2014).

18. Dongsheng Li, Michael H. Nielsen, Jonathan R. I. Lee, Cathrine Frandsen, Jillian F. Banfield, James J. De Yoreo, Modulation of calcium oxalate dihydrate growth by selective crystal-face binding of phosphorylated osteopontin and polyaspartate peptide showing occlusion by sectoral (compositional) zoning. *J Biol Chem* **284**, 23491-23501 (2009).

19. Duoduo Liang, Lana R. A. Follens, Alexander Aerts, Johan A.Martens, Gustaaf Van Tendeloo, Christine E. A. Kirschhock, TEM Observation of Aggregation Steps in Room-Temperature Silicalite-1 Zeolite Formation. *The Journal of Physical Chemistry C* **111**, 14283-14285 (2007).

20. James J. De Yoreo, Pupa U. P. A. Gilbert, Nico A. J. M. Sommerdijk, R. Lee Penn,Stephen Whitelam, Derk Joester, Hengzhong Zhang, Jeffrey D. Rimer,Alexandra Navrotsky, Jillian F. Banfield, Adam F. Wallace, F. Marc Michel,Fiona C. Meldrum, Helmut Cölfen, Patricia M. Dove., Crystallization by particle attachment in synthetic, biogenic, and geologic environments. *Science* **349**, aaa6760 (2015).

21. H. M. Van Horn, The crystallization of white dwarf stars. *Nature Astronomy* **3**, 129-130 (2019).

22. N. Reznikov, J. A. M. Steele, P. Fratzl, M. M. Stevens, A materials science vision of extracellular matrix mineralization. *Nature Reviews Materials* **1**, 16041 (2016).

23. J. J. De Yoreo, P. G. Vekilov, in *Biomineralization*. (2003), vol. 54, pp. 57-93.

24. K. N. Olafson, R. Li, B. G. Alamani, J. D. Rimer, Engineering Crystal Modifiers: Bridging Classical and Nonclassical Crystallization. *Chemistry of Materials* **28**, 8453-8465 (2016).

25. Ana Paula Badan Ribeiro&Monise Helen Masuchi&Eriksen Koj Miyasaki, Maria Aliciane Fontenele Domingues, Valter Luís Zuliani Stroppa, Glazieli Marangoni de Oliveira, Theo Guenter Kieckbusch, Crystallization modifiers in lipid systems. *J Food Sci Technol* **52**, 3925-3946 (2015).

26. S. N. Black, A. Hutchinson, R. J. Davey, Concerning the selection of crystallization modifiers for non-hydrogen bonded systems: the case of benzophenone. *CrystEngComm* **23**, 1281-1293 (2021).

27. Spencer D. Schaber, Dimitrios I. Gerogiorgis†, Rohit Ramachandran, James M. B. Evans, Paul I. Barton, Bernhardt L. Trout, Economic Analysis of Integrated Continuous and Batch Pharmaceutical Manufacturing: A Case Study. *Industrial & Engineering Chemistry Research* **50**, 10083-10092 (2011).

28. M. A. Ketchum, K. N. Olafson, E. V. Petrova, J. D. Rimer, P. G. Vekilov, Hematin crystallization from aqueous and organic solvents. *The Journal of Chemical Physics* **139**, 121911 (2013).

29. Jihae Chung, Ignacio Granja, Michael G. Taylor, Giannis Mpourmpakis, John R. Asplin, Jeffrey D. Rimer, Molecular modifiers reveal a mechanism of pathological crystal growth inhibition. *Nature* **536**, 446 (2016).

30. A. McPherson, J. A. Gavira, Introduction to protein crystallization. *Acta Crystallogr F Struct Biol Commun* **70**, 2-20 (2014).

31. A. Baronnet, Natural crystallization and relevant crystal growth experiments. *Progress in Crystal Growth and Characterization of Materials* **26**, 1-24 (1993).

32. I. Russo Krauss, A. Merlino, A. Vergara, F. Sica, An overview of biological macromolecule crystallization. *Int J Mol Sci* **14**, 11643-11691 (2013).

33. B. Huneau, STRAIN-INDUCED CRYSTALLIZATION OF NATURAL RUBBER: A REVIEW OF X-RAY DIFFRACTION INVESTIGATIONS. *Rubber Chemistry and Technology* **84**, 425-452 (2011).

34. M. Shepelenko, Y. Feldman, L. Leiserowitz, L. Kronik, Order and Disorder in Calcium Oxalate Monohydrate: Insights from First-Principles Calculations. *Crystal Growth & Design* **20**, 858-865 (2020).

35. L. H. Miller, H. C. Ackerman, X.-z. Su, T. E. Wellems, Malaria biology and disease pathogenesis: insights for new treatments. *Nature Medicine* **19**, 156-167 (2013).

36. DanielE.Goldberg, AndrewF.G.Slater, RonaldBeavis, BrianChait, AnthonyCerami, GraemeB.Henderson, Hemoglobin Degradation in the Human Malaria Pathogen Plasmodium falciparum: A Catabolic Pathway Initiated by a Specific Aspartic Protease. *J. Exp. Med.* **173**, 961-961 (1991).

37. B. Greenwood, Progress in malaria control in endemic areas. *Travel Med Infect Dis* **6**, 173-176 (2008).

38. A. V. S. Hill, Vaccines against malaria. *Philosophical transactions of the Royal Society of London. Series B, Biological sciences* **366**, 2806-2814 (2011).

39. D. E. Goldberg, A. F. Slater, A. Cerami, G. B. Henderson, Hemoglobin degradation in the malaria parasite Plasmodium falciparum: an ordered process in a unique organelle. *Proceedings of the National Academy of Sciences* **87**, 2931-2935 (1990).

40. A. U. Orjih, H. S. Banyal, R. Chevli, C. D. Fitch, Hemin lyses malaria parasites. *Science* **214**, 667-669 (1981).

41. R. G. Ridley, Medical need, scientific opportunity and the drive for antimalarial drugs. *Nature* **415**, 686-693 (2002).

42. A. Laveran, Un nouveau parasite trouve dans le sang des malade atteints de fievre palustre. Origine parasitaire des accidents de l'impaludisme. *Bull Mem Soc Med Hop Paris* **7**, 158–164 (1880).

43. R. Ross, On some Peculiar Pigmented Cells Found in Two Mosquitos Fed on Malarial Blood. *British Medical Journal* **2**, 1786-1788 (1897).

44. R. Talbor, *Pyretologia, A Rational Account of the Causes and Cure of the Agues*. (London, 1672).

45. T. J. Egan, Haemozoin formation. *Molecular and Biochemical Parasitology* **157**, 127-136 (2008).

46. Juliana B. R. Correˆa Soares, Diego Menezes, Marcos A. Vannier-Santos, Antonio Ferreira-Pereira, Giulliana T. Almeida, Thiago M. Venancio, Sergio

Verjovski-Almeida, Vincent K. Zishiri, David Kuter, Roger Hunter, Timothy J. Egan, Marcus F. Oliveira. Interference with Hemozoin Formation Represents an Important Mechanism of Schistosomicidal Action of Antimalarial Quinoline Methanols. *Plos Neglect.* Trop. Dis. 3, (2009).

47. D. J. Sullivan, I. Y. Gluzman, D. G. Russell, D. E. Goldberg, On the molecular mechanism of chloroquine's antimalarial action. *Proceedings of the National Academy of Sciences* **93**, 11865-11870 (1996).

48. A. P. Gorka, A. de Dios, P. D. Roepe, Quinoline Drug–Heme Interactions and Implications for Antimalarial Cytostatic versus Cytocidal Activities. *Journal of Medicinal Chemistry* **56**, 5231-5246 (2013).

49. A. F. Cowman, J. Healer, D. Marapana, K. Marsh, Malaria: Biology and Disease. *Cell* **167**, 610-624 (2018).

50. S. Kumar, U. Bandyopadhyay, Free Heme Toxicity and Its Detoxification Systems in Human. *Toxicol. Lett.* **157**, 175-175 (2005).

51. Jonathan M. Be´lisle, Santiago Costantino, Mara L. Leimanis,y Marie-Jose´e Bellemare,z D. Scott Bohle,z Elias Georges, y Paul W. Wiseman, Sensitive detection of malaria infection by third harmonic generation imaging. *Biophys J* **94**, L26-28 (2008).

52. B. Gligorijevic, T. Bennett, R. McAllister, J. S. Urbach, P. D. Roepe, Spinning Disk Confocal Microscopy of Live, Intraerythrocytic Malarial Parasites. 2. Altered Vacuolar Volume Regulation in Drug Resistant Malaria. *Biochemistry* **45**, 12411-12411 (2006).

53. Jigang Wang, Chong-Jing Zhang, Wan Ni Chia, Cheryl C.Y. Loh, Zhengjun Li, Yew Mun Lee, Yingke He, Li-Xia Yuan, Teck Kwang Lim, Min Liu3, Chin Xia Liew, Yan Quan Lee, Jianbin Zhang, Nianci Lu, Chwee Teck Lim, Zi-Chun Hua, Bin Liu, Han-Ming Shen, Kevin S.W. Tan & Qingsong Lin, Haem-activated promiscuous targeting of artemisinin in Plasmodium falciparum. *Nature Communications* **6**, 10111-10111 (2015).

54. John M. PISCIOTTA, Isabelle COPPENS, Abhai K. TRIPATHI, Peter F. SCHOLL, Joel SHUMAN, Sunil BAJAD, Vladimir SHULAEV, David J. SULLIVAN, JR., The Role of Neutral Lipid Nanospheres in Plasmodium falciparum Haem Crystallization. *Biochem. J.* **402**, 197-197 (2007).

55. M. A. Ketchum, K. N. Olafson, E. V. Petrova, J. D. Rimer, P. G. Vekilov, Hematin crystallization from aqueous and organic solvents. *J Chem Phys* **139**, 121911 (2013).

56. K. N. Olafson, R. J. Clark, P. G. Vekilov, J. C. Palmer, J. D. Rimer, Structuring of Organic Solvents at Solid Interfaces and Ramifications for Antimalarial Adsorption on β-Hematin Crystals. *ACS Applied Materials & Interfaces* **10**, 29288-29298 (2018).

57. S. Pagola, P. W. Stephens, D. S. Bohle, A. D. Kosar, S. K. Madsen, The structure of malaria pigment β-haematin. *Nature* **404**, 307 (2000).

58. K. N. Olafson, M. A. Ketchum, J. D. Rimer, P. G. Vekilov, Mechanisms of hematin crystallization and inhibition by the antimalarial drug chloroquine. *Proc Natl Acad Sci U S A* **112**, 4946-4951 (2015).

59. Timothy J. Egan, Jeff Y-J. Chen, Katherine A. de Villiers, Tebogo E. Mabotha, Kevin J. Naidoo, Kanyile K. Ncokazi, Steven J. LangfordDon, Mc Naughton, Shveta Pandiancherri, Bayden R. Wood, Hemozoin (β-Hematin) Biomineralization Occurs by Self-Assembly near the Lipid/Water Interface. *FEBS Lett.* **580**, 5105-5105 (2006).

60. K. N. Olafson, J. D. Rimer, P. G. Vekilov, Growth of Large Hematin Crystals in Biomimetic Solutions. *Cryst Growth Des* **14**, 2123-2127 (2014).

61. M. A. Ketchum, K. N. Olafson, E. V. Petrova, J. D. Rimer, P. G. Vekilov, Hematin crystallization from aqueous and organic solvents. *The Journal of Chemical Physics* **139**, 121911 (2013).

62. K. N. Olafson, M. A. Ketchum, J. D. Rimer, P. G. Vekilov, Mechanisms of hematin crystallization and inhibition by the antimalarial drug chloroquine. *Proceedings of the National Academy of Sciences* **112**, 4946-4951 (2015).

63. M. Krugliak, J. Zhang, H. Ginsburg, Intraerythrocytic Plasmodium falciparum Utilizes Only a Fraction of the Amino Acids Derived from the Digestion of Host Cell Cytosol for the Biosynthesis of Its Proteins. *Mol. Biochem. Parasitol.* **119**, 249-249 (2002).

64. N. A. Booth, A. A. Chernov, P. G. Vekilov, Step bunching in potassium dihydrogen phosphate crystal growth: Phenomenology. *Journal of Materials Research* **17**, 2059-2065 (2002).

65. P. G. Vekilov, J. D. Rimer, K. N. Olafson, M. A. Ketchum, Lipid or aqueous medium for hematin crystallization? *CrystEngComm* **17**, 7790-7800 (2015).

66. I. Weissbuch, L. Leiserowitz, Interplay Between Malaria, Crystalline Hemozoin Formation, and Antimalarial Drug Action and Design. *Chemical Reviews* **108**, 4899-4914 (2008).

67. M. A. Ketchum, K. N. Olafson, E. V. Petrova, J. D. Rimer, P. G. Vekilov, Hematin crystallization from aqueous and organic solvents. *The Journal of Chemical Physics* **139**, 121911-121911 (2013).

68. M. A. Ketchum, A. M. Lee, P. G. Vekilov, J. D. Rimer, Biomimetic Assay for Hematin Crystallization Inhibitors: A New Platform To Screen Antimalarial Drugs. *Crystal Growth & Design* **17**, 197-206 (2017).

69. E. G. Tse, M. Korsik, M. H. Todd, The past, present and future of anti-malarial medicines. *Malaria Journal* **18**, 93 (2019).

70. S. A. Dugger, A. Platt, D. B. Goldstein, Drug development in the era of precision medicine. *Nature Reviews Drug Discovery* **17**, 183-196 (2018).

71. Inna Solomonov, Maria Osipova, Yishay Feldman, Carsten Baehtz, Kristian Kjaer, Ian K. Robinson, Grant T. Webster, Don McNaughton, Bayden R. Wood, Isabelle Weissbuch, Leslie Leiserowitz, Crystal Nucleation, Growth, and Morphology of the Synthetic Malaria Pigment β-Hematin and the Effect Thereon by Quinoline Additives: The Malaria Pigment as a Target of Various Antimalarial Drugs. *J. Am. Chem. Soc.* **129**, 2615-2615 (2007).

72. K. N. Olafson, J. D. Rimer, P. G. Vekilov, Early Onset of Kinetic Roughening due to a Finite Step Width in Hematin Crystallization. *Physical Review Letters* **119**, 198101 (2017).

73. K. N. Olafson, M. A. Ketchum, J. D. Rimer, P. G. Vekilov, Molecular Mechanisms of Hematin Crystallization from Organic Solvent. *Crystal Growth & Design* **15**, 5535-5542 (2015).

74. S. R. Vippagunta, A. Dorn, R. G. Ridley, J. L. Vennerstrom, Characterization of Chloroquine–Hematin μ-Oxo Dimer Binding by Isothermal Titration Calorimetry. *Biochim. Biophys. Acta* **1475**, 133-133 (2000).

75. K. N. Olafson, T. Q. Nguyen, J. D. Rimer, P. G. Vekilov, Antimalarials inhibit hematin crystallization by unique drug–surface site interactions. *Proceedings of the National Academy of Sciences* **114**, 7531 (2017).

76. S. Yau, B. R. Thomas, P. G. Vekilov, Molecular mechanisms of crystallization and defect formation. *Phys Rev Lett* **85**, 353-356 (2000).

77. D. N. Petsev, K. Chen, O. Gliko, P. G. Vekilov, Diffusion-limited kinetics of the solution–solid phase transition of molecular substances. *Proceedings of the National Academy of Sciences* **100**, 792 (2003).

78. W. K. Burton, N. Cabrera, F. C. Frank, N. F. Mott, The growth of crystals and the equilibrium structure of their surfaces. *Philosophical Transactions of the Royal Society of London. Series A, Mathematical and Physical Sciences* **243**, 299-358 (1951).

79. P. G. Vekilov, Y. G. Kuznetsov, A. A. Chernov, Interstep interaction in solution growth; (101) ADP face. *Journal of Crystal Growth* **121**, 643-655 (1992).

80. G. H. Gilmer, R. Ghez, N. Cabrera, An analysis of combined surface and volume diffusion processes in crystal growth. *Journal of Crystal Growth* **8**, 79-93 (1971).

81. C.-F. Kuo, M. J. Grainge, W. Zhang, M. Doherty, Global epidemiology of gout: prevalence, incidence and risk factors. *Nature Reviews Rheumatology* **11**, 649 (2015).

82. Jeffrey D. Rimer, Zhihua An, Zina Zhu, Michael H. Lee,1 David S. Goldfarb, Jeffrey A. Wesson, Michael D. Ward, Crystal growth inhibitors for the prevention of L-cystine kidney stones through molecular design. *Science* **330**, 337-341 (2010).

83. Bryan T. Mott, Richard T. Eastman, Rajarshi Guha, Katy S. Sherlach, Amila Siriwardana, Paul Shinn, Crystal McKnight, Sam Michael, Norinne Lacerda-Queiroz, Paresma R. Patel, Pwint Khine, Hongmao Sun, Monica Kasbekar, Nima Aghdam, Shaun D. Fontaine, Dongbo Liu, Tim Mierzwa, Lesley A. Mathews-Griner, Marc Ferrer, Adam R. Renslo, James Inglese, Jing Yuan, Paul D. Roepe, Xin-zhuan Su, Craig J. Thomas, High-throughput matrix screening identifies synergistic and antagonistic antimalarial drug combinations. *Sci Rep* **5**, 13891 (2015).

84. S. Pagola, P. W. Stephens, D. S. Bohle, A. D. Kosar, S. K. Madsen, The structure of malaria pigment β-haematin. *Nature* **404** 307-310 (2000).

85. D. J. Sullivan, H. Matile, R. G. Ridley, D. E. Goldberg, A Common Mechanism for Blockade of Heme Polymerization by Antimalarial Quinolines. *Journal of Biological Chemistry* **273**, 31103-31107 (1998).

86. K. S. Sherlach, P. D. Roepe, Determination of the Cytostatic and Cytocidal Activities of Antimalarial Compounds and Their Combination Interactions. *Current Protocols in Chemical Biology* **6**, 237-248 (2014).

87. A. P. Gorka, L. M. Jacobs, P. D. Roepe, Cytostatic versus cytocidal profiling of quinoline drug combinations via modified fixed-ratio isobologram analysis. *Malar J* **12**, 332-332 (2013).

88. K. N. Olafson, T. Q. Nguyen, J. D. Rimer, P. G. Vekilov, Antimalarials inhibit hematin crystallization by unique drug–surface site interactions. *Proceedings of the National Academy of Sciences* **114**, 7531-7536 (2017).

89. D. J. Sullivan, Quinolines block every step of malaria heme crystal growth. *Proceedings of the National Academy of Sciences of the United States of America* **114**, 7483-7485 (2017).

90. J. E. Vance, Growth and Perfection of Crystals. *Journal of the American Chemical Society* **81**, 3489-3490 (1959).

91. N. Cabrera, D. A. Vermileya, in *Growth and Perfection of Crystals,* R. H. Doremus, B. W. Roberts, D. Turnbul, Eds. (Wiley, New York, 1958), vol. 393-408.

92. R. T. Eastman, D. A. Fidock, Artemisinin-based combination therapies: a vital tool in efforts to eliminate malaria. *Nat Rev Microbiol* **7**, 864-874 (2009).

93. T.-C. Chou, Theoretical Basis, Experimental Design, and Computerized Simulation of Synergism and Antagonism in Drug Combination Studies. *Pharmacological Reviews* **58**, 621-681 (2006).

94. K. A. de Villiers, T. J. Egan, Recent advances in the discovery of haem-targeting drugs for malaria and schistosomiasis. *Molecules* **14**, 2868-2887 (2009).

95. P. B. Bloland, M. Ettling, S. Meek, Combination therapy for malaria in Africa: hype or hope? *Bulletin of the World Health Organization* **78**, 1378-1388 (2000).

96. S Looareesuwan 1 , C Viravan, H K Webster, D E Kyle, D B Hutchinson, C J Canfield, Clinical studies of atovaquone, alone or in combination with other antimalarial drugs, for treatment of acute uncomplicated malaria in Thailand. *Am J Trop Med Hyg* **54**, 62-66 (1996).

97. T. J. Egan, K. K. Ncokazi, Effects of solvent composition and ionic strength on the interaction of quinoline antimalarials with ferriprotoporphyrin IX. *J. Inorg. Biochem.* **98**, 144-152 (2004).

98. T. J. Egan, Interactions of quinoline antimalarials with hematin in solution. *J. Inorg. Biochem.* **100**, 916-926 (2006).

99. Sahar Farmanesh, Sriram Ramamoorthy, Jihae Chung, John R. Asplin, Pankaj Karande, Jeffrey D. Rimer, Specificity of Growth Inhibitors and their Cooperative Effects in Calcium Oxalate Monohydrate Crystallization. *Journal of the American Chemical Society* **136**, 367-376 (2014).

100. S.-T. Yau, B. R. Thomas, P. G. Vekilov, Molecular mechanisms of crystallization and defect formation. *Phys. Rev. Lett.* **85**, 353-356 (2000).

101. S.-T. Yau, P. G. Vekilov, Quasi-planar nucleus structure in apoferritin crystallisation. *Nature* **406**, 494-497 (2000).

102. S.-T. Yau, B. R. Thomas, O. Galkin, O. Gliko, P. G. Vekilov, Molecular mechanisms of microheterogeneity-induced defect formation in ferritin crystallization. *Proteins: Structure, Function, Genetics* **43**, 343-352 (2001).

103. D. N. Petsev, K. Chen, O. Gliko, P. G. Vekilov, Diffusion-limited kinetics of the solution-solid phase transition of molecular substances. *Proc. Natl. Acad. Sci. USA* **100**, 792-796 (2003).

104. J. W. Gibbs, On the equilibrium of heterogeneous substances, First Part. *Trans. Connect. Acad. Sci.* **3**, 108-248 (1876).

105. W. Kossel, *Nachr. Ges. Wiss. Götingen*, 135-138 (1928).

106. I. N. Stranski, Zur Theorie des Kristallwachstums. *Z. Phys. Chem.* **136**, 259-278 (1928).

107. W. K. Burton, Cabrera, N. &. Frank, F.C., The growth of crystals and equilibrium structure of their surfaces. *Phil. Trans. Roy. Soc. London Ser. A* **243**, 299- 360 (1951).

108. A. A. Chernov, The spiral growth of crystals. *Sov. Phys. Uspekhi* **4**, 116-148 (1961).

109. G. Bliznakov, in *Adsorption et Croissance Cristalline.* (Centre National de la Recherche Scientifique,, Paris, 1965), pp. 291-300.

110. H. Eyring, S. H. Lin, S. M. Lin, *Basic Chemical Kinetics*. (John Wiley and Sons, New York, 1980).

111. A. A. Chernov, *Modern Crystallography III, Crystal Growth,*. (Springer, Berlin, 1984).

112. Weaver, Matthew L, Qiu, S. Roger, Hoyer, John R, Casey, William H, Nancollas, George H, De Yoreo, James J, Inhibition of calcium oxalate monohydrate growth by citrate and the effect of the background electrolyte. *J. Cryst. Growth* **306**, 135-145 (2007).

113. J. J. De Yoreo, Physical Mechanisms of Crystal Growth Modification by Biomolecules. *AIP Conference Proceedings* **1270**, 45-58 (2010).

114. Lutsko, James F, González-Segredo, Nélido, Durán-Olivencia, Miguel A, Maes Dominique, Van Driessche, Alexander E. S, Sleutel, Mike, Crystal Growth Cessation Revisited: The Physical Basis of Step Pinning. *Crystal Growth & Design* **14**, 6129-6134 (2014).

115. S. Y. Potapenko, Threshold for step percolation through impurity fence. *J. Crystal Growth* **133**, 141-146 (1993).

116. Wang Lijun, Zhang Wei, Qiu S. Roger, Zachowicz William J, Guan Xiangying, Tang Ruikang, Hoyer John R, Yoreo James J. De, Nancollas George H, Inhibition of calcium oxalate monohydrate crystallization by the combination of citrate and osteopontin. *J. Cryst. Growth* **291**, 160-165 (2006).

117. D. Kashchiev, *Nucleation. Basic theory with applications*. (Butterworth, Heinemann, Oxford, 2000), pp. 529.

118. J. F. Trape, The public health impact of chloroquine resistance in Africa. *Am J Trop Med Hyg* **64**, 12-17 (2001).

119. E. L. Korenromp, Lives saved from malaria prevention in Africa--evidence to sustain cost-effective gains. *Malar J* **11**, 94 (2012).

120. P. M. O'Neill, G. H. Posner, A medicinal chemistry perspective on artemisinin and related endoperoxides. *Journal of Medicinal Chemistry* **47**, 2945-2964 (2004).

121. S. R. Meshnick, Artemisinin: mechanisms of action, resistance and toxicity. *International Journal for Parasitology* **32**, 1655-1660 (2002).

122. N. White, Antimalarial drug resistance and combination chemotherapy. *Philos Trans R Soc Lond B Biol Sci* **354**, 739-749 (1999).

123. Dondorp Arjen M, Nosten François, Yi Poravuth, Das Debashish, Phyo Aung Phae, Tarning Joel, Lwin Khin Maung, Ariey Frederic, Hanpithakpong Warunee, Lee Sue J, Ringwald Pascal, Silamut Kamolrat, Imwong Mallika, Chotivanich Kesinee, Lim Pharath, Herdman Trent, An Sen Sam, Yeung Shunmay, Singhasivanon Pratap, Day Nicholas P.J, Lindegardh Niklas, Socheat Duong, White Nicholas J, Artemisinin resistance in Plasmodium falciparum malaria. *N Engl J Med* **361**, 455-467 (2009).

124. Ariey Frédéric, Witkowski Benoit, Amaratunga Chanaki, Beghain Johann, Langlois Anne-Claire, Khim Nimol, Kim Saorin, Duru Valentine, Bouchier Christiane, Ma Laurence, Lim Pharath, Leang Rithea, Duong Socheat, Sreng Sokunthea, Suon Seila, Chuor Char Meng, Bout Denis Mey, Ménard Sandie, Rogers William O, Genton Blaise, Fandeur Thierry, Miotto Olivo, Ringwald Pascal, Le Bras Jacques, Berry Antoine, Barale Jean-Christophe, Fairhurst Rick M, Benoit-Vical Françoise, Mercereau-Puijalon Odile, Ménard Didier, A molecular marker of artemisinin-resistant Plasmodium falciparum malaria. *Nature* **505**, 50 (2013).

125. Witkowski Benoit, Amaratunga Chanaki, Khim Nimol, Sreng Sokunthea, Chim Pheaktra, Kim Saorin, Lim Pharath, Mao Sivanna, Sopha Chantha, Sam Baramey, Anderson Jennifer M, Duong Socheat, Chuor Char Meng, Taylor Walter R J, Suon Seil, Mercereau-Puijalon Odile, Fairhurst Rick M, Menard, Didier, Novel phenotypic assays for the detection of artemisinin-resistant Plasmodium falciparum malaria in Cambodia: in-vitro and ex-vivo drug-response studies. *The Lancet. Infectious diseases* **13**, 1043-1049 (2013).

126. Nectarios Klonis, Stanley C. Xie, James M. McCaw, Maria P. Crespo-Ortiz, Sophie G. Zaloumis , Julie A. Simpson, Leann Tilley, Altered temporal response of malaria parasites determines differential sensitivity to artemisinin. *Proc Natl Acad Sci U S A* **110**, 5157-5162 (2013).

127. Nectarios Klonis, Stanley C. Xie, James M. McCaw, Maria P. Crespo-Ortiz, Sophie G. Zaloumis, Julie A. Simpson, Leann Tilley, A Kelch13-defined endocytosis pathway mediates artemisinin resistance in malaria parasites. *Science* **367**, 51-59 (2020).

128. Tuo YangLee, M. YeohMadel, V. TutorMalcolm, J. McConvilleLeann, TilleySimon A. Cobbold, Decreased K13 Abundance Reduces Hemoglobin Catabolism and Proteotoxic Stress, Underpinning Artemisinin Resistance. *Cell Rep* **29**, 2917-2928 e2915 (2019).

129. A. Robert, F. Benoit-Vical, C. Claparols, B. Meunier, The antimalarial drug artemisinin alkylates heme in infected mice. *Proceedings of the National Academy of Sciences of the United States of America* **102**, 13676-13680 (2005).

130. A. M. Stalcup, D. E. Martire, S. A. Wise, Thermodynamic comparison of monomeric and polymeric C18 bonded phases using aqueous methanol and acetonitrile mobile phases. *Journal of Chromatography A* **442**, 1-14 (1988).

131. Darren J. Creek, William N. Charman, Francis C. K. Chiu, Richard J. Prankerd, Yuxiang Dong, Jonathan L. Vennerstrom, Susan A. Charman , Relationship between antimalarial activity and heme alkylation for spiro- and dispiro-1,2,4-trioxolane antimalarials. *Antimicrob Agents Chemother* **52**, 1291-1296 (2008).

132. Q. P. Zeng, P. Z. Zhang, Artesunate mitigates proliferation of tumor cells by alkylating heme-harboring nitric oxide synthase. *Nitric Oxide* **24**, 110-112 (2011).

133. Y. L. Hong, Y. Z. Yang, S. R. Meshnick, The interaction of artemisinin with malarial hemozoin. *Mol Biochem Parasitol* **63**, 121-128 (1994).

134. A. Robert, F. Benoit-Vical, C. Claparols, B. Meunier, The antimalarial drug artemisinin alkylates heme in infected mice. *Proc Natl Acad Sci U S A* **102**, 13676-13680 (2005).

135. Haynes Richard K, Monti Diego, Taramelli Donatella, Basilico Nicoletta, Parapini Silvia, Olliaro Piero, Artemisinin antimalarials do not inhibit hemozoin formation. *Antimicrob Agents Chemother* **47**, 1175 (2003).

136. C. Loup, J. Lelièvre, F. Benoit-Vical, B. Meunier, Trioxaquines and Heme-Artemisinin Adducts Inhibit the In Vitro Formation of Hemozoin Better than Chloroquine. *Antimicrobial Agents and Chemotherapy* **51**, 3768 LP-3770 (2007).

137. R. Kannan, D. Sahal, V. S. Chauhan, Heme-Artemisinin Adducts Are Crucial Mediators of the Ability of Artemisinin to Inhibit Heme Polymerization. *Chemistry & Biology* **9**, 321-332 (2002).

138. L. E. Heller, E. Goggins, P. D. Roepe, Dihydroartemisinin–Ferriprotoporphyrin IX Adduct Abundance in Plasmodium falciparum Malarial Parasites and the Relationship to Emerging Artemisinin Resistance. *Biochemistry* **57**, 6935-6945 (2018).

139. R. E. Desjardins, C. J. Canfield, J. D. Haynes, J. D. Chulay, Quantitative Assessment of Anti-Malarial Activity In Vitro by a Semiautomated Microdilution Technique. *Antimicrobial Agents and Chemotherapy* **16**, 710-718 (1979).

140. W. C. Ma, J. F. Lutsko, J. D. Rimer, P. G. Vekilov, Antagonistic cooperativity between crystal growth modifiers. *Nature* **577**, 497-+ (2020).

141. Elhadj S, Salter E. A, Wierzbicki A, De Yoreo J. J, Han N, Dove P. M, Peptide Controls on Calcite Mineralization: Polyaspartate Chain Length Affects Growth Kinetics and Acts as a Stereochemical Switch on Morphology. *Cryst. Growth Des.* **6**, 197-201 (2006).

142. L. C. Nielsen, J. J. De Yoreo, D. J. DePaolo, General model for calcite growth kinetics in the presence of impurity ions. *Geochimica et Cosmochimica Acta* **115**, 100-114 (2013).

143. P. A. Sigala, D. E. Goldberg, The Peculiarities and Paradoxes of Plasmodium Heme Metabolism. *Annual Review of Microbiology* **68**, 259-278 (2014).

144. Nectarios Klonis, Maria P. Crespo-Ortiz, Iveta Bottova, Nurhidanatasha Abu-Bakar, Shannon Kenny, Philip J. Rosenthal, Leann Tilley, Artemisinin activity against Plasmodium falciparum requires hemoglobin uptake and digestion. *Proceedings of the* National *Academy of Sciences of the United States of America* **108**, 11405-11410 (2011).

145. L. E. Heller, P. D. Roepe, Quantification of Free Ferriprotoporphyrin IX Heme and Hemozoin for Artemisinin Sensitive versus Delayed Clearance Phenotype Plasmodium falciparum Malarial Parasites. *Biochemistry* **57**, 6927-6934 (2018).

146. F. Marin, G. Luquet, Molluscan biomineralization: The proteinaceous shell constituents of Pinna nobilis L. *Materials Science and Engineering: C* **25**, 105-111 (2005).

147. S. M. Porter, Seawater Chemistry and Early Carbonate Biomineralization. *Science* **316**, 1302-1302 (2007).

148. A. S. Myerson, *Handbook of Industrial Crystallization: Third Edition*. (Cambrifge University Press, Cambridge, 2019).

149. J. W. Gibbs, On the equilibrium of heterogeneous substances (concluded). *Trans. Connect. Acad. Sci.* **3**, 343-524 (1878).

150. J. W. Gibbs, *The scientific papers of J.W. Gibbs. Volume One Thermodynamics*. (Oxbow Press, Woodbridge, Connecticut, 1993).

151. N. Cabrera, D. A. Vermilyea, in *Growth and Perfection of Crystals,* R. H. Doremus, B. W. Roberts, D. Turnbul, Eds. (Wiley, New York, 1958), vol. 393-408.

152. A. G. Shtukenberg, M. D. Ward, B. Kahr, Crystal growth with macromolecular additives. *Chemical reviews* **117**, 14042-14090 (2017).

153. M. Sleutel, J. F. Lutsko, D. Maes, A. E. Van Driessche, Mesoscopic Impurities Expose a Nucleation-Limited Regime of Crystal Growth. *Physical review letters* **114**, 245501 (2015).

154. N. Kubota, J. W. Mullin, A kinetic model for crystal growth from aqueous solution in the presence of impurity. *J. Cryst. Growth* **152**, 203-208 (1995).

155. S. Y. Potapenko, Moving of step through impurity fence. *J. Cryst. Growth* **133**, 147-154 (1993).

156. J. P. Lee-Thorp, A. G. Shtukenberg, R. V. Kohn, Effect of Step Anisotropy on Crystal Growth Inhibition by Immobile Impurity Stoppers. *Crystal Growth & Design* **17**, 5474-5487 (2017).

157. A. I. Lupulescu, J. D. Rimer, Tailoring Silicalite-1 Crystal Morphology with Molecular Modifiers. *Angew. Chem.-Int. Edit.* **51**, 3345-3349 (2012).

158. Sirois Cherilyn M, Latz Eicke, Fitzgerald Katherine A, Rayner Katey J, Kono Hajime, Espevik Terje, Hornung Veit, Abela George S, Schnurr Max, Lien Egil, Wright Samuel D, Vladimer Gregory, Nuñez Gabriel, Rock Kenneth L, Duewell Peter, Bauernfeind Franz G, Franchi Luigi, Moore Kathryn J, NLRP3 inflammasomes are required for atherogenesis and activated by cholesterol crystals. *Nature* **464**, 1357-1361 (2010).

159. N. Blagden, R. J. Davey, Polymorph Selection: Challenges for the Future? *Crystal Growth & Design* **3**, 873-885 (2003).

160. P. E. Bonnett, K. J. Carpenter, S. Dawson, R. J. Davey, Solution crystallization via a submerged liquid-liquid phase boundary: oiling out. *Chem. Commun.*, 698-699 (2003).

161. R. G. Chakrabarti, P. G. Vekilov, Attraction between Permanent Dipoles and London Dispersion Forces Dominate the Thermodynamics of Organic Crystallization. *Crystal Growth & Design* **20**, 7429-7438 (2020).

162. Y. Hu, J. K. Liang, A. S. Myerson, L. S. Taylor, Crystallization Monitoring by Raman Spectroscopy: Simultaneous Measurement of Desupersaturation Profile and Polymorphic Form in Flufenamic Acid Systems. *Industrial & Engineering Chemistry Research* **44**, 1233-1240 (2005).

163. D. Khamar, J. Zeglinski, D. Mealey, Å. C. Rasmuson, Investigating the Role of Solvent–Solute Interaction in Crystal Nucleation of Salicylic Acid from Organic Solvents. *Journal of the American Chemical Society* **136**, 11664-11673 (2014).

164. M. A. Lovette, M. F. Doherty, Needle-Shaped Crystals: Causality and Solvent Selection Guidance Based on Periodic Bond Chains. *Crystal Growth & Design* **13**, 3341-3352 (2013).

165. Spijker Peter, Hiasa, Takumi, Musso, Tiziana, Nishioka Rina, Onishi Hiroshi, Foster, Adam S, Understanding the Interface of Liquids with an Organic Crystal Surface from Atomistic Simulations and AFM Experiments. *The Journal of Physical Chemistry C* **118**, 2058-2066 (2014).

166. E. L. Paul, H.-H. Tung, M. Midler, Organic crystallization processes. *Powder Technology* **150**, 133-143 (2005).

167. *Frontiers in Crystalline Matter:From Discovery to Technology*. (The National Academies Press, 2009).

168. L. Farkas, Keimbildungsgeschwindigkeit in übersättigten Dämpfen. *Z. phys. Chem.* **125**, 236-242 (1927).

169. P. G. Vekilov, in *Crystallization via Nonclassical Pathways Volume 1: Nucleation, Assembly, Observation & Application*. (American Chemical Society, 2020), vol. 1358, chap. 2, pp. 19-46.

170. J. Brunner, H. Cölfen, in *Crystallization via Nonclassical Pathways Volume 1: Nucleation, Assembly, Observation & Application*. (American Chemical Society, 2020), vol. 1358, chap. 4, pp. 73-96.

171. P. G. Vekilov, The Two-step Mechanism of Nucleation of Crystals in Solution. *Nanoscale* **2**, 2346 - 2357 (2010).

172. J. De Yoreo, in *Crystallization via Nonclassical Pathways Volume 1: Nucleation, Assembly, Observation & Application*. (American Chemical Society, 2020), vol. 1358, chap. 1, pp. 1-17.

173. O. Galkin, K. Chen, R. L. Nagel, R. E. Hirsch, P. G. Vekilov, Liquid-liquid separation in solutions of normal and sickle cell hemoglobin. *Proc. Natl. Acad. Sci. USA* **99**, 8479-8483 (2002).

174. Tomoya Yamazaki, Yuki Kimura, Peter G. Vekilov, Erika Furukawa, Manabu Shirai, Hiroaki Matsumoto, Alexander E. S. Van Driessche, Katsuo Tsukamoto, Two types of amorphous protein particles facilitate crystal nucleation. *Proceedings of the National Academy of Sciences* **114**, 2154-2159 (2017).

175. Ma Xiang, Zhang Shuai, Jiao Fang, Newcomb Christina J, Zhang Yuliang, Prakash Arush, Liao Zhihao, Baer Marcel D, Mundy Christopher J, Pfaendtner James, Noy Aleksandr, Chen Chun-Long, De Yoreo, James J, Tuning crystallization pathways through sequence engineering of biomimetic polymers. *Nature Materials* **16**, 767 (2017).

176. W. Qin, A. Agarwal, M. K. Choudhary, J. C. Palmer, J. D. Rimer, Molecular Modifiers Suppress Nonclassical Pathways of Zeolite Crystallization. *Chemistry of Materials* **31**, 3228-3238 (2019).

177. D. Kim, J. Moore, C. P. McCoy, N. J. Irwin, J. D. Rimer, Engaging a Battle on Two Fronts: Dual Role of Polyphosphates as Potent Inhibitors of Struvite Nucleation and Crystal Growth. *Chemistry of Materials*, (2020).

178. Rae Cho Kang, Kim Yi-Yeoun, Yang Pengcheng, Cai Wei, Pan Haihua, Kulak Alexander N, Lau Jolene L, Kulshreshtha Prashant, Armes Steven P, Meldrum

Fiona C, De Yoreo James J, Direct observation of mineral–organic composite formation reveals occlusion mechanism. *Nature Communications* **7**, 10187 (2016).

179. S. Weiner, L. Addadi, Design strategies in mineralized biological materials. *Journal of Materials Chemistry* **7**, 689-702 (1997).

180. F. C. Meldrum, H. Cölfen, Controlling Mineral Morphologies and Structures in Biological and Synthetic Systems. *Chemical Reviews* **108**, 4332-4432 (2008).

181. W. Ma, J. F. Lutsko, J. D. Rimer, P. G. Vekilov, Antagonistic cooperativity between crystal growth modifiers. *Nature* **577**, 497-501 (2020).

182. S. Weiner, P. M. Dove, in *Biomineralization*. (2003), vol. 54, pp. 1-29.

183. S. Weiner, H. D. Wagner, THE MATERIAL BONE: Structure-Mechanical Function Relations. *Annual Review of Materials Science* **28**, 271-298 (1998).

184. J. Aizenberg, D. A. Muller, J. L. Grazul, D. R. Hamann, Direct Fabrication of Large Micropatterned Single Crystals. *Science* **299**, 1205-1208 (2003).

185. Weaver Matthew L, Qiu S. Roger, Hoyer John R, Casey William H, Nancollas George H, De Yoreo, James J, Improved model for inhibition of pathological mineralization based on citrate–calcium oxalate monohydrate interaction. *ChemPhysChem* **7**, 2081-2084 (2006).

186. Ma Wenchuan, Balta Victoria A, West Rachel, Newlin Katy N, Miljanić Ognjen Š, Sullivan David J, Vekilov Peter G, Rimer Jeffrey D, A second mechanism employed by artemisinins to suppress Plasmodium falciparum hinges on inhibition of hematin crystallization. *Journal of Biological Chemistry* **296**, 100123 (2021).

187. K. N. Olafson, J. D. Rimer, P. G. Vekilov, Early Onset of Kinetic Roughening due to a Finite Step Width in Hematin Crystallization. *Physical Review Letters* **119**, 198101-198101 (2017).

188. V. Stojanoff, D. P. Siddons, L. A. Monaco, P. G. Vekilov, F. Rosenberger, X-ray topography of tetragonal lysozyme grown by the temperature controlled technique. *Acta Crystallogr. Section D* **53**, 588-595 (1997).

189. K. N. Olafson, T. Q. Nguyen, P. G. Vekilov, J. D. Rimer, Deconstructing Quinoline-Class Antimalarials to Identify Fundamental Physicochemical Properties of Beta-Hematin Crystal Growth Inhibitors. *Chemistry – A European Journal* **23**, 13638-13647 (2017).

190. Tsarfati Yael, Rosenne Shaked, Weissman Haim, Shimon Linda J. W, Gur Dvir, Palmer Benjamin A, Rybtchinski Boris, Crystallization of Organic Molecules: Nonclassical Mechanism Revealed by Direct Imaging. *ACS Central Science* **4**, 1031-1036 (2018).

191. L. Houben, H. Weissman, S. G. Wolf, B. Rybtchinski, A mechanism of ferritin crystallization revealed by cryo-STEM tomography. *Nature* **579**, 540-543 (2020).

192. Clifford P. Brangwynne, Christian R. Eckmann, David S. Courson, Agata Rybarska, Carsten Hoege, Jöbin Gharakhani, Frank Jülicher, Anthony A. Hyman, Germline P Granules Are Liquid Droplets That Localize by Controlled Dissolution/Condensation. *Science* **324**, 1729-1732 (2009).

193. Feric Marina, Vaidya Nilesh, Harmon Tyler S, Mitrea Diana M, Zhu Lian, Richardson Tiffany M, Kriwacki Richard W, Pappu Rohit V, Brangwynne

Clifford P, Coexisting Liquid Phases Underlie Nucleolar Subcompartments. *Cell* **165**, 1686-1697 (2016).

194. P. M. Chaikin, T. C. Lubensky, *Principles of condensed matter physics*. (Cambridge Unversity Press, Cambridge, 1995).

195. P. G. Debenedetti, *Metastable Liquids*. (Princeton Univ Pr, Princeton, 1996).

196. Safari Mohammad S, Wang Zhiqing, Tailor Kunaal, Kolomeisky Anatoly B, Conrad Jacinta C, Vekilov Peter G, Mesoscopic Liquid Clusters Represent a Distinct Condensate of Mutant p53. *bioRxiv*, 2020.2002.2004.931980 (2020).

197. M. Warzecha, M. S. Safari, A. J. Florence, P. G. Vekilov, Mesoscopic Solute-Rich Clusters in Olanzapine Solutions. *Crystal Growth & Design* **17**, 6668-6676 (2017).

198. Warzecha Monika, Guo Rui, M. Bhardwaj Rajni, Reutzel-Edens Susan M, Price Sarah L, Lamprou Dimitrios A, Florence Alastair J, Direct Observation of Templated Two-Step Nucleation Mechanism during Olanzapine Hydrate Formation. *Crystal Growth & Design* **17**, 6382-6393 (2017).

199. M. A. Vorontsova, H. Y. Chan, V. Lubchenko, P G. Vekilov, Lack of Dependence of the Sizes of the Mesoscopic Protein Clusters on Electrostatics. *Biophysical Journal* **109**, 1959-1968 (2015).

200. M. S. Safari, M. A. Vorontsova, R. Poling-Skutvik, P. G. Vekilov, J. C. Conrad, Differential dynamic microscopy of weakly scattering and polydisperse protein-rich clusters. *Physical Review E* **92**, 042712 (2015).

201. H. Y. Chan, V. Lubchenko, A mechanism for reversible mesoscopic aggregation in liquid solutions. *Nature Communications* **10**, 2381 (2019).

202. M. S. Safari, M. A. Vorontsova, R. Poling-Skutvik, P. G. Vekilov, J. C. Conrad, Anomalous Dense Liquid Condensates Host the Nucleation of Tumor Suppressor p53 Fibrils. *iScience* **12**, 342-355 (2019).

203. W. Pan, P. G. Vekilov, V. Lubchenko, The origin of anomalous mesoscopic phases in protein solutions. *J. Phys. Chem. B* **114** 7620-7630 (2010).

204. Ho Y. Chan, V. Lankevich, Peter G. Vekilov, V. Lubchenko, Anisotropy of the Coulomb Interaction between Folded Proteins: Consequences for Mesoscopic Aggregation of Lysozyme. *Biophysical Journal* **102**, 1934-1943 (2012).

205. M. S. Safari, M. C. Byington, J. C. Conrad, P. G. Vekilov, Polymorphism of Lysozyme Condensates. *The Journal of Physical Chemistry B* **121**, 9091-9101 (2017).

206. Y. Li, V. Lubchenko, M. A. Vorontsova, L. Filobelo, P. G. Vekilov, Ostwald-Like Ripening of the Anomalous Mesoscopic Clusters in Protein Solutions. *The Journal of Physical Chemistry B* **116**, 10657-10664 (2012).

207. Noy A, McBride M. T, Orme C.A, Grantham M, Teng H.H, Dove P.M, Wierzbicki A, DeYoreo J.J, Formation of chiral morphologies through selective binding of amino acids to calcite surface steps. *Nature* **411**, 775-779 (2001).

208. A. E. Stephenson, J. J. DeYoreo, L. Wu, K. J. Wu, J. Hoyer, P. M. Dove, Peptides Enhance Magnesium Signature in Calcite: Insights into Origins of Vital Effects. *Science* **322**, 724-727 (2008).

209. S. W. Guo, M. D. Ward, J. A. Wesson, Direct visualization of calcium oxalate monohydrate crystallization and dissolution with atomic force microscopy and the role of polymeric additives. *Langmuir* **18**, 4284-4291 (2002).

210. Jung Taesung, Sheng Xiaoxia, Choi Chang Kyun, Kim Woo-Sik, Wesson Jeffrey A, Ward Michael D, Probing crystallization of calcium oxalate monohydrate and the role of macromolecule additives with in situ atomic force microscopy. *Langmuir* **20**, 8587-8596 (2004).

211. A. I. Lupulescu, J. D. Rimer, In Situ Imaging of Silicalite-1 Surface Growth Reveals the Mechanism of Crystallization. *Science* **344**, 729-732 (2014).

212. Dey A, Bomans P.H.H, Muller F.A, Will J, Frederik P.M, With de, G, Sommerdijk N.A.J.M, The role of prenucleation clusters in surface-induced calcium phosphate crystallization. *Nature Materials* **9**, 1010-1014 (2010).

213. E. B. French, W. A. Robb, Biliary and renal colic. *Br Med J* **2**, 135-138 (1963).

214. Suhalim Jeffrey L, Chung Chao-Yu, Lilledahl Magnus B, Lim Ryan S, Levi Moshe, Tromberg Bruce J, Potma Eric O, Characterization of cholesterol crystals in atherosclerotic plaques using stimulated Raman scattering and second-harmonic generation microscopy. *Biophys J* **102**, 1988-1995 (2012).

215. C. R. Loomis, G. G. Shipley, D. M. Small, The phase behavior of hydrated cholesterol. *J Lipid Res* **20**, 525-535 (1979).

216. S. Park, T. N. Sut, G. J. Ma, A. N. Parikh, N.-J. Cho, Crystallization of Cholesterol in Phospholipid Membranes Follows Ostwald's Rule of Stages. *Journal of the American Chemical Society* **142**, 21872-21882 (2020).

217. Abela George S., Aziz Kusai, Vedre Ameeth, Pathak, Dorothy R. Talbott John D., DeJong Joyce, Effect of Cholesterol Crystals on Plaques and Intima in Arteries of Patients With Acute Coronary and Cerebrovascular Syndromes. *The American Journal of Cardiology* **103**, 959-968 (2009).

218. Gadeela Nitesh, Rubinstein Jack, Tamhane Umesh, Huang Ruiping, Pathak Dorothy R, Hosein Hazel-Ann, Rich Michael, Dhar Gaurav, Abela George S, The Impact of Circulating Cholesterol Crystals on Vasomotor Function: Implications for No-Reflow Phenomenon. *JACC: Cardiovascular Interventions* **4**, 521-529 (2011).

219. A. Grebe, E. Latz, Cholesterol crystals and inflammation. *Curr Rheumatol Rep* **15**, 313-313 (2013).

220. R. Ziblat, L. Leiserowitz, L. Addadi, Crystalline Domain Structure and Cholesterol Crystal Nucleation in Single Hydrated DPPC:Cholesterol:POPC Bilayers. *Journal of the American Chemical Society* **132**, 9920-9927 (2010).

221. R. S. Abendan, J. A. Swift, Cholesterol Monohydrate Dissolution in the Presence of Bile Acid Salts. *Crystal Growth & Design* **13**, 3596-3602 (2013).